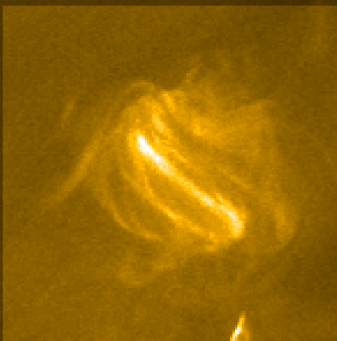


Structuring of the quiet solar corona

Nikolina Milanović



International Max Planck Research School
on Physical Processes in the Solar System and Beyond
at the Universities of Braunschweig and Göttingen

Structuring of the quiet solar corona

Von der Fakultät für Elektrotechnik, Informationstechnik, Physik
der Technischen Universität Carolo-Wilhelmina zu Braunschweig

zur Erlangung des Grades einer Doktorin

der Naturwissenschaften (Dr. rer. nat.)

genehmigte Dissertation

von Nikolina Milanović

aus Pančevo, Serbien

eingereicht am: 28.06.2024

Disputation am: 30.08.2024

1. Referent: Prof. Dr. Sami Solanki

2. Referent: Prof. Dr. Karl-Heinz Glaßmeier

Druckjahr: 2024

**Dissertation an der Technischen Universität Braunschweig,
Fakultät für Elektrotechnik, Informationstechnik, Physik**

Abstract

The heating of the solar corona, the tenuous outer atmosphere of the Sun, has remained one of the major open questions in solar physics for decades. How the coronal plasma, above the much cooler photosphere, reaches temperatures of millions of degrees is closely related to the magnetic field on the Sun. The magnetic field permeates the solar atmosphere, shaping various active phenomena, from the large active regions with sunspots to the small magnetic features in the so-called quiet Sun. The corona is structured by the magnetic field, as is particularly evident in bright, arch-shaped coronal loops, where hot plasma is tied to the field lines that connect opposite magnetic polarities in the photosphere. In contrast to the clear loops, the corona also exhibits regions of diffuse-looking emission, that show no obvious substructure. The diffuse corona is rarely studied, despite its significant emission at the extreme-ultraviolet (EUV) wavelengths. This poses the questions of what determines the amount of structure we can see in the corona, how the diffuse emission is connected to magnetic footpoints in the lower atmosphere, and how different the heating mechanisms in distinct loops and in the diffuse areas are. To shed light on these questions, in this thesis we focus on observations of the quiet corona, whose magnetic footpoints lie in the supergranular magnetic network in the photosphere. In two complementary studies, we explore how this highly-structured magnetic foundation can support both structured small loops, and featureless diffuse emission.

Our first study is related to coronal bright points, prominent systems of loops in the quiet corona, that connect small bipoles (~ 20 Mm) in the junctions of the magnetic network. Although very compact, these are complex, multi-thermal features that span different layers in the solar atmosphere. We investigate the thermal structuring of these loops by using the differential emission measure (DEM). By combining spectral data from the EUV spectrometer SPICE on board Solar Orbiter, and imaging data from AIA on board the Solar Dynamics Observatory (SDO), we simultaneously covered a broad range of temperatures, from the low transition region to the corona ($\log T$ [K] ≈ 4.6 – 6.5). We analyzed 14 bright points, and found common behavior in terms of their DEM curves when compared to the average emission of the quiet Sun. At the low-temperature end, below $\log T$ [K] ≈ 5.2 , the negative slope of the bright points' DEM is similar to that of the average quiet Sun. In the upper transition region ($\log T$ [K] ≈ 5.2 – 6.0), the increase of the DEM towards the corona is significantly shallower in the bright points. Our findings are relevant for coronal heating models, and

based on earlier studies, imply less frequent heating events in bright points in comparison to the average quiet Sun. This apparent dichotomy between the plasma at lower and higher temperatures could also imply distinct heating mechanisms, or thermally disconnected loops in the two temperature regimes.

The other side of the coin, opposite of highly structured features, are diffuse regions, to which we turn our attention to in the second part. We focus on a diffuse region observed in coronal images from AIA, above the supergranular network in the quiet Sun. By combining this with the transition-region spectra from IRIS, and the photospheric magnetograms from HMI on SDO, we study how the diffuse emission connects to its magnetic footpoints in the lower atmosphere. We found that the diffuse region hosts plasma at close to 1 MK, related to a magnetic canopy which extends above unipolar magnetic footpoints. Unlike the small loops in coronal bright points, the diffuse region evolves gradually over more than five hours, while showing no clear substructure. This is also contrasted with its footpoint area, where we found spicule-like features and signatures of upflows, that might supply heated material to the diffuse region. Based on magnetic field extrapolations we performed, the diffuse region is found to be located at the base of a long-ranging loop, which has its other footpoint at a great distance of about 300 Mm. The orientation of this loop base toward the observer suggests that integration along the line of sight could be the main reason for the lack of structure seen in the coronal emission, at least in this case.

In summary, by using recent observations that span the solar atmosphere, we studied the quiet corona and its connection to the magnetic footpoints, both in small loops and in the regions with diffuse emission. Explaining how structures form in the corona, and why large areas remain apparently featureless over long periods of time, is a challenging but important task in coronal physics, which might advance our understanding of coronal heating.

Zusammenfassung

Die Aufheizung der Sonnenkorona, der dünnen äußeren Atmosphäre der Sonne, ist seit Jahrzehnten eine der wichtigsten offenen Fragen der Sonnenphysik. Wie das koronale Plasma oberhalb der viel kühleren Photosphäre Millionen von Grad erreicht, hängt eng mit dem Magnetfeld der Sonne zusammen. Das Feld durchdringt die Sonnenatmosphäre und prägt verschiedene aktive Phänomene, von den größten aktiven Regionen mit Sonnenflecken bis hin zu den kleinsten magnetischen Merkmalen in der ruhigen Sonne. Die Korona wird durch das Magnetfeld strukturiert, was besonders in den hellen, bogenförmigen koronalen Schleifen, auch koronale Bögen genannt, deutlich wird, wo heißes Plasma an die Feldlinien gebunden ist, die entgegengesetzte magnetische Polaritäten in der Photosphäre verbinden. Im Gegensatz zu den klaren Bögen weist die Korona auch Regionen mit diffuser Emission auf, die keine offensichtliche Substruktur zeigen. Die diffuse Korona wird trotz ihrer erheblichen Emission im extrem ultravioletten (EUV) Wellenlängenbereich nur selten untersucht. Dies wirft Fragen auf, wie die nach dem Grad der Strukturierung, die wir in der Korona sehen können, dem Zusammenhang der diffusen Emission mit ihren Fußpunkten in der unteren Atmosphäre und der Unterscheidung von Heizmechanismen in ausgeprägten Bögen und in den diffusen Bereichen. Die vorliegende Arbeit bezieht sich auf Beobachtungen der ruhigen Korona, deren magnetische Fußpunkte im supergranularen magnetischen Netzwerk in der Photosphäre liegen. In zwei komplementären Studien untersuchen wir, wie das magnetische Netzwerk sowohl strukturierte, kleine Bögen als auch diffuse Bereiche erzeugen kann.

Die erste Studie befasst sich mit koronalen hellen Punkten, markanten Systemen von kleinen Bögen, die kleine magnetische Bipole (~ 20 Mm) an den Knotenpunkten des magnetischen Netzwerks in der ruhigen Sonne verbinden. Obwohl sie sehr kompakt sind, handelt es sich um komplexe, multithermische Erscheinungen, die sich über verschiedene Schichten der Sonnenatmosphäre erstrecken. Wir untersuchen die thermische Strukturierung dieser Schleifen mit Hilfe der differentiellen Emissionsmessung (DEM). Durch die Kombination von Spektraldaten des EUV-Spektrometers SPICE an Bord von Solar Orbiter und Bilddaten von AIA an Bord des Solar Dynamics Observatory (SDO) haben wir gleichzeitig einen breiten Temperaturbereich abgedeckt, der von der niedrigen Übergangsregion bis zur Korona reicht ($\log T [\text{K}] \approx 4.6\text{--}6.5$). Wir analysierten 14 helle Punkte und fanden ein gemeinsames Verhalten in Bezug auf ihre DEM-Kurven im Vergleich zur durchschnittlichen ruhigen Sonne. Im unteren Temperaturbereich, unter-

halb von $\log T [\text{K}] \approx 5.2$, ist die negative Steigung der DEM ähnlich wie bei der ruhigen Sonne. Im oberen Übergangsbereich ($\log T [\text{K}] \approx 5.2\text{--}6.0$) ist der Anstieg der DEM zur Korona hin in den hellen Punkten deutlich flacher. Unsere Ergebnisse sind für koronale Heizungsmodelle von Bedeutung und deuten auf der Grundlage früherer Studien auf weniger häufige Heizungsereignisse in hellen Punkten im Vergleich zur ruhigen Sonne hin. Diese offensichtliche Dichotomie zwischen dem Plasma bei niedrigeren und höheren Temperaturen könnte auch auf unterschiedliche Heizmechanismen oder thermisch getrennte Bögen in den beiden Temperaturbereichen hindeuten.

Die andere Seite der Medaille, das Gegenteil von stark strukturierten Merkmalen, sind diffuse Regionen, denen wir im zweiten Teil unsere Aufmerksamkeit widmen. Wir konzentrieren uns auf eine diffuse Region, die in koronalen Bildern von AIA oberhalb des supergranularen Netzwerks in der ruhigen Sonne beobachtet wurde. Durch die Kombination mit den Spektren der Übergangsregion von IRIS und den photosphärischen Magnetogrammen von HMI auf SDO untersuchen wir, wie die diffuse Emission mit ihren Fußpunkten in der unteren Atmosphäre verbunden ist. Wir fanden heraus, dass die diffuse Region Plasma in der Nähe von 1 MK beherbergt, das mit einem magnetischen Baldachin verbunden ist, der sich über unipolare magnetische Fußpunkte wölbt. Im Gegensatz zu den kleinen Bögen in den koronalen hellen Punkten entwickelt sich die Region allmählich über mehr als fünf Stunden und zeigt dabei keine klare Substruktur. Dies steht auch im Gegensatz zum Fußpunktbereich, wo wir Spiculen-ähnliche Merkmale und Anzeichen von Aufwärtsströmungen gefunden haben, die möglicherweise erhitztes Material in die diffusen Region injizieren. Ausgehend von den von uns durchgeführten Magnetfeldextrapolationen befindet sich die diffuse Region an der Basis eines langen koronalen Bogens, dessen anderer Fußpunkt sich in einer großen Entfernung von etwa 300 Mm befindet. Die Ausrichtung der unteren Region dieses Bogens auf den Beobachter deutet darauf hin, dass die Integration entlang der Sichtlinie wesentlich zu dem Fehlen an Struktur in der koronalen Emission beigetragen haben könnte.

Anhand aktueller Beobachtungen, die sich über die gesamte Sonnenatmosphäre erstrecken, haben wir die ruhige Korona und ihre Verbindung zu den magnetischen Fußpunkten untersucht, sowohl in kleinen koronalen Bögen als auch in den Regionen mit diffuser Emission. Die Erklärung, wie sich Strukturen in der Korona bilden und warum große Gebiete über lange Zeiträume hinweg scheinbar strukturlos bleiben, ist eine anspruchsvolle, aber wichtige Aufgabe, die unser Verständnis der koronalen Heizung voranbringen könnte.

Contents

Abstract	iv
Zusammenfassung	vi
List of Figures	ix
List of Tables	xi
1 Introduction	1
2 Magnetic field at the surface	5
2.1 Emergence of the field	5
2.2 Magnetically active and quiet regions	7
3 Magnetic connectivity through the atmosphere	11
3.1 Expansion of the magnetic concentrations	11
3.2 Active atmosphere	16
3.3 Quiet atmosphere	19
3.3.1 Chromospheric spicules	20
3.3.2 Structures in the transition region	23
3.3.3 Coronal bright points	26
3.3.4 Diffuse corona	29
3.4 Coronal heating	32
3.4.1 Slow and fast driving: DC and AC heating	33
3.4.2 Temporal nature of coronal heating	34
4 Analysis techniques	37
4.1 Emission-line spectroscopy	37
4.2 Excitation and ionization processes	39
4.3 Optically-thin emission	40
4.3.1 Two-level atom approximation	41
4.3.2 Properties of the line contribution function	42
4.4 Differential emission measure	43
5 Thermal properties of coronal bright points	49
5.1 Observations and data processing	49
5.1.1 Observational data	50
5.1.2 Preparation of data	50

5.1.3	Selection of bright points	53
5.2	DEM analysis of the bright points and the quiet Sun	56
5.2.1	DEM with SPICE	57
5.2.2	DEM with AIA	58
5.3	Results	59
5.3.1	Quiet Sun DEM with SPICE and AIA	59
5.3.2	Properties of the bright points	61
5.4	Discussion	71
5.4.1	Bright points DEM in the lower transition region	72
5.4.2	Bright points DEM in the upper transition region	73
5.4.3	Implications on the frequency of heating	74
5.5	From bright points to diffuse coronal features	76
6	Diffuse solar coronal features and their spicular footpoints	77
6.1	Observations and data processing	77
6.1.1	Observational data	77
6.1.2	Data processing	80
6.1.3	Magnetic field extrapolation	82
6.2	Results	83
6.2.1	Unusual diffuse coronal emission pattern	83
6.2.2	Temporal evolution of the diffuse region	84
6.2.3	Temperature of diffuse region	86
6.2.4	Si iv line profiles at the spicular footpoints of the diffuse region	88
6.2.5	Magnetic connectivity of the diffuse region	90
6.3	Discussion	91
6.3.1	Magnetic structure of diffuse coronal emission	91
6.3.2	Supply of hot gas to the diffuse corona above the quiet Sun	93
7	Conclusions	95
	Bibliography	101
	Publications	117
	Acknowledgments	119
	Curriculum Vitae	121

List of Figures

2.1	Active and quiet regions at the surface	9
3.1	Magnetic field expansion from the supergranular network . .	13
3.2	Active and quiet region in the upper atmosphere	15
3.3	Active region loops	17
3.4	Spicules in the quiet Sun	22
3.5	Loop-like structures in the quiet transition region	24
3.6	Coronal bright point from the footpoints to the corona . . .	27
4.1	Spectrum of a quiet region acquired with SPICE	38
4.2	AIA 171 Å channel temperature response function compared to its main emission line contribution	45
4.3	Emission measure of the quiet Sun	48
5.1	Overview of our observations	51
5.2	Bright point 01 through the solar atmosphere	55
5.3	Differential emission measure of the average quiet Sun	60
5.4	Overview of the bright point 01 observations	62
5.5	Differential emission measure of the bright point 01 com- pared to the quiet Sun	63
5.6	Overview of the results for the bright point 02	64
5.7	Overview of the results for the bright point 03	65
5.8	Evolution of bright points 01, 02 and 03 over the course of 8 hours	69
5.9	Loops in bright point 01	73
6.1	Observational context	78
6.2	Overview of the used data	81
6.3	Temporal evolution of the diffuse region	85
6.4	Diffuse region observed in various spectral bands	87
6.5	Summarized properties of Si IV (1394 Å) profiles around the diffuse region	89
6.6	Large-scale magnetic configuration in the vicinity of the dif- fuse region	91
6.7	Magnetic field configuration within the diffuse region	92
7.1	Coronal bright point study with Solar Orbiter	98

List of Tables

5.1	Spectral lines and bands	52
5.2	Summary of the bright point properties	68
6.1	Lines and EUV bands	79

1 Introduction

Our perception of the solar corona developed over many centuries. For the longest period of time, what was available to our observation was the surface of the Sun – the photosphere, which is the brightest part of the Sun in visible light. From ancient observations and until the late 19th century, the fainter upper solar atmosphere was visible to us exclusively during total solar eclipses. Nevertheless, eclipse observations yielded many records of features related to the corona, reminiscent of rays, arches and clouds that extend over the limb of the solar disk. Development of observational techniques and instruments, including the first spectroheliograph by Hale in 1892, and the first coronagraph by Lyot in 1930, opened doors to more regular and comprehensive studies of such phenomena (Bray et al. 1991). These observations, although not any more tied to the eclipses, were still limited to the visible light.

Advances in observations brought new clues about corona, which Alfvén (1941) perceived together, and based on it argued that the coronal gas must be at about 1 million Kelvin (Peter & Dwivedi 2014). Some of these clues come from spectroscopy, and in particular from the identification of emission lines that originate from highly ionized elements (Edlén 1943; Grotrian 1939). The famous coronal green line at 530.3 nm, for example, originates from thirteen times ionized iron (Fe xiv), whose formation requires temperatures of about 2 MK (1 MK = 10^6 K). Similar temperatures are inferred from the radial extent of the white-light corona, and the related electron density through the pressure scale height. This apparent violation of thermodynamics laws raised a question how the photosphere, that is only about 6000 K hot, can heat and sustain the much hotter corona.

Different ions present in the upper solar atmosphere radiate in emission lines that are typically found in the range from ultraviolet (UV) to X-rays (shortward of ~ 1400 Å; Mariska 1992). At these wavelengths, the contamination from the photosphere drops by several orders of magnitude, as compared to the visible light. This allows for the corona to be observed also against the solar disk, and not only above the limb. The Earth's atmosphere, however, is not transparent to the light shortward of visible wavelengths, so the instruments needed to be placed on rockets and satellites to perform the observations. Furthermore, observations at shorter wavelengths require optical approaches different from the ones in the visible range, including grazing-incidence optics and special coatings of mirrors. Development of

these techniques and observations that started in the 1960s were crucial for understanding the solar corona. In the early 1970s, the new data allowed for an important connection to be established, namely that the bright arches seen in the corona – the coronal loops, are related to the strong magnetic fields at the solar surface (Vaiana et al. 1973).

The magnetic field is generated in the Sun’s interior, in a complex process called the solar dynamo. The field is transported to the surface with the rise of magnetic loops of various sizes. Signatures of the emerged magnetic loops can be seen everywhere in the photosphere. They come in forms of bipolar concentrations of the magnetic flux, located at the base of these loops. The largest flux concentrations are found in the active regions, recognizable by sunspots in the photosphere, and bright plasma loops in the corona. Areas outside the active regions, termed the quiet Sun, are characterized with smaller magnetic features, that individually carry much less flux than the active regions. Still, their ubiquity and fast replenishment is what makes the quiet Sun as important as active regions in terms of solar magnetism (Stein 2012). The magnetic features in the quiet Sun are organized by the supergranular plasma flows. This gives rise to a network pattern, with concentrations of magnetic field at the boundaries between the network cells, which are some 30 Mm ($1 \text{ Mm} = 10^6 \text{ m}$) across.

From the surface, the magnetic field extends upward into the corona, creating configurations of closed field in the active regions and the quiet Sun, and open field in the coronal holes. The so-called open regions are not truly open, of course, but are connected to the heliosphere, and there close back to the respective opposite magnetic polarity on the Sun. In regions of stronger heating, the closed field is outlined by the bright loops of hot and dense plasma. Loops are the building blocks of the corona (Reale 2014). They are arch-shaped and span tens to hundreds of megameters. The most prominent are the loops that span between the large bipolar footpoints in the active regions. Cores of active regions host hot loops of up to almost 10 MK, bright in the X-rays. These are overlaid with larger and somewhat cooler loops, which are well-observed in the extreme-UV (EUV) domain. In the quiet-Sun corona, what stands out are the coronal bright points (Madjarska 2019). These are compact systems of loops, typically 20 Mm across, that connect the bipolar concentrations in the junctions of the magnetic network. They reach temperatures of about 1–2 MK, with indications of hotter loops overlying the cooler ones.

The magnetic field connects the flux concentrations in the photosphere with the overlying chromosphere, the transition region, and eventually the corona. Moving away from the surface, the temperature of plasma rises –

first slowly through the chromosphere, and then sharply through the transition region, leading to the coronal values of about 1 MK. Plasma flows constantly shake and distort the footpoints of the magnetic field in the photosphere. In the photospheric granules, for example, which are convection patterns of typically 1 Mm across, the field is rearranged by the convective flows on timescales of minutes. The field acts like a conduit of this abundant mechanical energy from the photosphere upward, to provide the heating for the corona. Exactly how the energy is transferred to, and as importantly, dissipated in the corona, is the coronal heating problem (Cranmer & Winebarger 2019). Many mechanisms have been proposed to solve the problem, relying on the tangling of the magnetic field lines, formation of currents, propagation of waves, etc. From the point of view of both observations and models, however, it is difficult to select a process, or more likely a combination of processes, that can explain the corona as we see it. This leaves the coronal heating an open question for more than 80 years.

The energy to heat the corona inevitably has to traverse the chromosphere and the transition region. Furthermore, because of the magnetic connection, any dynamic events happening in one of the atmospheric layers can leave an effect on the others. Both the chromosphere and the transition region are dynamic regimes, abundant of small-scale phenomena like spicules, jets, and small loops – all closely related to the structure of the magnetic field. Therefore, when considering how the corona is heated, data that probe different temperature regimes in the atmosphere are highly valuable.

This thesis comprises two complementary studies, which are concerned with the observations of the quiet-Sun corona, with its thermal structuring, and magnetic connectivity. Usually, our attention is drawn to distinct features in the corona, either small or large, simply because of their prominent appearance. This applies certainly to the coronal bright points (Madjarska 2019), which are prominent brightenings at the network junctions. In some way, one can consider the loops in the coronal bright points as morphologically similar to those in the active regions. This poses the question if all features we see in the corona are based on this type of loop structures. A challenge to this is the presence of regions with diffuse emission, that are characterized by an absence of structure (Gorman et al. 2023). Are the magnetic roots of these diffuse features, which are also occurring in the quiet Sun above the magnetic network, similar or different from the coronal bright points? In this work, we analyze these two types of features – coronal bright points and diffuse regions, as two sides of the same coin, essentially relating these features to their magnetic origin in the supergranular network.

In our first study, we analyzed compact loops in coronal bright points (Ch. 5). We used observations that simultaneously cover a broad range of temperatures in the atmosphere – from the low transition region to the corona. The simultaneous aspect is important when studying the thermal characteristics of these short loops, that live for several hours, but evolve on timescales of minutes. Earlier studies of active region loops showed that the thermal properties of plasma can be related to the temporal nature of heating (Del Zanna & Mason 2018). Whether the heating is steady or impulsive, compared to the typical plasma cooling time, will affect the temperature distribution of plasma. We discussed this in the scope of the coronal bright points, which have morphological similarities with the much larger, and presumably more complex active region loops. Our results for the plasma temperature distribution in coronal bright points, in particular between 0.1 and 1 MK, can provide constraints for the future heating models.

While the objective of our first study is the structured emission in the compact and dynamic loops, in the second study we looked at the diffuse corona above the quiet-Sun magnetic network (Ch. 6). A diffuse component of the emission is common to both the active and the quiet corona. In fact, while the distinct loops, sometimes as thin as 200 km, are the most prominent, the bulk of the emission comes from the diffuse and structureless corona (Viall & Klimchuk 2011). This contrast between the clear loops and the diffuse emission poses a question of what determines the amount of details we can see in the corona, and whether the heating mechanisms are fundamentally different for the two components. The diffuse region we studied is at a temperature of about 1 MK, and similarly compact (~ 20 Mm) as the coronal bright points. The hazy appearance it maintains over several hours, however, stands in contrast to its highly-structured footpoints in the lower atmosphere. Our results show that the configuration of the magnetic field on large scales (of hundreds of megameters) can be related to the diffuse appearance of the observed emission.

2 Magnetic field at the solar surface

Nearly all the dynamic phenomena on the Sun, from sunspots to coronal loops, are governed by the solar magnetic field. The presence of this field is first seen at the surface, where sunspots mark the areas of the strongest field – the active regions. Besides from the obvious active regions, a large part of the solar magnetism is contained in the areas with weaker magnetic flux – the quiet Sun. In this section, we discuss the emergence and structuring of the magnetic field at the solar surface.

2.1 Emergence of the field

The global magnetic field of the Sun shows a periodic behavior. The number of sunspots, that is indicative of the magnetic flux, changes with a cycle of about 11 years. Since the global magnetic field changes polarity from one sunspot cycle to the next, the magnetic cycle of the Sun is about 22 years long. During the 11-year cycle, the solar magnetic activity grows to reach a peak, which is followed by the cycle decay and the reversal of the magnetic poles. This periodic growth and dissipation of the field, in contrast to a simple gradual decay, is a sign of a dynamo acting on the Sun. The dynamo is a mechanism in which the magnetic field can be amplified by the means of plasma flows. Flows of charged particles induce currents, which reinforce the field in a positive feedback loop.

On the Sun, the heart of the dynamo is believed to be in the convection zone, spanning from about 0.7 solar radii to the surface. There, the convective motions and the differential rotation (the equator rotating faster than the poles) provide the energy to amplify the field (Solanki et al. 2006). Initially dipole-like (poloidal) field of the Sun is stretched and coiled by the differential rotation during the cycle rise, owing to the field lines being frozen in the plasma (Alfvén's theorem). As the cycle peaks, this process produces a strong, azimuthal (toroidal) magnetic field in the convection zone. During the cycle decay, the global field returns back to the poloidal shape.

Compared to the surroundings, regions of stronger field need to be vacant of plasma, in order to maintain a balance of the total pressure, i.e. the sum of gas and magnetic pressure. This results in magnetic buoyancy and instabilities related to the toroidal field in the convection zone, which causes the rise of the field strands. These strands emerge at the surface in the form of magnetic loops. Where the loops cross the surface, concentrations

of the magnetic flux are observed, with one loop footpoint having positive (outward-directed), and the other negative (inward-directed) magnetic flux. These flux concentrations are roughly described as bundles of nearly parallel and, due to the buoyancy, nearly vertical field lines, called the magnetic flux tubes. The tubes have sharp boundaries and can be of vastly different cross-sectional area, but on average show magnetic flux density of about 1–2 kG¹ (Lagg et al. 2010; Stenflo 1973).

The presence of the magnetic field in the photosphere influences the radiation, which is what allows us to observe and quantify the field. The surface of the Sun – the photosphere, that spans a few hundreds of kilometers in height, is where most of the solar radiation we observe originates. That is because in the photosphere, going outwards from the Sun’s interior, the plasma changes from opaque to transparent. Exactly where within the photosphere this change will occur depends on the wavelength of the radiation, in particular in the spectral lines. Spectral lines originate from the atomic transitions, when an atom changes its energy state because it either absorbs or emits a photon. The strength and shape of spectral lines are sensitive to the conditions in the solar plasma, including the magnetic field. Finally, the field causes one spectral line to split into multiple components with slightly different wavelengths, which is known as the Zeeman effect. Following is a brief description of this phenomenon, and more details can be found in, e.g., chapter 3.5.1 of Stix (2002).

The energy levels of the atom split in the presence of the external magnetic field. This results in the distinct spectral line components, as opposed to the original single line, with wavelength changed because of the slight change in the energy of the transition. In the weak magnetic field B , for one line component the wavelength shift $\lambda - \lambda_0$ is given by

$$\lambda - \lambda_0 = \frac{e}{4\pi cm_e} g^* \lambda^2 B,$$

where e is the elementary charge, c is the speed of light, and m_e is the electron mass. The factor g^* is different for each transition and depends on the quantum numbers characterizing the initial and the final state. There are some important remarks to the expression above. Firstly, a stronger field B introduces a greater line splitting. Secondly, the splitting is more prominent for lines at longer wavelengths. Finally, through the g^* factor, some lines will be more magnetically sensitive than others.

¹Although we use SI units in this thesis, in case of the magnetic flux density, we decided for gauss instead of tesla (1 G = 10⁻⁴ T), because this is commonly used in solar physics. Likewise, in case of the magnetic flux, we decided for maxwell instead of weber (1 Mx = 10⁻⁸ Wb).

Generally, one line splits into multiple components, but these are not all resolved in solar conditions. Therefore, a special case with only three line components (the so-called normal Zeeman effect) is of particular interest. This line triplet contains one central (unshifted) π component and two opposite-shifted σ components. Unless the field is very strong and the original line is magnetically very sensitive, not even these three can always be well-resolved. Fortunately, the components exhibit different polarization states, which are distinguishable by the means of spectropolarimetry. In this way, spectropolarimetry and Zeeman effect are widely used to measure the magnetic fields in the photosphere, and in the chromosphere. In the corona, however, due to a combination of wider spectral lines, weaker fields, and shorter wavelengths at which the observations are carried out, it is difficult to directly measure the field through the Zeeman effect. Therefore, other techniques are necessary, like the field extrapolations based on the photospheric measurements (Wiegelmann et al. 2014).

2.2 Magnetically active and quiet regions

When magnetic loops from the interior emerge in the photosphere, they show as bipolar regions on the maps of the magnetic field, with an average field strength always around 1–2 kG (Solanki et al. 2006). Still, some parts of the surface have greater areas covered with these strong fields, and therefore larger magnetic flux content than others. This is illustrated in Fig. 2.1, which shows intensity in the visible continuum and line-of-sight magnetic field in the photosphere at a given time. These data were acquired with the Helioseismic and Magnetic Imager (HMI; Scherrer et al. 2012; Schou et al. 2012) on board the Solar Dynamics Observatory (SDO; Pesnell et al. 2012). The regions of greater magnetic flux, that are typically bipolar in nature, are called the active regions, with the total magnetic flux of up to 10^{23} Mx (Wiegelmann et al. 2014). An example is shown in Fig. 2.1c,d.

The most prominent features in the active regions are sunspots, which appear dark in the photospheric images (Fig. 2.1c), and are related to large and apparently continuous flux concentrations. Because of the strong magnetic field (Fig. 2.1d), the convection and hence the upflow of hot gas from below are inhibited in sunspots. Consequently, they are cooler and darker than the surroundings. Sunspots consist of a dark, central umbra, surrounded by a less dark penumbra, and their diameters range between a few and 60 Mm. Sunspot umbrae are characterized with strong magnetic fields, usually between 2 and 4 kG (Solanki 2003), but even stronger fields were found at locations of high-speed plasma flows in the outer penumbra (over

7 kG; van Noort et al. 2013).

The magnetic flux in the active regions which is not contained in sunspots is located in smaller concentrations, either the dark pores (a few Mm in diameter) or the bright magnetic elements (a few 100 km). Unlike sunspots, the magnetic elements appear bright, because these much smaller flux tubes can still be efficiently heated from the sides by the surrounding hot gas. Faculae, large and fragmented-looking features that accompany and surround sunspots, are composed of the magnetic elements and the nearly field-free gas in between (Stein 2012).

Areas outside the active regions are termed the quiet Sun, and are characterized by smaller magnetic flux concentrations (Fig. 2.1e). Emerging bipolar regions with flux content of roughly 10^{18} – 10^{20} Mx are called ephemeral regions (e.g., Wiegelmann et al. 2014). There are even smaller bipolar magnetic patches that can emerge in the quiet Sun, with fluxes down to 10^{16} Mx. At first sight, the quiet-Sun magnetism might seem insignificant in comparison to the active regions, but this is not the case. Although an active region contains significantly more flux than the smaller bipolar regions, at any given time, the total flux on the solar disk contained in the (many) small and in the (fewer) large regions is close to even. Even more so, the faster evolution and replenishment of the small-scale bipolar regions makes them contribute more flux in total during the solar cycle (Stein 2012).

Active regions show some systematic properties at their emergence. They occupy only low latitudes on the solar disk, the so-called activity belts, between about $\pm 30^\circ$ around the equator. Sunspot pairs and groups have a preferred east-west orientation, with a certain tilt, so that typically the leading spot is closer to the equator than the trailing ones. Most leading spots are of the same polarity in one hemisphere, and of the opposite in the other. The number of sunspots grows as the solar cycle peaks, and this was often used as an indicator of the cycle phase (Solanki 2003). Ephemeral regions, on the other hand, emerge over a wider area on the disk, and their numbers vary less with the cycle (Wiegelmann et al. 2014).

Fields in the photosphere are greatly influenced by the plasma flows. This can be quantified with the magnetic Reynolds number – the ratio of the field induction by the flows and the diffusion, which is always greater than 1 for the relevant flows (Solanki et al. 2006). The magnetic field lines are frozen to the plasma and carried by the flows, which can cause two opposite polarities to meet and (partially) cancel, or two like polarities to merge. One ubiquitous flow pattern is the granulation, a consequence of convection overshooting in the photosphere. In granules, which are roughly 1 Mm in size, hot plasma rises from the middle and disperses toward the edges,

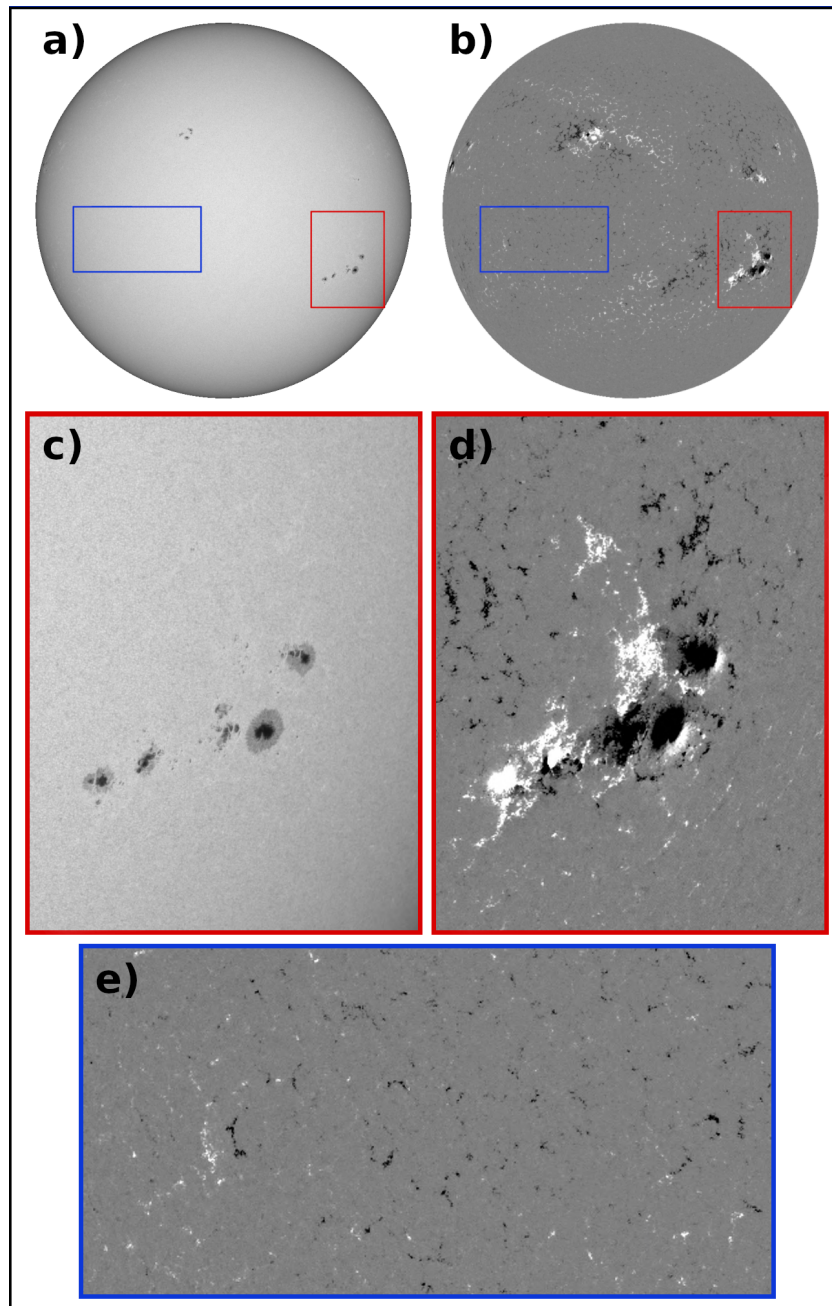


Figure 2.1: Active and quiet regions at the surface. The top panels display the full solar disk, where (a) shows the photosphere in the visible-light continuum, and (b) the line-of-sight magnetic field at the surface. The white and black patches in panel b represent regions of stronger field, where white is the positive (toward the observer), and black is the negative polarity. The red box in (a) and (b) outlines one active region, which is enlarged in panels c and d, respectively. The blue box outlines a quiet region, whose magnetogram is enlarged in panel e. These data were acquired with the HMI instrument on 30 April 2023 at 23:35 UTC, and the images were produced with the ESA JHelioviewer software (Müller et al. 2017).

where it sinks as it cools. This flow creates a pattern of brighter granules and darker intergranular lanes. At the same time, horizontal granular flow concentrates the magnetic flux to the edges of granules. On a larger scale, supergranular flows are important. They swipe the magnetic flux toward the edges of the supergranular cells, which are typically 30 Mm across. This creates a prominent, larger network pattern visible outside the active regions. The magnetic flux is enhanced in the network lanes, at the edges of the supergranules, and weaker in their interiors or the internetwork.

Finally, the flux emerged at the surface eventually gets crumbled and destroyed in complex interactions with the plasma. Generally, larger flux concentrations persist for longer time, and larger features keep their identity for longer (Stein 2012). Granules and fields on granular scales turn over in a few minutes, while the supergranular network gets replenished in about a day. Active regions live for months, before they are decayed by the flows and the diffusion – sunspots being the ones to decay before the faculae. The end of an active region also influences the quiet Sun, as the leftover flux gets recycled and enhances the magnetic network (Wiegmann et al. 2014). This change in the quiet-Sun network is visible over the solar cycle. Around the cycle minimum, the network is weaker and shows mixed (positive and negative) polarities. Predominantly unipolar are only the areas near the poles, with the two hemispheres having opposite main polarities. Around the maximum, however, the presence and the decay of more active regions enhances the network fields, and creates unipolar areas also at lower latitudes. With the decay of an active region, magnetic connectivity between its main polarities may still persist, but now connecting the newly-formed quiet Sun to seemingly unrelated areas on the solar disk, at great distances.

The photosphere hosts many interesting and diverse phenomena, from the large sunspots to the smallest internetwork loops. Since this thesis focuses on the structures in the corona, in the following text (Ch. 3) we will leave the photosphere and discuss the higher parts of the atmosphere.

3 Magnetic connectivity through the atmosphere

The influence of the magnetic field on the Sun is not limited to its surface. Instead, the whole solar atmosphere is permeated with the magnetic field. Through its interactions with plasma, the field shapes and energizes numerous atmospheric features. It also expands further through the heliosphere, where it eventually reaches and influences the Earth. In this section, we discuss this expansion of the magnetic field, and how it creates structures in the solar atmosphere.

3.1 Expansion of the magnetic concentrations

The magnetic field at the solar surface is highly intermittent in time and space, with strong concentrations covering only about 5% of the surface (Wiegmann et al. 2014). From the concentrations in the active regions, and the ones in the quiet-Sun magnetic network, the flux expands and fills the whole volume higher up. How this expansion takes place depends on the conditions in different layers of the atmosphere.

The idea of layers is based on one-dimensional models of the solar atmosphere, where any property of the medium depends only on the radial coordinate or the height above the surface (e.g., Vernazza et al. 1981). In this simplified and static picture, the plasma temperature decreases through the photosphere, from about 6000 K at the base to 4000 K at the temperature minimum. From the minimum upward, it first increases gradually through the chromosphere, reaching close to 10^4 K over some 1500 km. After that, the temperature increases very sharply through only a few 100 km thick transition region, eventually reaching values of 10^6 K in the corona. Over this whole course, the plasma particle density drops from about 10^{17} cm⁻³ in the photosphere to about 10^9 cm⁻³ in the corona. The real Sun, however, is much more complex, with dynamic processes, and both horizontal and vertical structuring, that break the above picture. The atmospheric layers should, therefore, be understood as distinct temperature regimes, rather than the shells with fixed height above the surface.

The one-dimensional picture is still useful, however, when describing how individual features like isolated flux tubes behave. For the ascension of the magnetic flux from the surface, the decrease of the particle density is

important. Assuming that strong magnetic field is located only within the flux tube, the lateral pressure balance at the flux tube walls is

$$p_{\text{gas,e}} \approx p_{\text{gas,i}} + p_{\text{mag}}$$

where $p_{\text{gas,e}}$ and $p_{\text{gas,i}}$ are the (higher) external and the (lower) internal gas pressure, $p_{\text{mag}} = \frac{B^2}{2\mu}$ is the magnetic pressure, and μ is the magnetic permeability (chapter 5.8.1 of Aschwanden 2005). In hydrostatic equilibrium, the gas pressure drops exponentially with height. Assuming a constant temperature, the scale height, i.e. the height where the pressure drops by $1/e$, is $H = \frac{k_B T}{\rho g}$, where k_B is the Boltzmann constant, T the temperature, ρ the density, and g the gravitational acceleration. In the photosphere, this is about 100 km, and hence in the one-dimensional, static models the pressure drops by several orders of magnitude from the surface into the chromosphere. The exponential decrease with height of the gas particle density (and pressure) affects the lateral pressure balance in the flux tube, causing also the field strength inside the tube to decrease. Consequently, the flux tube must expand to cover a larger area, in order for the total magnetic flux in the cross-section of the tube to be conserved.

The flux tubes expand through the photosphere and the chromosphere, resembling a shape of a wine glass. At a certain height (which differs between different regions on the Sun, but is generally below 1 Mm; Solanki & Steiner 1990), the expanding tubes merge with each other. The very edges of the expanding tubes form the so-called magnetic canopy – a structure of nearly horizontal field that outlines the weak-field region below the canopy from the magnetized one above. Above the canopy, the volume is completely filled with the magnetic field that continues to expand upward.

On the scale of the supergranular magnetic network, as the stronger magnetic patches expand into the upper atmosphere, they form funnels that span over the supergranular cells (e.g., Hackenberg et al. 2000). This is illustrated in Fig. 3.1. When these funnels encounter each other, the like-polarity funnels merge, while the opposite polarity ones connect to form magnetic arches (loops). At this level, the plasma is so thin that it no longer influences the magnetic field strength. While the gas pressure continues to drop exponentially, the field drops also rapidly, but with a power-law trend (Solanki et al. 2006). This results in the plasma beta parameter $\beta = \frac{p_{\text{gas}}}{p_{\text{mag}}} \ll 1$, so that the dynamics in the corona is governed by the magnetic field. The coronal field is arranged in a way that it is nearly homogeneous in strength (an order of 10 to 100 of Gauss), but not in the direction.

The corona exhibits two types of the large-scale magnetic field configu-

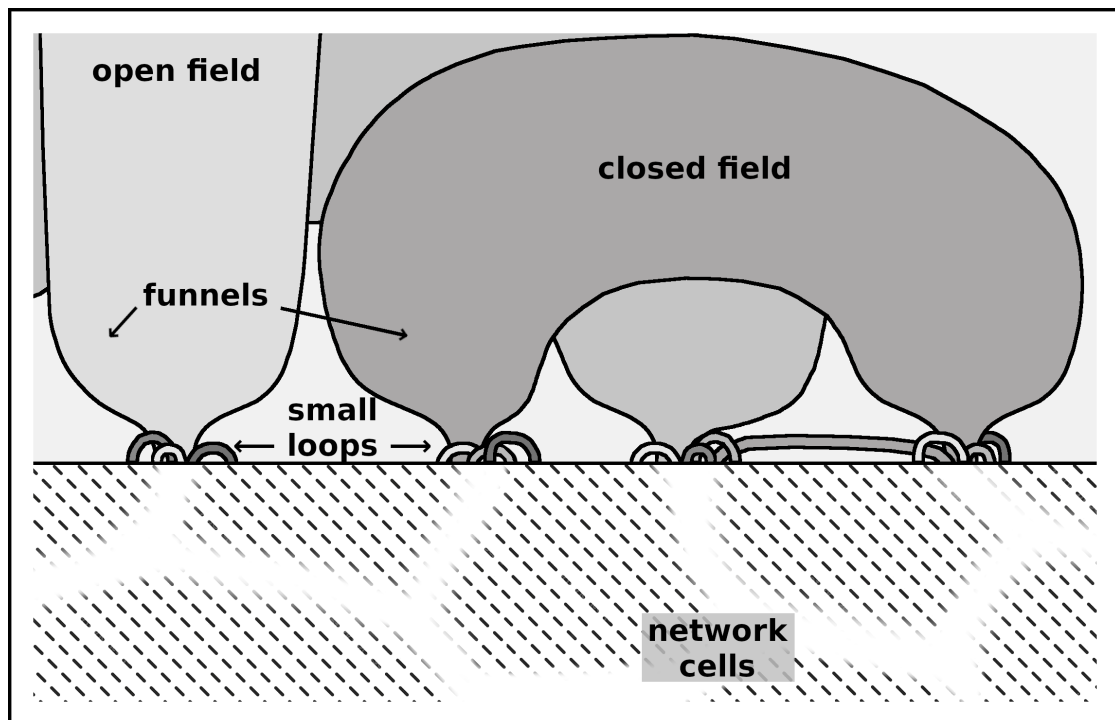


Figure 3.1: Magnetic field expansion from the supergranular network. This figure illustrates the expansion of the magnetic flux tubes from the supergranular network in the quiet Sun, based on similar illustrations from Peter (2001) and Cranmer and van Ballegoijen (2005). The network is shown at the bottom half of the image, where the lanes are marked with white, and the cell interiors with dashed pattern (Sect. 2.2). The expanding magnetic field that forms funnels is shown at the top (Sect. 3.1). Small loops that cross the network lanes, and sometimes the supergranular cells, are shown at the footpoints of the large funnels (Sect. 3.3.2).

rations – the closed and the open one. The closed fields are composed of magnetic arches that connect opposite polarities at the surface, related to the active regions and to the mixed-polarity areas in the quiet Sun. They can be outlined with hot plasma, forming the striking coronal loops. Open fields stem out of the areas at the surface where one polarity dominates. Predominantly unipolar regions are typically present at the poles, and sometimes at the lower latitudes. In the corona, they appear as dark coronal holes, where the hot plasma is successfully transported away from the Sun as the solar wind (Aschwanden 2005). Large structures of closed magnetic field, like helmet streamers, can reach heights of several solar radii. Going further away from the solar surface, most of the coronal field extends nearly radially away from the Sun and connects to the heliosphere.

The chromosphere and the transition region in many ways represent a turning point within the solar atmosphere. As discussed before, the particle density drops significantly in the chromosphere, which causes the magnetic field to turn from the spatially highly-intermittent configuration in the photosphere to the volume-filling one in the corona. Similarly, the plasma, influenced by the thermal motions and flows below the chromosphere, is strongly governed by the magnetic field higher up. Furthermore, the temperature increase across these layers causes the plasma to turn from mostly neutral to fully ionized in the corona. Therefore, the chromosphere and the transition region hold important clues about the photosphere-corona connection.

Looking at the Sun at wavelengths that probe the upper atmosphere (above the photosphere) results in a completely different view from the one at the surface. This is illustrated in Fig. 3.2, that shows data acquired with the Atmospheric Imaging Assembly (AIA; Lemen et al. 2012) on board the SDO. The AIA instrument uses narrowband filters in the EUV domain, sensitive to plasma at different temperatures. The peak sensitivity of the 304 Å channel is at about 0.08 MK (Peter et al. 2022), but due to the complex formation of the He II emission that is sampled there, this channel shows features from both the chromosphere and the transition region. The 171 Å channel samples emission from Fe IX at about 0.8 MK, which includes plasma in between the transition region and the corona. The increased magnetic heating in the active region results in a bright plage seen in the 304 Å channel (Fig. 3.2a). Signs of fibrils – darker, striated features that follow the magnetic connections, begin to show around the active region plage. In the quiet Sun, the dominant structure is the patchy chromospheric network of brighter lanes and darker cell interiors (Fig. 3.2c), due to the underlying network of the magnetic concentrations in the photosphere (Fig. 2.1e). The chromospheric

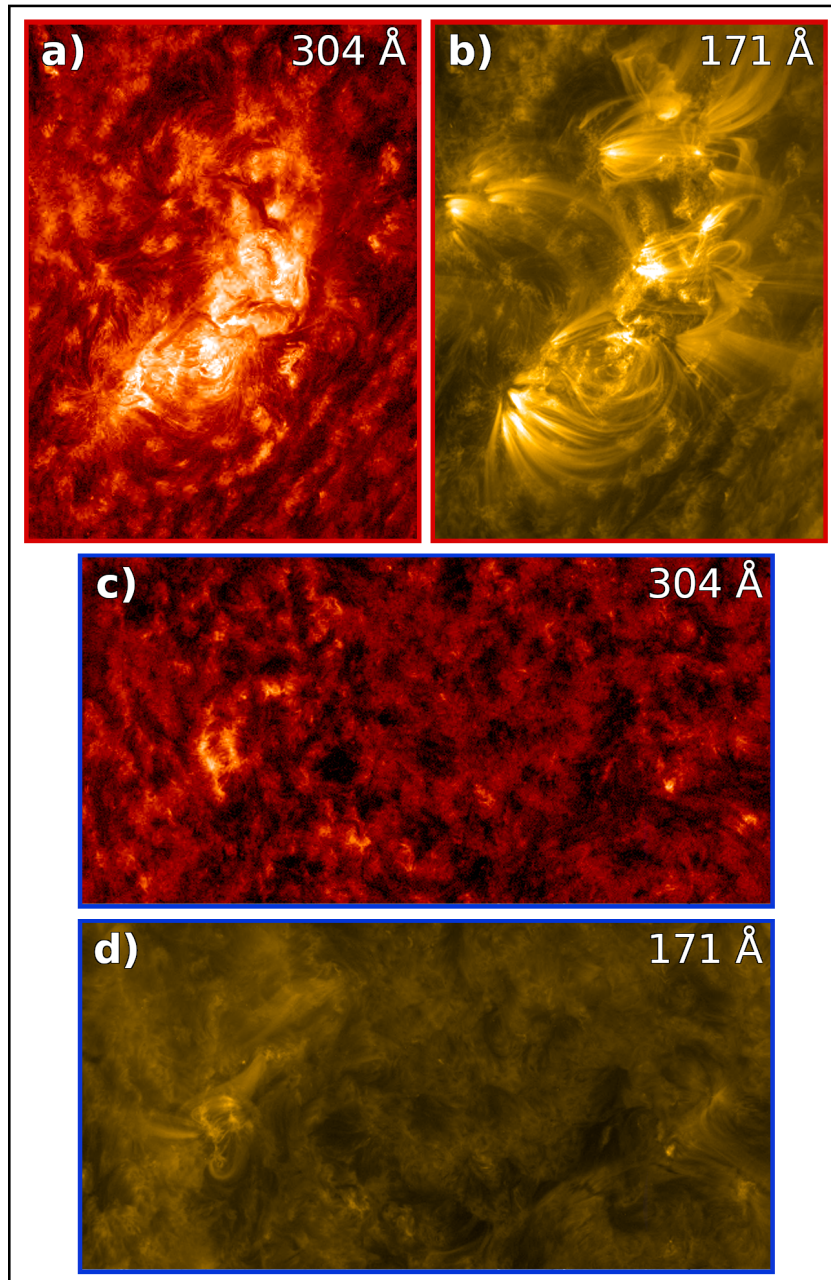


Figure 3.2: Active and quiet region in the upper atmosphere. The active region, shown in the top two panels, and the quiet region, shown in the bottom two panels, are the same as in Fig. 2.1c–e. Different panels show images in the EUV channels at 304 \AA and 171 \AA , with the wavelength of the channel noted in the upper right. These data were acquired with the AIA instrument on 30 April 2023 at 23:35 UTC, and the images were produced with the ESA JHelioviewer software.

network is also structured and abundant of elongated features, like spicules, for example, that follow the configuration of the magnetic field. The organization that the field imposes on the plasma is even more noticeable in the 171 Å images, that in case of the active region show clear, long loops (Fig. 3.2b). Loops can also be seen in the quiet-Sun image, in particular in the small bipolar region in the middle left (cf. Fig. 2.1e and Fig. 3.2d). In the next two sections, we will discuss the active and the quiet atmosphere in more detail.

3.2 Active atmosphere

Increased magnetic activity produces excess heating of the plasma, which is what makes the active regions the brightest and the most prominent features of the upper atmosphere. In the chromosphere, dark sunspots are surrounded by the bright plages, typically observed in the emission from the chromospheric ions like Ca II. Properties of plages and possible ways to heat them, including both the dissipation of waves and the magnetic reconnection, are still studied (Carlsson et al. 2019). Being located at the footpoints of large coronal loops, plages are important for understanding how mass and energy are transferred into the corona. Plages are also visible through the lower transition region, similar to the chromosphere. At higher temperatures, like in the emission of Ne VIII at ~ 0.6 MK, sunspot plumes are prominent. These are extended, bright features above sunspots, that show signatures of downflowing material, and seem to be located at the footpoints of multiple coronal loops (Damasch et al. 2008). Higher in the corona, active regions are identified with the bright coronal loops.

The magnetic field in the corona is outlined by the loops. Loops connect areas with opposite magnetic polarity at the surface, and are shaped like arches, owing to the closed magnetic field configuration (Fig. 3.3). They are, in particular in one-dimensional loop models, often assumed to be semi-circular, which is an over-simplification. Hot and ionized plasma in loops is tied to the magnetic field lines. Because of this magnetic confinement, and because thermal energy is mostly conducted along the field lines, the plasma in loops is considered thermally isolated from the surroundings. This isolation allows loops to exhibit a range of different temperatures. Active regions are found to have hot loops at their core, observed in X-rays at up to almost 10 MK (Reale 2014). At the periphery, there are longer, warm loops, observed in the EUV light at about 1 MK (Mason et al. 1999). There is evidence of both isothermal and multi-thermal loops, the first showing a narrow, and the second a broad plasma temperature distribution. It is pos-

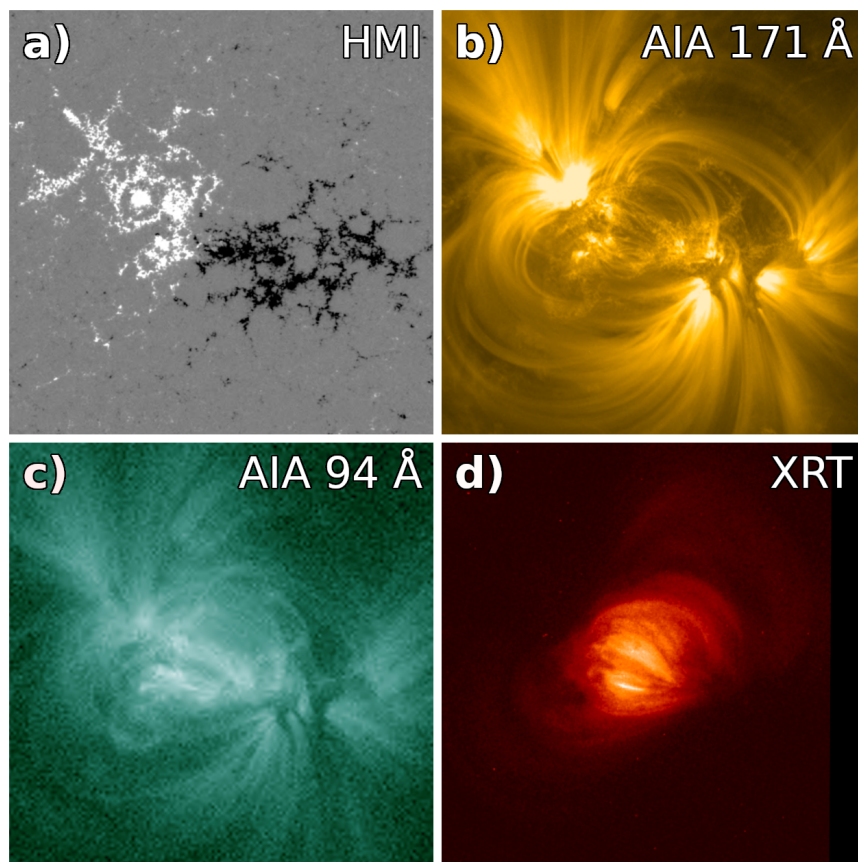


Figure 3.3: Active region loops. This figure displays an active region in different diagnostics. Panel a shows photospheric line-of-sight magnetic field from HMI, at the footpoints of the active region loops. Panels b and c show coronal images in EUV domain, in the 171 Å and 94 Å channels from AIA, respectively. Panel c shows an X-ray coronal image from XRT. These data were acquired on 29 May 2018 at 23:05 UTC, and the images were produced with the ESA JHelioviewer software.

sible that loops at vastly different temperatures (the hot and the warm ones) are intrinsically different, but it could also be that they are representatives of different evolution phases of one and the same class of loops (Reale 2014).

Many open questions about loops arise from the difficulties related to their observation. This is partly due to the optically-thin conditions in the corona, where it is inevitable to average the emission along the line of sight, and the individual features that overlap cannot be separated. Beyond that, there are limitations in the instrumental resolution, the uncertainties of the instrumental (spectral) channels etc. Loops in different filters (or channels) sometimes clearly spatially coincide with each other, possibly being multi-thermal structures. Otherwise, when they do not, it can be an evidence of distinct isothermal features, and of loops going through heating and cooling cycles. The complex thermal structuring of loops is illustrated in Fig. 3.3. The 171 Å filter-image from AIA shows long, warm loops at about 1 MK, and the image from the X-ray Telescope on board the Hinode Mission (XRT; Golub et al. 2007) shows hot loops at several MK in the core of the active region. The 94 Å image from AIA shows a combination of both, since this channel has the main contribution from plasma at about 7 MK, but is also sensitive to cooler plasma at about 1 MK, due to its broad temperature response function.

Significant properties of loops are also their cross-section and fine structure. The cross-section of loops can be related to the structure of the magnetic field in the corona. In case of the potential field configuration, when there are no currents present in the volume, loops should expand with height. The observations, on the other hand, show only modest variation of the loops' cross-section (Klimchuk et al. 1992). Some possible explanations for this include the braiding of the field lines (Schrijver 2007), the variation of the temperature perpendicular to the loop (Peter & Bingert 2012), and the selection bias related to the non-circular cross-section of loops (Malanushenko & Schrijver 2013).

Fine-structuring of loops, or whether loops consist of thinner, unresolved strands, constrains the scales relevant for the heating models. Wide (multi-thermal) temperature distribution in loops can also be interpreted as the presence of many isothermal strands. There has been evidence of monolithic, isothermal loops that are up to about 2000 km wide, but also of strands as narrow as 200 km (Aschwanden & Nightingale 2005; Brooks et al. 2012; Peter et al. 2013). Contrary to that, although the distinct loops are the most remarkable features of the active corona, they are surrounded with a significant amount of diffuse-looking emission (Viall & Klimchuk 2011), which also needs to be considered when discussing the coronal heating.

3.3 Quiet atmosphere

The underlying pattern in the quiet-Sun magnetism is the supergranular magnetic network. Magnetic activity related to the stronger flux in the network lanes provides energy to heat the plasma in the upper atmosphere. This results in a bright network in the chromosphere (Mariska 1992), above the photospheric magnetic concentrations, observed for example in the core of Ca II H and K lines (396.8 nm and 393.4 nm), often used in chromospheric diagnostics.

The network is visible through the transition region, but the contrast between the bright lanes and dark cell interiors changes with temperature (Reeves 1976). The contrast is the strongest in the emission lines of ions that form near 0.1 MK, like C III and O IV, for example. Above the formation temperature of O VI of about 0.3 MK, the contrast of the network quickly drops. In lines that form at coronal temperatures above 1 MK, like those from Mg X, the coherence of the network cannot be recognized anymore. With this change of contrast at different temperatures, although a network pattern is observed in the images, it is unclear where to draw a line between the bright network and the dark internetwork. The distribution of the intensity in the transition-region lines is strongly peaked. This is well-reproduced with a log-normal distribution, which has an extended tail toward higher intensities (Pauluhn et al. 2000). There, it is also unclear where the network stops and the internetwork begins.

The network patches in the transition region expand with temperature (Patsourakos et al. 1999). In the scenario where the magnetic flux tubes expand into funnels (Fig. 3.1), the transition region forms as a thin interface between the chromosphere and the corona, at the base of these large funnels (Gabriel 1976). While this picture agrees with the observed expansion of the network structures through the transition region temperatures, it is rather too simple. The emission in the network, however, appears patchy both in the chromosphere and the transition region, due to the presence of structures on smaller scales. This structuring suggested that the transition region confined to the funnel base might account only for a part of the observed emission (Feldman 1983).

In the chromosphere, the small-scale structure consists of various jet-like features, mostly spicules. Spicules stem out like hairs off the solar limb, reaching a few thousands of kilometers (Beckers 1968). Observed in the transition-region lines, the limb appears ragged as well, and the emission is spread over a few thousands of kilometers, an order of magnitude thicker than inferred from the average models (Mariska et al. 1978). The evidence

of structuring and the observed extent of the emission both suggested that a part of the transition region emission might originate from spicules or other jets. Apart from the jets, the network in the transition region also hosts small loop-like features (Feldman et al. 1999). The small-scale structures in the chromosphere and the transition region evolve on timescales of minutes (Hansteen et al. 2014), which certainly contributes to difficulties in finding a clear one-to-one correspondence between the two.

Higher up in the corona, the network virtually disappears, and the emission often looks hazy and diffuse. The most prominent features are systems of small loops, traditionally called coronal bright points, nested in junctions of the network lanes (Madjarska 2019). In the following subsections, we will discuss in more details specific features mentioned above, which are relevant for the topic of this thesis.

3.3.1 Chromospheric spicules

Spicules are chromospheric features that resemble elongated, thin jets above the solar limb. These jets, typically ~ 1000 km wide and reaching heights of up to 10000 km, are observed in chromospheric lines, hydrogen $H\alpha$ (656 nm) and Ca II H and K. Individual spicules live for a few minutes, and their numbers reach $\sim 10^5$ at any time on the Sun (Beckers 1968). This ubiquity, together with their dynamic nature, is what motivates the question of how spicules fit into a larger picture of heating of the upper atmosphere.

Models showed that the leakage of photospheric acoustic waves into the chromosphere is important for the formation of spicules (De Pontieu et al. 2004). These waves, guided along the inclined flux tubes, steepen into shocks and drive upward-moving spicules, with typical periodicity of about 5 minutes. The chromosphere is flooded with various jets, and, strictly speaking, the term 'spicule' refers only to features observed above the limb. The presence of jets is certainly visible in the observations on the disk as well, but finding the ones that directly correspond to spicules is not straightforward. On the solar disk, dynamic fibrils in the active regions and mottles in the quiet Sun appear as dark jets when observed in the blue wing of the hydrogen $H\alpha$ line (Hansteen et al. 2006; Rouppe van der Voort et al. 2007). These features are related to strong flux tubes in the active-region plages and the quiet-Sun network. Based on their common, jet-like properties, and possible same formation mechanism, they are thought of as suitable counterparts of spicules on the disk.

Many spicules show bright, chromospheric plasma that travels up and falls back down, while others travel only upward and then fade out of view.

While this twofold nature of spicules was known early on, more recent observations clarified the existence of at least two different types of spicules (De Pontieu et al. 2007a). Type I spicules, with the characteristic return flow in the chromosphere, have lifetimes of 3–7 minutes and speeds of 20–40 km s⁻¹. Type II spicules, on the other hand, are more dynamic, with typically shorter lifetimes of about 10–60 s. Their apparent speeds predominantly range between 50–150 km s⁻¹, and they accelerate toward the end of their life, as they disappear from the chromospheric emission. On the disk, they are related to the so-called rapid blue excursions – signatures in the blue wing of the chromospheric lines (Rouppé van der Voort et al. 2009). While leakage of photospheric waves can account for the type I spicules, type II requires different driving, like the release of increased magnetic tension (Martínez-Sykora et al. 2017), or magnetic reconnection at the footpoints (Samanta et al. 2019).

Because of the dynamic nature of the type II spicules, which fade out of the chromospheric channels, it was suspected that they get heated to higher temperatures. This is of particular interest for the source of coronal heating, where spicules could contribute hot matter to the corona (De Pontieu et al. 2009). This idea was reinforced with the observations from the Interface Region Imaging Spectrograph (IRIS; De Pontieu et al. 2014), that showed type II spicules which continue to transition region temperatures (Pereira et al. 2014, see Fig. 3.4), and which are related to jets observed in the transition-region network (De Pontieu et al. 2017b; Tian et al. 2014).

Examples of spicules are shown in Fig. 3.4, as seen at the limb in the quiet Sun in different diagnostics (Pereira et al. 2014). These are the Hinode/SOT filter-image of Ca II (at ≈ 9 kK), the IRIS filter-images of Mg II (≈ 10 kK) and Si IV (≈ 80 kK), and the AIA filter-image in 304 Å channel with He II (≈ 80 kK). In these images, some of the elongated features in Ca II seem to extend into those in Mg II, which then continue into the ones in Si IV. These are the type II spicules, that rise and fade in Ca II, but continue upward (and sometimes show the return flow) in hotter lines. In Si IV, unlike in Ca II and Mg II, the top of the spicule is often brighter than its bottom (top panels in Fig. 3.4). This suggests that predominantly the top part reaches adequate temperature to appear bright in the transition region Si IV line.

The ultimate role of spicules in the upper atmosphere is still debated, and some authors argue that their contribution to the hot coronal plasma is only subtle (Klimchuk 2012). However, spicules might still be relevant for the coronal heating, as they could generate disturbances that would eventually impact the corona (De Pontieu et al. 2017a; Klimchuk 2015). Apart from the vertical motions, most spicules also show periodic transverse dis-

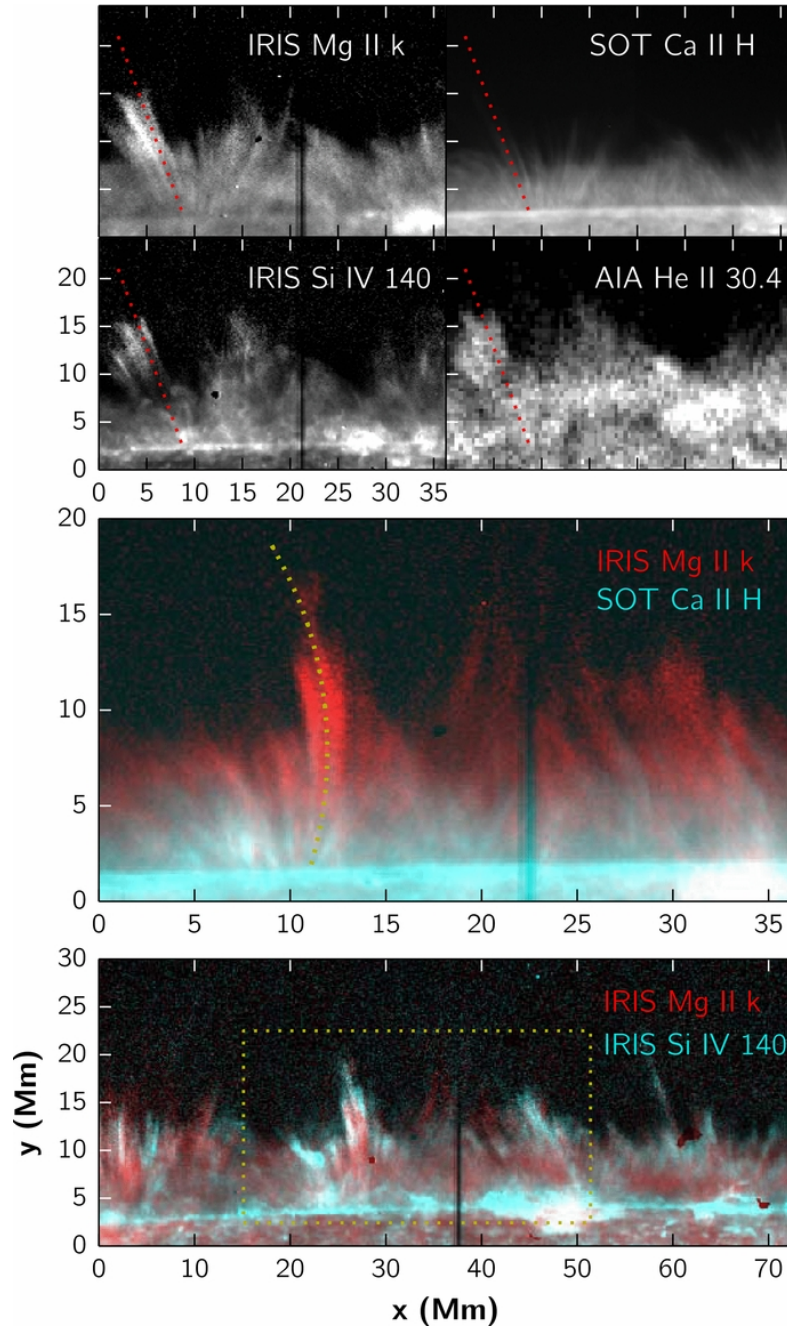


Figure 3.4: Spicules in the quiet Sun. The top four panels show cotemporal filter-images of the solar limb in different diagnostics, with ions/channels as noted in the panels. The middle panel is a color composite of Ca II and Mg II images in the same field of view at a different time. The bottom panel is a color composite of Mg II and Si IV images, but in a larger field of view. The dotted rectangle outlines the field of view of the middle panel. The dotted lines mark individual features highlighted in the study by Pereira et al. (2014), from where this figure was taken © AAS. Reproduced with permission.

placements that can be described as Alfvénic waves (De Pontieu et al. 2007b). These waves, if propagated further and dissipated, could provide energy to heat the quiet corona. Most recently, counterparts of dynamic fibrils were captured at ~ 1 MK (Mandal et al. 2023), thanks to the high spatial resolution (~ 250 km) of the Extreme Ultraviolet Imager (EUI; Rochus et al. 2020) on board the Solar Orbiter mission (Müller et al. 2020).

3.3.2 Structures in the transition region

The transition region is often considered as a thin interface layer of plasma at about 0.1 MK, which is thermally connected to both cooler plasma in the chromosphere below, and to the hot coronal plasma above (Gabriel 1976). In such a scenario, the transition region plasma is predominantly heated by thermal conduction from above, which is a consequence of the energy deposited in the corona. While this might be the case in coronal funnels that constitute the large coronal loops, substructures observed in the transition-region network often do not support such a thermal connection (Feldman 1983). Furthermore, the emission from the transition region in the quiet Sun exceeds the predictions from the conduction-driven models, in which the energy to power the transition region is supplied via thermal conduction from the corona (Athay 1982).

To complement the weak emission from funnels, based on the patchy appearance of the transition-region network, it was suggested that the transition region includes another, dominant component named the unresolved fine structure (Feldman 1983). The fine structure compensates for the observed emission below ~ 0.1 MK, and represents plasma that is magnetically and thermally disconnected from the coronal funnels. Several authors suggested this component to consist of small loops (~ 10 Mm; Antiochos & Noci 1986; Dowdy et al. 1986). These small, low-lying, cool loops span between opposite magnetic polarities in what is called the magnetic junkyard – the field concentrations swept into the network lanes by the supergranular flows. The shorter of these loops cross one network lane, while the longer span across network cells connecting neighboring network patches. Hot, coronal plasma, on the other hand, occupies the large coronal funnels.

Loop-like structures have been observed at transition region temperatures in the quiet-Sun network, in particular with the SUMER instrument on board the SOHO mission. Feldman et al. (1999) reported on ~ 10 Mm long, loop-like features that cross the network lanes in C III images (formation temperature of ≈ 80 kK). Similarly, Landi et al. (2000) reported on filamentary structures that mostly overlie the network lanes, and sometimes

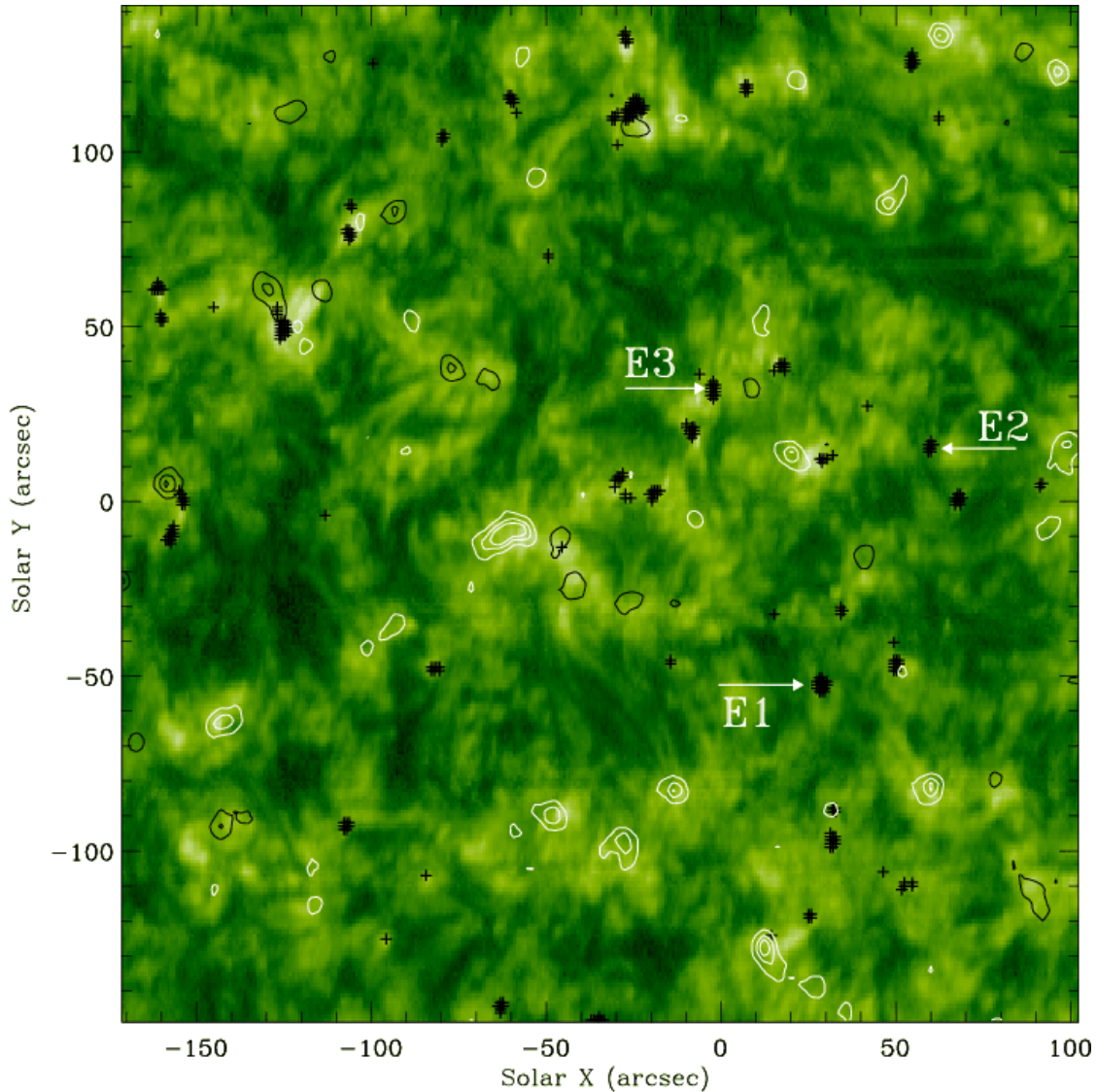


Figure 3.5: Loop-like structures in the quiet transition region. The image shows the quiet Sun near the solar disk center, observed in the O VI emission with SUMER. The overlaid black and white contours outline the magnetic flux concentrations, that seemingly connect to form the supergranular network. The black + symbols mark pixels with spectral signatures of flows, and the white arrows mark three explosive events studied in the work by Teriaca et al. (2004), from where this figure was taken. Credit: Teriaca et al., *A&A*, 427, 1065-1074, 2004, reproduced with permission © ESO.

the supergranular cells in Si IV (≈ 80 kK) and O V (≈ 0.25 MK). Teriaca et al. (2004) studied structures in the network in O VI (≈ 0.3 MK) and showed evidence of flows along the small loops. In Fig. 3.5 we show an O VI image of the quiet region, where many loop-like features are present. These observations support the idea that, in the quiet Sun, the plasma at transition region temperatures resides both in the small, low-lying loops within the network, and in the faint, large-scale funnels that stem out from between the loops (Peter 2001).

The smallest loops in the transition region, related to the unresolved fine structure of Feldman (1983), were observed at the limb with IRIS. Hansteen et al. (2014) showed loops and loop segments that reach up to about 5 Mm above the limb, closing below the spicules, which are also visible in these transition region observations. These miniature loops are very dynamic, with individual features evolving on timescales of a few seconds, and systems of loops being recognizable over a few tens of minutes. Rapid evolution of these loops in the transition region emission is a consequence of the episodic heating and efficient cooling of plasma. Radiative losses, which are the dominant cooling mechanism there, can cool these loops within a few minutes. This efficient cooling, paired with the intermittent heating, ensures the loops to undergo cooling and heating cycles, in which they will repeatedly vanish from and show up in the transition region diagnostics.

Transition region plasma is generally very dynamic and abundant with transient structures. One example are the long-known explosive events. These are compact locations (~ 1500 km) near network lanes, that show spectral signatures of flows in the transition region, and are associated with the magnetic reconnection (Dere 1994; Innes et al. 1997). More recently, it was revealed with the filter-images from IRIS that jets are also ubiquitous in the transition-region network (Tian et al. 2014). These features have apparent speeds of $80\text{--}250$ km s $^{-1}$, lifetimes of a few tens of seconds and widths of about 300 km. They can have an extent of 4–15 Mm, which means that some of the loop-like structures observed with SUMER might actually be jets. Some jets are related to type II spicules, where the higher apparent speed of jets comes from propagating heating fronts, rather than actual mass motions (De Pontieu et al. 2017b). Jets are sometimes associated with the reconnection between the small-scale loops, and the locally-open, background magnetic field in the network. Depending on where the energy is deposited within the atmosphere, jets can show a downflow of matter below the energy deposition site and an upflow above it (Gorman et al. 2022). Chen et al. (2019) showed that network jets sometimes coincide with the explosive events, where signatures of either bidirectional flows or downflows

are detected at the footpoints, and upflows are detected on the jet, but away from the footpoints.

Finally, the patchy bright network in the quiet-Sun transition region seems to consist of small, rapidly-evolving loops and jets. Since both appear as elongated features in the intensity images, it is not always easy to distinguish between the two. Being sometimes related to the type II spicules, and for the same reason of ubiquity and dynamics, network jets are potentially important in the energetics of the upper atmosphere, as they might contribute to the coronal heating and the solar wind.

3.3.3 Coronal bright points

At coronal temperatures, most of the underlying bright network structure is hard to be recognized. The most prominent features in the quiet corona are the coronal bright points. They are known since the early X-ray observations of the corona, when their substructure could not be resolved, hence they were called 'points' (Madjarska 2019).

The early observations showed bright points everywhere on the Sun outside the active regions, with a typical diameter of about 20 Mm, and a smaller, bright core of a few Mm (Golub et al. 1974). Their average lifetime in X-rays is 8 hours, with more bright points with shorter than with longer lifetimes. Bright points are associated with magnetic bipoles at the surface (Fig. 3.6a), with typical flux content of 10^{19} – 10^{20} Mx (Golub et al. 1977; Madjarska 2019). These bipoles are located at the boundaries of the magnetic network, and connected with closed magnetic field lines, that host small, bright loops (Fig. 3.6d). Bright points appear similar, regardless if their magnetic environment is closed on large scales, like in the typical quiet Sun, or open, like in the coronal holes (Habbal et al. 1990).

Multi-thermal observations showed that bright points cover a broad temperature range, spanning the whole upper atmosphere (Habbal & Withbroe 1981). While bright points stand out in the quiet corona, in the transition region they merge with the overall network structure, and appear as network elements that are brighter than average. Fewer bright points are observed at coronal than at transition region temperatures, implying that only some of these loops reach higher temperatures. Furthermore, higher temperatures are reached only for a short time, which explains generally shorter lifetimes of bright points in X-rays (~ 8 h; Golub et al. 1974) than in the EUV domain (~ 20 h; Zhang et al. 2001). The complexity of the emission observed at different temperatures, where the location of brightest features does not always coincide between different channels, suggested that bright points

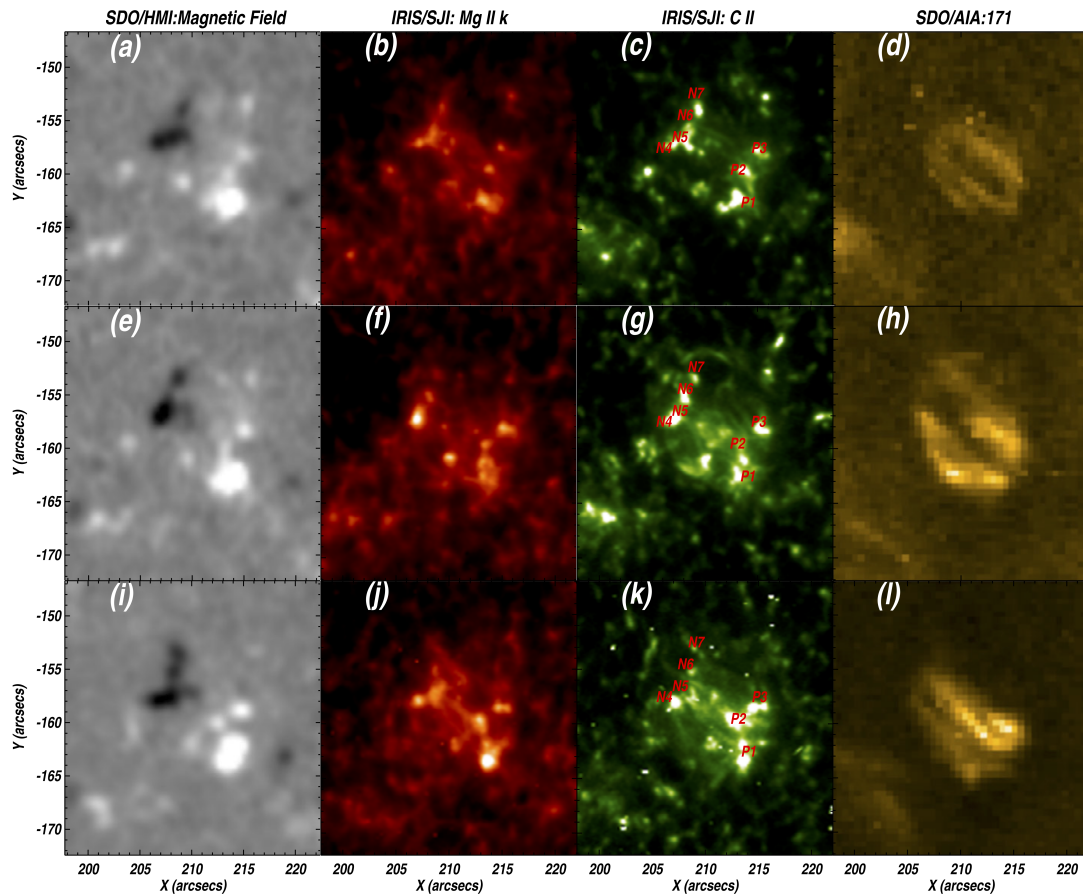


Figure 3.6: Coronal bright point from the footpoints to the corona. This figure displays evolution of a coronal bright point as seen with different instruments, where the second row of images is taken 10 minutes after the first, and the third row another 20 minutes later. The leftmost column shows the photospheric line-of-sight magnetic field from HMI. The two middle columns show the chromospheric filter-images of Mg II and C II from IRIS. The rightmost column shows the coronal emission in the 171 Å channel from AIA. Markings P1–3 and N4–7 stand for the chromospheric brightenings studied in the work by Kayshap and Dwivedi (2017), from where this figure was taken. Reproduced with permission from Springer Nature.

comprise systems of small loops of different sizes and temperatures (Habbal et al. 1990). Based on the emission variability on timescales of minutes, the plasma in these loops should be heated intermittently. Therefore, while the X-ray bright points contain loops that reach temperatures of about 2–3 MK, there is also a spectrum of relatively cooler bright points (up to 1–2 MK), that contain loops prominent in the UV and EUV emission lines.

The main magnetic processes that drive the bright points have long been discussed. In particular, it was questioned whether the bright points correspond mainly to the newly emerged magnetic flux (i.e., the ephemeral regions; Sect. 2.2), or they are related to the already existing magnetic features at the surface (Webb et al. 1993). It is now understood that bright points can exhibit complex magnetic evolution, that can involve several processes. Mou et al. (2016) investigated how the main bipolar features associated with the bright points form. They found that the emergence of new flux is the main formation mechanism in about a half of the bright points (of the 70 cases they studied). In other cases, the formation of the main bipolar features results from random encounters of the already existing flux concentrations. In these random encounters, the authors particularly recognized convergence of the main polarities toward each other from greater distances, and buildup of the main polarities through local coalescence (merger of neighboring features of like polarity). They also found signatures of flux cancellation in all studied bright points, which is believed to be evidence of magnetic reconnection. The cancellation can involve the main magnetic polarities of the bright point, as they converge toward each other, but can also happen between a main polarity and weaker, surrounding ones. McIntosh (2007) proposed that bright points undergo a two-stage heating process. The first stage, which happens in all bright points, is driven by the incessant convective flows. The flows cause reconnection at the junctions of the supergranular network lanes, and heat the bright-point loops to transition region temperatures. The second stage involves reconnection between the rising bright-point loops and the overlying coronal field, and happens only in hotter bright points.

Bright points are complex phenomena that couple plasma at different temperatures, and they are best studied with spectroscopic observations that span the solar atmosphere. This simultaneous spectral coverage of a broad range of plasma temperatures is, however, not regularly available. Tian et al. (2008) analyzed plasma flows and electron densities in a coronal bright point, by using spectroscopic data from SUMER and Hinode/EIS. They found that the bright point consists of cooler and hotter plasma components, further indicating that the loops associated with these two compo-

nents might be powered through different physical mechanisms (McIntosh 2007). The combination of instruments they used offered a broad temperature coverage, with SUMER covering the transition region, and EIS the coronal plasma. The disadvantage of the SUMER data set was, however, that different emission lines were acquired 1–2 hours apart from each other, because the instrument could not access all the lines at the same time. This is not ideal for studying loops that generally evolve on timescales much shorter than that.

Another study by Doschek et al. (2010) investigated bright points by using spectroscopic data from EIS, which covers mostly coronal emission lines. They showed that the bright points exhibit a high level of complexity when observed at different temperatures, but their study lacked strong emission lines to cover the low transition region (below ~ 0.2 MK). Chitta et al. (2013) studied emerging bright points, by using the EUV channels of AIA that sample coronal emission. They compared the observed loops to different models of impulsive plasma heating, and found that a combination of low and high frequency of heating events produces results closest to the observations. Kayshap and Dwivedi (2017) studied bright points using IRIS and AIA data. They found compact brightenings at chromospheric temperatures (Fig. 3.6b, c), located above the magnetic concentrations, at the footpoints of loops that constitute the bright points. They observed loop-like features in the low transition region (Si IV from IRIS) and in the corona (EUV channels from AIA), but there was no coverage of temperatures between 0.1 MK and 0.8 MK.

Despite the studies mentioned so far, the question of how bright points are thermally coupled through the solar atmosphere remains an outstanding issue, mainly due to the lack of simultaneous spectral observations from the chromosphere to the corona. This can certainly be improved with the observations from the Spectral Imaging of the Coronal Environment (SPICE; SPICE Consortium et al. 2020) instrument on board the Solar Orbiter mission. This spectrograph can simultaneously cover a broad range of plasma temperatures, from the low transition region to the corona. In combination with coronal imagers like EUV or AIA, that can acquire observations at a temporal cadence of a few seconds, it provides a powerful tool to study the dynamic loops that build the coronal bright points.

3.3.4 Diffuse corona

The coronal loops – either the large ones in the active regions, or the small ones in the quiet Sun, are the most prominent structures of the corona. In

contrast with the clear loops, and with the highly-structured chromosphere and transition region underneath, both the active and the quiet corona also host bright regions that appear rather diffuse and structureless. Such regions were studied in early X-ray observations, which have moderate spatial resolution (Priest et al. 1998; Sturrock et al. 1996). The diffuse emission is, however, also present in the more recent observations, and not limited to a particular wavelength range, or to a specific temperature of the coronal plasma.

The loops in the active regions, as pointed out by Viall and Klimchuk (2011), are only about 10–20% brighter than the abundant diffuse emission, which is often treated as a background when studying the loops (Del Zanna & Mason 2003). Although being very abundant, and therefore important in the discussion of the coronal heating, the diffuse corona by itself is studied only rarely (e.g., Viall & Klimchuk 2012). It might, however, hold important clues about what determines the amount of structure present in the corona, and how different are the heating processes for the diffuse emission and the distinct loops.

There are various possible reasons for the coronal emission to appear structureless. A volume with homogeneous plasma could be maintained over a longer time by a heating process that is both spatially and temporally constant. This might not be easy to achieve, however, knowing how inhomogeneous the energy input from the photospheric footpoints into the upper atmosphere is. Otherwise, the diffuse-looking emission might not really be structureless. Some of the structures there could simply be on scales beyond the resolution power of the current instrumentation (~ 900 km for AIA, and down to ~ 200 km for EUV). Even if the structures are resolvable, averaging of the optically-thin emission along the line of sight could result in a diffuse-looking corona, where structures are hard to detect. The ability to detect small fluctuations, both in space and time, will then also depend on the sensitivity of the instrument and the signal-to-noise ratio of the observations.

Since the corona is permeated with the magnetic arches, it is possible that the unresolved structure of the diffuse emission consists of individual loops. In particular in active regions, where there are prominent, large loops, the diffuse emission could comprise many loops which overlap along the line of sight (Williams et al. 2020). On the other hand, the diffuse emission is also present in the quiet areas, with no obvious large-scale loops, like in the study by Gorman et al. (2023). There, assuming a closed magnetic configuration in the quiet Sun, it is still possible that faint loops, which overlie the supergranular network, overlap to produce the diffuse emission.

If there are loops within the diffuse corona, they need to have an appropriate width, so that together they produce a smooth-looking background (similarly to the model used to describe the substructure of wide loops, by Peter et al. 2013). In case that these loops are required to be very thin, it is then questionable whether they should still be called loops. Loops represent connected structures of plasma, that stay connected over distances that are typically about 100 Mm, despite the dissipative effects present on small scales within the loop. It is known that dynamic driving of the magnetic footpoints in the photosphere results in the formation of magnetohydrodynamic turbulence in the corona. The component of the magnetic field perpendicular to the loop axis (i.e., to the guiding field) becomes turbulent. In a low plasma- β regime in the corona, this component drives perpendicular motions of plasma within the loop, creating small-scale structures in the loop cross-section (e.g., Breu et al. 2022). This also contributes to slight misalignment of neighboring field lines in the loop, which consequently must reconnect. When two strands reconnect, plasma can be exchanged between them, which effectively causes mixing of plasma across the guiding field. Because of this, very thin strands might not be able to keep their identity over a typical length of the loop, and therefore might not correspond to the traditional definition of a coronal loop.

Another important question is the magnetic connectivity of the diffuse emission, as the energy for the plasma heating should ultimately come from the magnetic footpoints in the photosphere. The magnetic field expands from the flux concentrations at the surface and fills a much larger volume up in the corona. Looking at this from a different perspective, the structures in the corona are rooted in small magnetic sources at the surface, which might not even be in their vicinity when observed in projection on the solar disk. For that reason, it is often difficult to find the direct correspondence between the photospheric and the coronal structures. The location of the magnetic footpoints is certainly clearer for the coronal loops, that trace the shape of the magnetic field, than for the diffuse corona.

In the quiet Sun, based on the idea of the magnetic canopy (Sect. 3.1), the coronal features are expected to originate from the strong flux concentrations in the magnetic network. This scenario, where the weaker flux in the internetwork plays no role above the magnetic canopy, might be too simplified. There are indications of a significant fraction (up to $\sim 50\%$; Schrijver & Title 2003) of the coronal field above the supergranular network being anchored in the mixed polarities of the internetwork. Based on the magnetic field extrapolations, Wiegmann et al. (2010) found that magnetic loops that reach into the corona tend to have asymmetric footpoints, such that one side

of the loop is rooted in stronger, network fields in the photosphere, and the other in the internetwork. The internetwork flux evolves on timescales of minutes, as it is constantly stirred by the granular flows. This implies that the diffuse corona in the quiet Sun, if it really has significant roots in the internetwork, might be powered by many small-scale heating events related to the internetwork magnetism.

3.4 Coronal heating

How a relatively cool photosphere sustains a hot corona is the outstanding question of coronal heating in solar physics. If thermal conduction was the only relevant mechanism for energy transport from the photosphere outward, the temperature would decrease with distance from the energy source, as expected from the laws of thermodynamics. Instead, it rises from 6000 K at the surface to millions of Kelvin in the corona.

It is well-established that mechanisms closely related to the magnetic field are necessary to explain how the high temperatures are reached and maintained in the corona (Aschwanden 2005). The footpoints of the coronal magnetic field are continuously perturbed in the interaction with the convective flows in the photosphere, when mechanical energy is transferred from the flows to the magnetic field. These perturbations then travel upward in the atmosphere, along the magnetic field, and get dissipated in the corona to provide heating. This is the basic idea of coronal heating, where the ultimate energy source for the heating lies in the convective motions under the surface.

Convection carries the mechanical energy from the interior to the photosphere. Most of this energy is radiated away as the plasma parcels reach the surface. The residual flows in the photospheric granules provide an energy flux of the order of 500 kW m^{-2} (Cranmer & Winebarger 2019). However, only a small fraction of the photosphere is magnetically connected to the corona, which reduces the earlier estimate for the energy flux that can eventually take off to the corona by a certain filling factor. This filling factor, essentially a ratio between the field strength in the corona and in the photosphere, ranges roughly between 0.01 in the quiet Sun and 0.1 in active regions. Consequently, the convective flows in the photosphere can provide between 5 and 50 kW m^{-2} for the coronal heating, which is enough to cover the estimated energy losses in the upper atmosphere (Withbroe & Noyes 1977). While this availability of energy is a prerequisite, further details of how this energy is transferred and dissipated are required to solve the heating problem.

On large scales, the corona is organized by a magnetic field that is nearly vertical at the surface, and relatively stable, based for example on the longevity of the overall morphology of the active region loops, or even the coronal bright points. The photospheric driving (i.e., random motion) of the magnetic footpoints gives energy to a smaller, transverse component of the field. For this energy to be dissipated as heating, strong gradients and transfer of energy from large to small spatial scales need to occur in the corona. Depending on the heating scenario, these could be the gradients in the magnetic field, which induce currents in the corona, or the gradients in the velocity field, which are related to viscosity (Klimchuk 2006).

3.4.1 Slow and fast driving: DC and AC heating

Many different mechanisms that rely on the idea of the photospheric driving were suggested to explain the details of the coronal heating (Cranmer & Winebarger 2019). Traditionally, these theories are divided into two major categories, based on the ratio between the footpoint driving speed and the propagation speed of the magnetic disturbance (the latter usually expressed by the Alfvén speed). The mechanisms with slow driving, for which this ratio is small, belong to the so-called DC (Direct Current) heating. On the opposite side, the mechanisms with fast driving belong to the AC (Alternating Current) heating. Determining the most relevant heating mechanism from the observations is difficult, partly because the heating models often depend on parameters that are not directly observable. What is observable, within certain limitations, are the thermal properties of the coronal plasma. These properties, however, represent the aftermath of the heating, and not the heating itself.

The DC heating models assume the photospheric driving to be slow in comparison to the Alfvén transit time, which is the time in which the magnetic disturbance travels along a coronal loop, for example (order of minutes). The field in the corona can, therefore, adjust to the changing condition in the photosphere in a quasi-static way. Random walk of the magnetic footpoints stresses the magnetic field in the corona, causing buildup of nonpotential magnetic energy and formation of current sheets (Parker 1983). When a certain limit is reached, for example a sufficient twist of the field lines, the magnetic energy dissipates into heating, and the field relaxes. The dissipation can occur via different channels, one famous one being through the stress-induced reconnection that produces nanoflares (Parker 1988). Nanoflares are small-scale, burst-like events that locally heat the corona. They happen when slightly misaligned, adjacent magnetic strands

reconnect to become parallel, while releasing $\sim 10^{17}$ J of magnetic energy per event (10^9 times less than in a large-scale flare).

The AC heating models assume fast driving of the footpoints, which results in a plethora of upwardly propagating waves. While waves generated at the surface sustain an energy flux sufficient to heat the corona, the problem lies in transferring this energy against the steep density and temperature gradient in the chromosphere and the transition region (Klimchuk 2006). Alfvén waves, where the tension of the magnetic field lines acts as a restoring force, and where the energy is transferred along the field, have best chances of reaching the corona. There, inhomogeneities in the density and the magnetic field, for example, can cause the neighboring field lines to oscillate increasingly out of phase, and eventually dissipate the waves into heating. Current findings are that the AC models cannot provide enough heating to sustain the coronal loops (Van Doorselaere et al. 2020). On the other hand, waves can cause local misalignment of the magnetic strands and result in reconnection. Due to the development of instabilities and turbulence in the wave models, waves can also affect the twisted flux tubes by mixing the plasma across the field. Therefore, strictly AC or DC models are an idealization, and processes that share characteristics of the two can also occur.

3.4.2 Temporal nature of coronal heating

Another important aspect of coronal heating is how the energy in the corona is dissipated with time. In case the energy dissipation is continuous over some period, the heating is regarded as steady, while if it is intermittent, the heating is impulsive. This is in particular to be compared to the plasma cooling time, which is typically a few tens of minutes for 1 MK plasma (e.g., Aschwanden 2005). In that sense, steady heating can also be understood as consisting of many smaller, but more frequent events, with the waiting time between the events being much less than the plasma cooling time. Impulsive heating, on the other hand, consists of larger, less frequent events.

The frequency with which the heating events occur will affect the thermal properties of the coronal plasma. While the high frequency of heating maintains the plasma at a certain temperature, the lower frequency allows for the hot plasma to cool between the two heating episodes. The first one, therefore, results in a narrower, and the second one in a wider plasma temperature distribution.

The temporal nature of the heating was studied in active regions, and there have been arguments to support both the steady and the impulsive

heating. Warren et al. (2012), for example, proposed that steady heating is required to sustain the hot active region cores, which have a temperature distribution strongly peaked near 4 MK. Viall and Klimchuk (2011), however, argued that there is a signature of cooling plasma in an active region core, and based on that suggested impulsive heating. The frequency of heating was often discussed in the scope of the nanoflare heating models. It should be noted, however, that the term 'nanoflare' acquired a more general meaning of a small-scale, impulsive energy release in the corona, regardless of the exact formation mechanism. In such nanoflare models, a single loop consists of many (i.e., hundreds or thousands) thin, unresolvable and independent magnetic strands. The strands are randomly heated by nanoflares, and the waiting time between the two events can be adjusted to represent different frequencies of heating. Warren et al. (2011) showed that the high-frequency nanoflares result in a sharply peaked, and the low-frequency ones in a broad loop temperature distribution. Cargill (2014) demonstrated that a wide range of the observed thermal properties can be reproduced by the nanoflare heating, if the nanoflare energies are allowed to vary, and the waiting time is proportional to the energy of the previous heating event. What type of heating prevails is still under research, and it might depend on the type of the region that is studied – whether it is quiet Sun, an emerging active region, a decaying active region etc.

We have seen that the magnetic footpoints in the quiet-Sun network are constantly rearranged by the plasma flows (Sect. 2.2). This ever-changing magnetic boundary in the photosphere helps to energize various structures in the upper atmosphere (Sect. 3.3, 3.4). Since this thesis is concerned with the features of the quiet solar corona and their thermal structuring, in the following text (Ch. 4) we will discuss how optically-thin emission can be used for plasma diagnostics in the transition region and corona.

4 Analysis techniques

In this chapter, we will discuss the optically-thin emission lines in the EUV spectrum of the Sun. The properties of these lines strongly depend on the thermal conditions in the plasma. The techniques for the plasma diagnostics with the EUV lines, some of which we will mention in the following text, are widely used for studying the upper solar atmosphere. The discussion in this chapter is limited to topics relevant for this thesis, and more information can be found, for example, in Mariska (1992), Del Zanna and Mason (2018), and the documentation for CHIANTI software and data package (Dere et al. 1997).

4.1 Emission-line spectroscopy

The solar spectrum in the EUV domain between about 100 and 1200 Å, and up to about 1400 Å in the UV domain, is dominated by emission lines. Many of these lines belong to various ions abundant in the solar atmosphere, which form in the transition region and corona, at temperatures between about 20 kK and a few million Kelvin.

An example spectrum of the quiet Sun in this domain obtained with the SPICE spectrograph is shown in Fig. 4.1. The emission lines used for one of the studies in this thesis are marked on the spectrum. The SPICE spectrograph covers a wide range of temperatures, including the lower transition region with C III (977 Å), S V (786 Å), and O IV (788 Å), and the upper transition region with O VI (1032 Å) and Ne VIII (770 Å). It also covers the prominent H I Ly β line (1026 Å) that forms in the upper chromosphere. Apart from the numerous lines, the EUV spectrum also contains continuum emission that originates from recombination of various ions in the chromosphere. In the spectral range observed with SPICE, the H I Lyman continuum is particularly visible in the Short Wavelength Channel (top panel in Fig. 4.1) as a trend on which the lines are superimposed.

The emission lines result from the bound-bound transitions of electrons in an ion, in which photons are emitted. One element can have several associated ionic species (or ionization states) depending on the atomic number, including neutral, one-time ionized, two-times ionized, etc. Each of the ionic species has its associated excitation states, that correspond to the distribution of electrons over the energy levels in the ion. The ion will emit a photon once an electron transitions between two bound, discrete energy

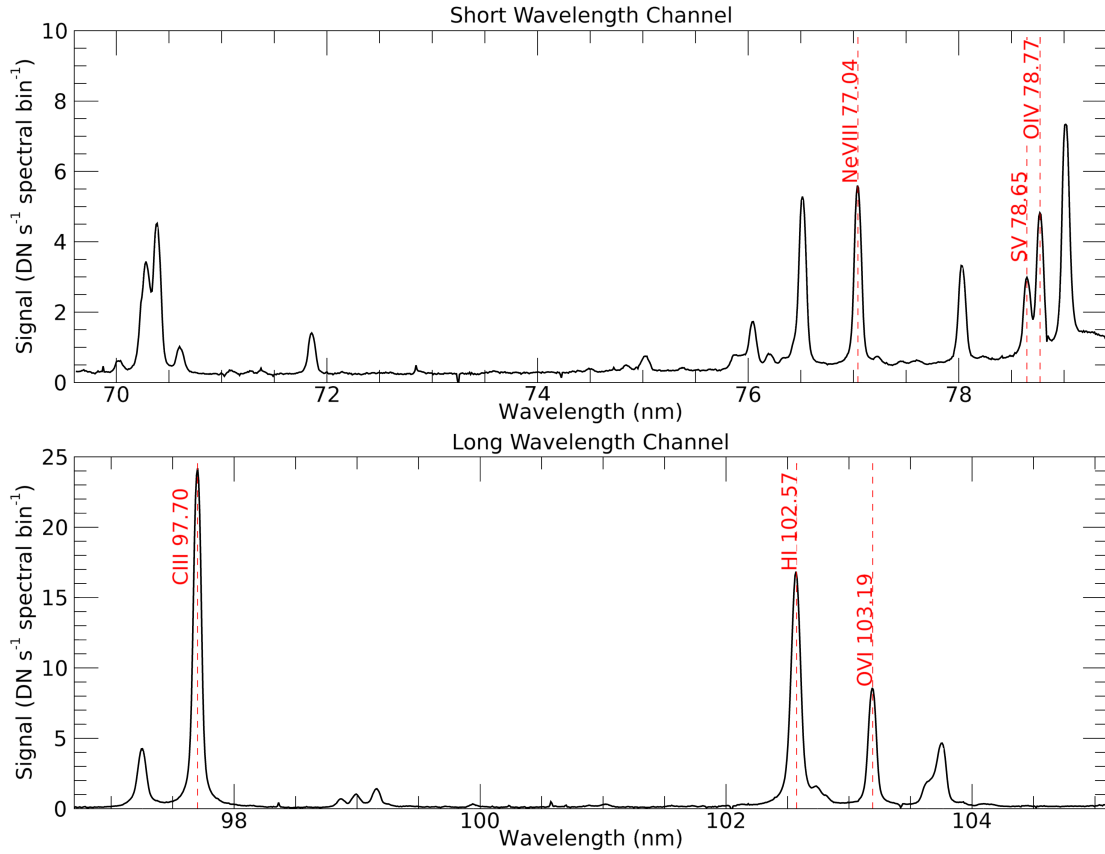


Figure 4.1: Spectrum of a quiet region acquired with SPICE. This figure shows a spectrum of the quiet Sun in the full spectral range of SPICE. The spectrum is covered with two detectors – Short Wavelength Channel (top panel), and Long Wavelength Channel (bottom panel). The lines marked in red are used in the study in Ch. 5. This figure was adapted from the publication by Fludra et al. (2021). Credit: Fludra et al., *A&A*, 656, A38, 2021, reproduced with permission © ESO.

levels, with the photon energy equal to the difference between the upper (excited) and the lower (deexcited) energy level.

The EUV lines are well approximated with a Gaussian profile

$$I_{\lambda} = I_0 \exp[-(\lambda - \lambda_0)^2 / \sigma^2] + C$$

where I_0 is the peak intensity of the line, λ_0 the central wavelength, σ the line width at the intensity equal to I_0/e , and C the intensity of the continuum. The total line intensity is equal to $\sqrt{\pi} I_0 \sigma$.

When there is a resolved, directed motion of plasma in the resolution element of the instrument, the central line wavelength is shifted with respect to the natural (rest) wavelength in accordance with the Doppler effect. On average, emission lines that sample transition region are redshifted for

plasma temperatures up to about 0.5 MK, after which they are blueshifted. While individual events can show stronger shifts, the bulk of the plasma shows subsonic motions with amplitudes that are not greater than about $10\text{--}15\text{ km s}^{-1}$ (Peter & Judge 1999).

Any additional plasma motions that are not spatially resolved by the instrument, i.e. within the resolution element or along the line of sight, will contribute to the (Doppler) broadening of the spectral lines. The lines are therefore wider than the natural line width, that is of the order of 10^{-5} \AA . In the first place, thermal motions of particles will lead to a more significant broadening. The Doppler shift associated with these motions is typically of the order of 10 km s^{-1} at transition region temperatures, and in general is given through $\sqrt{2k_B T/m}$, where k_B is the Boltzmann constant, T the temperature, and m the mean molecular weight. Other motions, often called non-thermal, will also cause line broadening. These motions can be induced through, e.g., turbulence or waves. The Doppler shift of these non-resolved motions then collectively leads to the non-thermal broadening, that mostly exceeds the thermal broadening (e.g., Peter 2001). On top of these effects, the spectral resolution of the instrument introduces additional broadening to the measured spectral lines. This instrumental broadening can be less significant, like in the IRIS spectra (corresponding to $\approx 6\text{ km s}^{-1}$; De Pontieu et al. 2014), or more significant, like in the SPICE spectra ($\approx 120\text{ km s}^{-1}$; Fludra et al. 2021).

4.2 Excitation and ionization processes

Many different processes can contribute to the excitation and ionization of ions, and therefore need to be considered in the line formation. Only a few of these processes are relevant for the EUV lines formed in the solar transition region and corona.

There is a distinction between collisional and radiative processes, both of which can contribute to the excitation or deexcitation of an ion. In the collisional processes, an ion is excited (or deexcited) in a collision with another particle. In a fully ionized plasma, the ions predominantly collide with the free electrons. No photon is exchanged in the process, and the excitation (deexcitation) of the ion happens at the expense (gain) of the kinetic energy of the free electron. In the radiative processes, on the other hand, an ion is excited by absorbing, and deexcited by emitting a photon.

Collisional excitation is the dominant process to populate the upper energy level in the formation of the optically thin transition-region and coronal EUV lines. Radiative excitation can be neglected, because the radia-

tion field is too weak at the wavelengths of the prominent transitions in the transition region and corona. Deexcitation, on the other hand, occurs predominantly via a photon emission, often referred to as the radiative decay. At the typical densities (and temperatures) in the transition region and corona, collisional deexcitation has a characteristic timescale of the order of 10^{-3} s, as compared to the much faster (order of 10^{-9} s) radiative decay, and is therefore usually neglected. Exceptions to this are the forbidden lines, in which the upper energy level is metastable. The typical lifetime of the metastable level, until it undergoes a spontaneous, radiative decay, can be of the same order as the timescale for collisional deexcitation. Therefore, collisional deexcitation and radiative decay become competing processes in the forbidden lines, and both need to be considered for transitions from the metastable levels.

Collisions with electrons and interactions with photons can also lead to ionization or recombination of an ion. Such processes affect the overall population of a specific ionic species in the plasma, and are therefore also important for the line formation. Similarly to the excitation processes, collisional ionization via electron collisions dominates over the radiative ionization (photoionization) in the transition region and corona. Likewise, radiative recombination (which results in the previously mentioned Lyman continuum) dominates over the collisional recombination. The ionization processes have characteristic timescales of the order of 10–100 s, which is much longer than the excitation processes, implying that the two can be treated separately.

4.3 Optically-thin emission

The low-density plasma in the solar transition region and corona is assumed to be optically thin for the majority of the EUV emission lines. This assumption means that any absorption of photons in a line is neglected, and only emission is considered. Therefore, once a photon is emitted, it continues freely toward the observer.

In this scenario, the total intensity of a line that results from a transition between levels j and i in an ion will be

$$I_{ji} = \int_{l.o.s.} \epsilon_{ji} dh, \quad [\text{W m}^{-2} \text{ sr}^{-1}]$$

where ϵ_{ji} is the plasma emissivity, and the integral is performed along the line of sight (hence the l.o.s.). The emissivity ϵ_{ji} , which is essentially the

energy radiated in an emission line per volume, time, and solid angle, comes from the radiative decay from level j to i . It can be expressed as

$$\epsilon_{ji} = \frac{h\nu_{ji}}{4\pi} A_{ji} n_j,$$

where h is the Planck constant, ν_{ji} is the line frequency, $h\nu_{ji}$ is the energy of the transition, n_j is the number density of the excited level, and A_{ji} is the Einstein coefficient for the transition, which signifies the probability of the radiative decay. This gives for the total line intensity

$$I_{ji} = \int_{l.o.s.} \frac{h\nu_{ji}}{4\pi} A_{ji} n_j dh. \quad (4.1)$$

4.3.1 Two-level atom approximation

Another often used simplification is that only two excitation levels are considered in the ion – the lower and the upper level of the observed transition. In the transition region and corona, because of the radiative decay being much faster than the collisional excitation, for most strong lines the lower level is the ground state of the ion. These are the resonance lines, like for example the lines from Si IV at 1394 Å and 1403 Å. In this case, the only two relevant excitation processes are the collisional excitations from the ground level, and the radiative decay from the excited level. Assuming the excitation balance, so that the number density of either the ground (n_1) or the excited level (n_2) is constant with time, gives

$$A_{21} n_2 = C_{12} n_e n_1 \quad (4.2)$$

where C_{12} is the collisional excitation coefficient, n_e is the number density of the free electrons, and these two together signify the probability for the collisional excitation to occur.

In the two-level atom approximation, equation (4.1) becomes

$$I_{21} = \int_{l.o.s.} \frac{h\nu_{21}}{4\pi} A_{21} n_2 dh. \quad (4.3)$$

The excited level population n_2 can be expanded as

$$n_2 = \frac{n_2}{n_{ion}} \frac{n_{ion}}{n_{el}} \frac{n_{el}}{n_H} \frac{n_H}{n_e} n_e, \quad (4.4)$$

where n_{ion} is the total number density of the ionic species, n_{el} of the element (including all of its ionic species), and n_H of hydrogen. The term $A_{el} =$

n_{el}/n_H is the elemental abundance relative to hydrogen. If we define the line contribution function G_{21} as

$$G_{21} = \frac{h\nu_{21} A_{21} n_2 n_{ion}}{4\pi n_e n_{ion} n_{el}}, \quad (4.5)$$

then by substituting equations (4.4) and (4.5) into (4.3), the total line intensity can be rewritten as

$$I_{21} = \int_{l.o.s.} A_{el} G_{21} n_H n_e dh. \quad (4.6)$$

Depending on the author, the elemental abundance A_{el} can also be included in the contribution function G_{21} . This is not the case in the expression we listed above, which is similar to the treatment in CHIANTI.

For illustrative purpose, if we now assume a fully ionized plasma consisting of hydrogen and helium, with a fixed share of helium such that $n_{He} = 0.1n_H$, then $n_e = n_H + 2n_{He}$ and $n_H \approx 0.83n_e$. By including this in equation (4.6), we reveal more clearly an important property of the optically-thin emission lines. Namely, the total line intensity is proportional to the electron number density squared

$$I_{21} = 0.83 \int_{l.o.s.} A_{el} G_{21} n_e^2 dh. \quad (4.7)$$

4.3.2 Properties of the line contribution function

The dependence of the line intensity on the plasma temperature is contained in the line contribution function. The term $\frac{n_{ion}}{n_{el}}$ in equation (4.5) is the relative population of the ionic species. It is often calculated under the assumption of ionization equilibrium, where the population of the species is independent of time. The ionization equilibrium results in population curves that are sharply peaked in temperature, so that each ionic species forms predominantly within a narrow range of temperatures, typically of 0.2 to 0.3 in $\log T$ [K]¹ for prominent transition-region and coronal lines. When the formation temperatures of different ions are mentioned, as it is often the case in this thesis, the ionization equilibrium is the usual underlying assumption. The temperature dependence of the contribution function is then mostly due to the ionization term.

¹We use \log to denote the common logarithm with base 10, and \ln for the natural logarithm with base e .

The term $\frac{A_{21}n_2}{n_e n_{ion}}$ in equation (4.5) is related to the excitation balance. Because the radiative decay proceeds much faster than the collisional excitation, the majority of the ions are in the ground state, so that $n_{ion} \approx n_1$. Based on this, and equation (4.2), the excitation term is simply equal to the collisional coefficient C_{12} , which also peaks in temperature, but less sharply than the ionization. The excitation term then modulates the influence of the ionization term in the contribution function, by slightly shifting the location of the peak in temperature.

Strictly speaking, the contribution function $G_{21}(n_e, T)$ depends not only on the plasma temperature, but also on the electron number density. With the assumptions we had so far, where we considered collisionally-excited, allowed transitions under ionization equilibrium, the dependence on electron density comes from the ionization and recombination rate coefficients. Neglecting this, and assuming only temperature-dependent $G_{21}(T)$, is a good approximation for many lines from the transition region and corona, like the strong resonance lines in the EUV domain.

The properties of the contribution function allow for temperature diagnostics. To carry out this diagnostics, intensity ratio of two emission lines of the same ion can be used, if the lines have sufficiently different excitation energies. Assuming again that these are collisionally-excited, resonant lines, their intensity ratio will be sensitive to temperature through the corresponding collisional excitation coefficients. This method implies significantly different wavelengths of the two lines, which usually cannot be observed with one instrument, and therefore require a multi-instrument approach. Line ratios are more commonly used for density diagnostics, by employing the forbidden lines. The treatment of the forbidden lines is different from what we discussed, since the collisional deexcitations need to be included, which then results in a line ratio sensitive to the electron number density over a certain density range.

4.4 Differential emission measure

A common way of carrying out temperature diagnostics in the upper solar atmosphere is by using the differential emission measure (DEM), which represents the distribution of the observed plasma over temperatures. The DEM can be introduced from equation (4.6) for the total line intensity. As discussed previously, the line contribution function G_{21} is sharply peaked in temperature, such that there is a limited range $(T_m - \Delta T, T_m + \Delta T)$ around the peak T_m in which $G_{21}(T)$ has a significant value. Assuming that the temperature changes monotonously along the line of sight, we can change the

variable and integrate over the corresponding temperature range

$$I_{21} = \int_{T_m - \Delta T}^{T_m + \Delta T} A_{el} G_{21}(T) n_H n_e \left(\frac{dT}{dh} \right)^{-1} dT. \quad (4.8)$$

The differential emission measure $DEM(T)$ can then be defined as

$$DEM(T) = n_H n_e \left(\frac{dT}{dh} \right)^{-1}, \quad [\text{cm}^{-5} \text{K}^{-1}] \quad (4.9)$$

and substituted into equation (4.8), which finally gives for the total intensity

$$I_{21} = \int_{T_m - \Delta T}^{T_m + \Delta T} A_{el} G_{21}(T) DEM(T) dT. \quad (4.10)$$

From the above expression, the total line intensity consists of two distinct parts. The first part represents the atomic properties of the transition, which are contained in $G_{21}(T)$, and which define the favorable conditions for the line formation. The second part combines the properties of the atmosphere, contained in the $DEM(T)$, which describes the distribution of the atmospheric plasma over temperatures.

Specific ions predominantly form at a certain temperature in the atmosphere. Observations of emission lines from various ions can, therefore, be used to sample different parts of the atmosphere, and reconstruct the shape of the DEM. The DEM inversion is essentially a minimization procedure, that begins with a set of measured line intensities, for which the contribution functions are known. In the first iteration, an initial shape of $DEM(T)$ is assumed. Using this, based on equation (4.10) and the line contribution functions, a set of modeled line intensities is calculated. These values are then compared to the measured ones, and based on their difference, the shape of $DEM(T)$ is adjusted for the next iteration. The iterations continue until the difference between the measured and the modeled line intensities reaches a predefined, small value.

Apart from the spectroscopic observations of emission lines, like those with the SPICE spectrograph, data from an imager can also be used for the DEM inversions. The difference with the imager data is that the narrowband channels, like those of the AIA, generally cover more than one emission line. Therefore, when using the channel images, the line contribution function in equation (4.10) is to be replaced with the response function of the channel. The response function describes the sensitivity of the EUV channel to plasma at a certain temperature, and an example for the 171 Å channel of AIA is shown in Fig. 4.2. The response function is significantly wider than

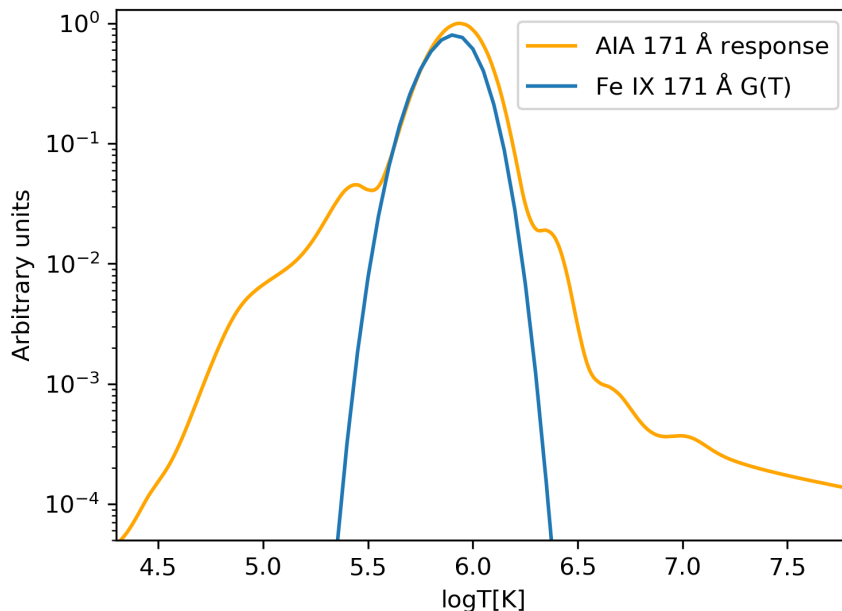


Figure 4.2: AIA 171 Å channel temperature response function compared to its main emission line contribution function. Both curves are produced using CHIANTI software and data package.

the contribution function of the main emission line in the channel, which is in this case the Fe IX line at 171 Å, also shown in the figure. Other prominent contributions to this response function, that show as secondary peaks, are due to O V and O VI just below $\log T$ [K] ≈ 5.5 , and due to Ni XIV at about 6.4.

The temperature distribution of the plasma is often described by using the column emission measure (EM) – a quantity related to the DEM, instead of the DEM itself. The sharply-peaked line contribution function can be taken out of the integral in equation (4.10), and according to the mean value theorem, replaced with its average value $\langle G_{21}(T) \rangle$ within the integration range. With this, and assuming that the elemental abundance is constant along the line of sight, we can rewrite the total intensity as

$$I_{21} = A_{el} \langle G_{21}(T) \rangle \int_{T_m - \Delta T}^{T_m + \Delta T} DEM(T) dT. \quad (4.11)$$

The remaining integral of the DEM over temperature is the column emission measure

$$I_{21} = A_{el} \langle G_{21}(T) \rangle EM, \quad (4.12)$$

$$EM = \int_{T_m - \Delta T}^{T_m + \Delta T} DEM(T) dT = \int_{l.o.s.} n_H n_e dh. \quad (4.13)$$

The EM determined from the intensity of a single emission line is associated with the temperature of the line formation. Therefore, measuring multiple lines that form at different temperatures provides us with the distribution of the EM with temperature. This approach is somewhat different from the DEM. In case of the EM, line intensities are independently used to calculate the EM at each temperature and build the distribution. In the DEM inversions, however, the final DEM distribution is adjusted to satisfy the whole set of the observed line intensities.

The well-known shape of the EM distribution in the quiet Sun is shown in Fig. 4.3. Different regimes of the upper solar atmosphere can be distinguished through the properties of the EM. Above the chromosphere, in the temperature range covering the lower transition region, the EM of the quiet Sun drops steeply, reaching a minimum value at around $\log T [\text{K}] \approx 5.2$. From this minimum toward higher coronal temperatures, in the upper transition region, the EM rises. It peaks at coronal temperatures of $\log T [\text{K}] \approx 6.0$, after which it sharply drops. The peak at $\log T [\text{K}] \approx 6.0$ defines the typical temperature of the quiet-Sun corona. In these distinct temperature ranges, namely the lower and the upper transition region, and the corona, the EM nearly follows three different power-law-like distributions, that intersect at the minimum and maximum values.

The general shape of the EM distribution can be understood to some extent in terms of static, one-dimensional models of coronal loops. As the real Sun is dynamic, this static picture may serve as a rough guideline to understand the distribution of plasma over temperatures. To describe this, we will follow the shape of the curve from higher to lower temperatures (right to left in Fig. 4.3). Assuming a constant heat input at the apex of the loop, the local plasma temperature will increase up to $\log T [\text{K}] \approx 6.0$. This results in the coronal peak in the EM, above which the EM drops, as there is very little hotter plasma. The local increase of the plasma temperature also creates a temperature gradient in the loop, which gives rise to thermal conduction of energy from the corona toward the loop footpoints, that host cooler plasma. This is the dominant energy loss mechanism in the corona and the upper transition region, down to $\log T [\text{K}] \approx 5.2$. Since the conduction depends both on temperature and the temperature gradient ($\propto T^{5/2} \nabla T$), in order to maintain a constant conductive flux, the temperature gradient must increase as we move from the coronal peak to lower temperatures. The increasing temperature gradient implies smaller volume of the emit-

ting plasma corresponding to a certain temperature bin (i.e., a very thin transition region). At the same time, as the temperature decreases, in an isobaric atmosphere the plasma density will increase. Still, the effect of this density increase is overpowered by the steep temperature gradient, hence the drop in the EM curve from $\log T [\text{K}] \approx 6.0$ to 5.2.

Moving to even lower temperatures from the minimum at $\log T [\text{K}] \approx 5.2$, the EM begins to rise. This cannot be reproduced with the models described above, as the transition region is too thin to emit the observed amount of radiation. This lack of emission from the transition region confined to the footpoints of large loops, together with the hints of structures on small scales, were the reasons behind proposing that unresolved, cool loops radiate the bulk of the transition region emission (Sect. 3.3.2). At these temperatures, thermal conduction is no longer the dominant energy loss mechanism, and the radiative losses are more significant. For optically thin radiation, as evident from the equation (4.7), the radiative losses increase with the density, hence the rise in the EM curve from $\log T [\text{K}] \approx 5.2$ to lower temperatures.

There are differences in the shape of the EM between the network and the internetwork emission, which are shown separately in Fig. 4.3, and which will be discussed in Ch. 5. The shape of the EM, and in particular its slope in the upper transition region, can be related to the properties of plasma heating mechanism in the corona, which will also be discussed in Ch. 5. In the earlier chapters, we discussed the motivation for the studies in this thesis (Ch. 1), and how the magnetic field permeates the solar atmosphere – from the footpoints at the surface (Ch. 2) to the hot structures in the corona (Ch. 3). After we covered the techniques for the plasma diagnostics with the optically-thin, EUV lines (Ch. 4), in the next chapters we will present our studies, where we explore the quiet solar corona organized in structured, compact loops (Ch. 5), and in apparently structureless and long-ranging diffuse emission (Ch. 6).

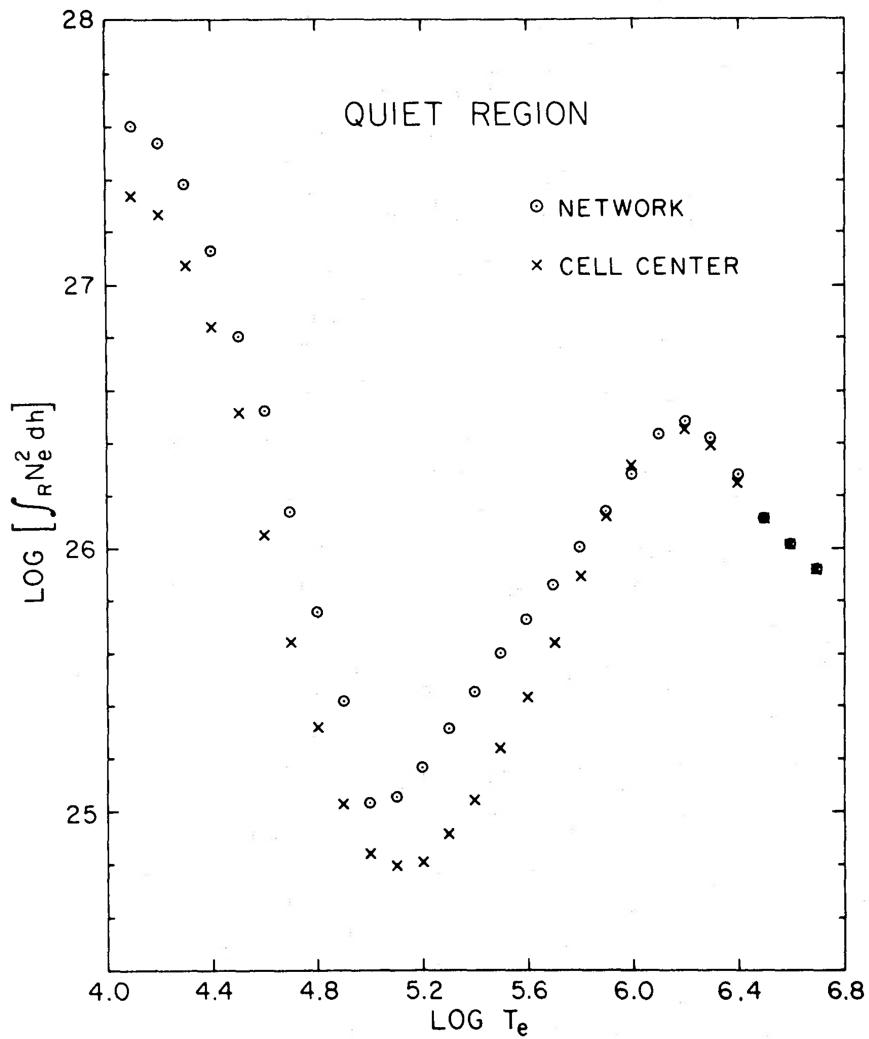


Figure 4.3: Emission measure of the quiet Sun. This figure shows the distribution of the EM [cm^{-5}] with temperature in the quiet Sun. The circles mark the measurements taken within the bright, supergranular network lanes, and the crosses within the darker interiors of the supergranular cells. The figure is taken from Raymond and Doyle (1981) © AAS. Reproduced with permission.

5 Thermal properties of coronal bright points

The upper atmosphere of the Sun is populated with bright loops, where plasma is confined to the magnetic field lines anchored in the photosphere. In Sect. 3.3.3 we discussed the coronal bright points – compact systems of loops associated with magnetic bipoles at the junctions of the magnetic network. These loops, bright in the EUV and sometimes in the X-rays, are coupled to their chromospheric footpoints that emit in the UV range. For that reason, studying the dynamics of bright points requires simultaneous spectral coverage of a broad range of plasma temperatures, which is not regularly available. How the bright points are thermally coupled through the solar atmosphere remains an outstanding issue, mainly due to this lack of simultaneous spectral observations spanning the solar atmosphere.

In this chapter, we study thermal structuring of the short loops in bright points in the quiet Sun. To cover a broad range of plasma temperatures – from the low transition region to the corona, we combine spectral data from SPICE with cotemporal images from AIA. The transition region emission lines observed with SPICE are, unlike with SOHO/SUMER, acquired simultaneously, which is important for these short loops that evolve on timescales of minutes. By performing a differential emission measure (DEM) analysis (Sect. 4.4), we found common behavior in all analyzed bright points, which can give insights into the heating of these short loops.

5.1 Observations and data processing

We identified bright points in the EUV spectroscopic data from transition region ($\log T [\text{K}] = 4.6\text{--}6.0$), in a quiet-Sun data set from SPICE. To investigate their characteristics at higher temperatures ($\log T [\text{K}] = 5.9\text{--}6.5$), we used coronal imagery data from AIA. For the magnetic field context, we used photospheric magnetograms from HMI in the same region.

5.1.1 Observational data

We used a large, dense raster¹ acquired on 28 May 2020 between 16:09 and 16:54 UT by SPICE on board the Solar Orbiter mission. At the time of these observations, Solar Orbiter was about 28° away from the Sun-Earth line, at a distance of about 0.565 astronomical units from the Sun. At that distance, $1''$ corresponds to ≈ 410 km on the Sun. The field of view is located in the quiet Sun and, from the Solar Orbiter point of view, close to the disk center (Fig. 5.1c). It is in the western hemisphere from the vantage point of the Earth (Fig. 5.1a). SPICE rastered an extent of about 210 Mm, with a $4''$ step size in the direction from west to east. The plate scale along the slit is $1.098''/\text{pixel}$, and the slit length corresponds to about 270 Mm. The spatial resolution along the slit is estimated to be $6.7''$ (Fludra et al. 2021), which here corresponds to about 2.8 Mm. This data set contains spectra of six transition region emission lines listed in Table 5.1. We show the C III (977 \AA) line intensity map (sum of the observed line profile) in Fig. 5.1c.

During the period of the SPICE raster, we used a time series of data from AIA.² We used the full-disk coronal images acquired by AIA in the EUV channels (see Table 5.1). The images are taken with a cadence of 12 s and have a plate scale of about $0.6''/\text{pixel}$. We also used the full-disk line-of-sight magnetograms acquired by HMI. These data have a cadence of 45 s and a plate scale of about $0.5''/\text{pixel}$.

Additionally, we used a longer time series of the SDO data that starts four hours before and ends about three hours after the SPICE raster. Here we used the HMI magnetograms, and the AIA images at 171 \AA , 193 \AA and 304 \AA , to follow the long-term evolution of the bright points. For this long time series covering about 8 hours, we used a reduced cadence of ca. 1.5 minutes (90 s for HMI, and 96 s or 84 s for AIA).

5.1.2 Preparation of data

We processed all the AIA data using the aiapy Python package (Barnes et al. 2020). The processing includes updating the image pointing information, rescaling the data to the plate scale of exactly $0.6''/\text{pixel}$, and removing the instrument roll angle. To simplify handling of different data sets and selection of features to analyze, we projected the HMI data onto the AIA coordinates and interpolated the HMI pixels to be identical to the AIA pixels. We did this by using the information given in the data headers and the routines

¹These data were obtained during the commissioning phase of the mission, and we used the version V05.

²All data from SDO are available at <http://jsoc.stanford.edu/>.

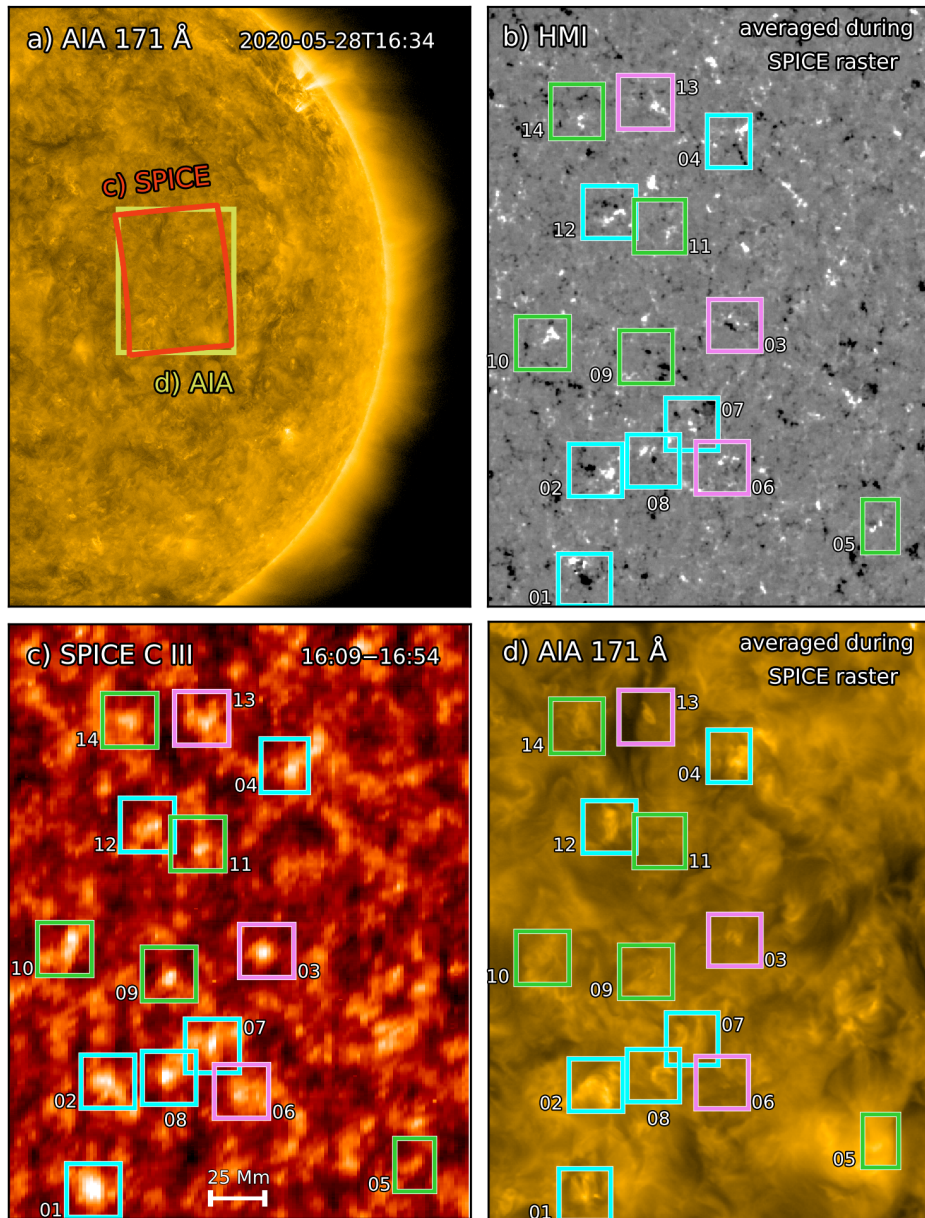


Figure 5.1: Overview of our observations. Panel a is a context image from AIA 171 Å, where the red box outlines the SPICE field of view, displayed in panel c (C III 977 Å intensity map). The corresponding SDO field of view is outlined with the yellow box, and shown in panels b (HMI line-of-sight magnetogram) and d (AIA 171 Å). The boxes in panels b–d (side length of ~ 24 Mm) highlight the 14 bright points we analyzed, which exhibited predominantly flux emergence (blue), flux cancellation (violet), or random motion of the footpoints (green; Sect. 5.3.2). The images in (a), (c) and (d) are in logarithmic scaling. The ones in (b) and (d) are averaged during the SPICE raster, and their evolution is available in an online movie, which spans eight hours centered around the SPICE raster (Sect. 5.1): <https://owncloud.gwdg.de/index.php/s/Bn6he2QRhY3elEb>

Table 5.1: Spectral lines and bands

	Line / band ^a	log T [K] ^b
	H I 1025.728 Å	4.00
	C III 977.020 Å	4.85
SPICE	S V 786.468 Å	5.20
	O IV 787.710 Å	5.15
	O VI 1031.912 Å	5.50
	Ne VIII 770.409 Å	5.80
	304 Å (He II)	4.92
	131 Å (Fe VIII) ^c	5.72
	171 Å (Fe IX)	5.91
AIA	193 Å (Fe XII)	6.18
	211 Å (Fe XIV)	6.27
	335 Å (Fe XVI)	6.40
	94 Å (Fe XVIII) ^c	6.86

Notes.

^a For the SPICE emission lines we list rest wavelengths from the NIST database (<https://dx.doi.org/10.18434/T4W3oF>), and for the AIA bands the primary contributing ions (Lemen et al. 2012).

^b For the SPICE emission lines, we list the temperatures from CHIANTI where the ion fraction peaks in ionization equilibrium. For the AIA bands, we list the peak temperature of the response function based on Peter et al. (2012), their Fig. 1.

^c The AIA 131 Å band also has a contribution around 10 MK from Fe XXI (Lemen et al. 2012), which is not relevant for the observations of the coronal bright points. On the other hand, the 94 Å band has a relevant contribution at around 1 MK from Fe X (cf. Table 1 of Martínez-Sykora et al. 2011).

available in the Python package SunPy (The SunPy Community et al. 2020). This ensures that HMI and AIA data are co-aligned and all have a plate scale of $0.6''/\text{pixel}$.

When comparing the data from SPICE to the ones from SDO, there are noticeable projection effects as a consequence of the instruments being at different heliographic longitudes. Here we aimed to measure the average intensity of small features, namely the loops that are roughly up to 20 Mm long, so that they do not reach sufficiently high to be severely affected by projection effects. Therefore, we used each data set in its original view plane (and plate scale) to perform the measurements, and avoided unnecessary interpolation of the data in a small field of view. We still made sure, for each analyzed feature, that the area selected for the analysis overlaps in all different passbands, as we discuss in Sect. 5.1.3. In Fig. 5.1b and 5.1d we show cutouts from an HMI magnetogram and an AIA 171 Å image in a field of view that nearly matches the one from SPICE. For illustration purposes, both images are produced by averaging individual frames during the SPICE raster period.

5.1.3 Selection of bright points

We identified several bright points in the C III intensity image (overplotted boxes in Fig. 5.1c). All of them have underlying small bipolar magnetic field regions in the photosphere (separation distance of 5–10 Mm; Fig. 5.1b). Likewise, they all have counterparts in the coronal images (Fig. 5.1d). In the following, we first explain how we selected the bright points in the SPICE data, and then the corresponding ones in the AIA data.

Bright points in the SPICE data

For our analysis, we selected features that appeared prominent in the transition region emission, located over the magnetic network. We selected 14 bright points in total, the selection of which was based on the brightness in the C III image from SPICE.³

We applied certain steps when extracting the emission of the bright points in the respective spectral lines, in order to reduce contamination of the line profile by the surrounding and background quiet-Sun emission. We started by placing a small box around the feature (e.g., box 01 in Fig. 5.1c,

³Despite being less prominent in the C III emission, we still added bright point 05 to the sample as it appeared very prominent both in the Ne VIII image from SPICE, and in the 171 Å channel from AIA (see Fig. 5.1d).

enlarged in Fig. 5.2a). Within it, we first selected pixels that have C III intensity lower than 30% of the brightest pixel value (pixels marked with green dots in Fig. 5.2a). We then obtained the background emission spectral profile by computing the average line profile from these pixels. We subtracted this background profile from all the pixels within the box. Then we selected pixels that have intensity higher than 70% of the brightest pixel value (on and inside the blue contour in Fig. 5.2a). Here we aimed to avoid the surrounding quiet-Sun emission, and included only a small area that belongs to the bright point in our analysis. We used these pixels to calculate the average C III line profile of the bright point itself, after the previously mentioned background subtraction (see Fig. 5.2b). We experimented with these thresholds, and found that our results are not sensitive to the exact values of the thresholds. Hence, we settled on values that give a good match when inspecting by eye.

After this, we calculated average profiles of all other spectral lines observed with SPICE for the same bright point. To do this, we used the C III image as a reference. This implies that in all emission lines we used the same pixels for the background estimation, or for the bright point itself, as the ones selected from the C III image (see Fig. 5.2d). In this way, we always used the same spatial area when calculating average line profiles for all the observed emission lines.

For a given bright point, we fitted each of the average line profiles with a single Gaussian by using the `curve_fit` function available in the SciPy Python package (Virtanen et al. 2020). Because of the limited spectral resolution of SPICE, S v and O IV are (slightly) overlapping in the spectral direction. Therefore, we fitted both these profiles, simultaneously, with a double Gaussian. From the fit parameters, we obtained the total line intensities, which we then used as an input for further analysis (Sect. 5.2.1).

Bright points in the AIA data

To analyze the same bright points in the AIA data, we first needed a representative AIA image that is nearly co-temporal to the corresponding SPICE raster. Since it takes about 5 minutes for SPICE to scan across a given bright point (e.g., boxed region in Fig. 5.1c), we used 26 consecutive snapshots of AIA to create an average intensity map of that bright point, in each respective AIA passband. This averaging also reduces the noise in AIA images, which is particularly necessary for channels with lower signal-to-noise ratio in quiescent regions (e.g., 94 Å, 131 Å, and 335 Å). Similarly, we averaged 7 HMI magnetograms (taken within ca. 5 minutes) to create an average magnetogram for each bright point.

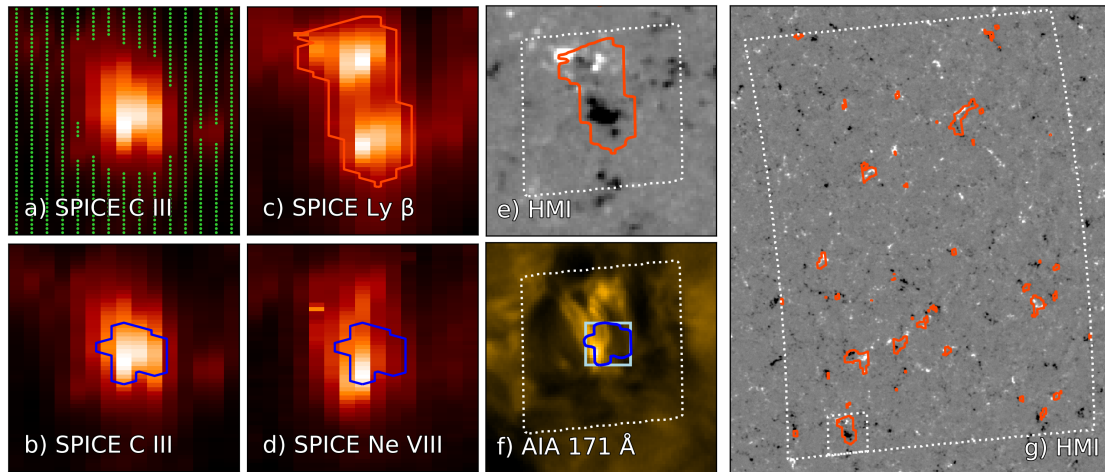


Figure 5.2: Bright point 01 through the solar atmosphere. We show the bright point 01 as recorded with different instruments and in different spectral ranges, as annotated. The green dots in panel a mark the pixels used to estimate the average background spectrum. The dark blue contour in panels b and d outlines the bright point pixels selected in the SPICE data. The orange contour in panel c outlines the brightening in $\text{Ly}\beta$, used to align the SPICE data to HMI. In panels e and f we overplot the contours from (c) and (d), respectively, after reprojecting them onto the AIA coordinate grid. The white, dotted quadrangle represents the field of view of panels a–d (roughly 24×24 Mm), after the reprojected. The light-blue box in panel f outlines the bright point pixels selected in the AIA data. In panel g we show the overlap between the various analyzed brightenings in $\text{Ly}\beta$ and the magnetic field concentrations across the whole field of view. See Sect. 5.1.3. All panels from SPICE and AIA are scaled linearly between minimum and maximum values.

We then spatially aligned the average AIA and HMI maps with SPICE. For this, we used the $\text{H I Ly}\beta$ raster image from SPICE and the average HMI magnetogram. The $\text{Ly}\beta$ line shows emission that originates from the upper chromosphere ($T \approx 10000$ K), while the HMI magnetogram shows the photospheric magnetic field. Bright chromospheric features, in general, are expected to correlate well spatially with the magnetic field concentrations in the photosphere. Furthermore, because both of these diagnostics reveal low-lying emission (i.e., from the photosphere or the chromosphere), they should be the least affected by the projection effects, making this magnetogram-image pair suitable for alignment.

To align the images, we reprojected the $\text{Ly}\beta$ image on top of the magnetogram using the routines from the Python package SunPy. To achieve a good overlap between the bright features and the magnetic field concentrations, we adjusted the WCS keywords (Thompson 2006) in the SPICE header.

Precisely, we set the values of $CRVAL1 = -77.707^\circ$, $CRVAL2 = -56.166^\circ$ and $CDELTA1 = 4.15''$. We decided on these values after visually inspecting the quality of the alignment. Additionally, we also accounted for minor offsets between the $Ly\beta$ and HMI regions of interest due to the solar rotation. The alignment is illustrated in Fig. 5.2g, where the curved, white quadrangle represents the SPICE field of view reprojected onto the HMI magnetogram. The orange contours outline the brightenings in the $Ly\beta$ image, which, after the alignment, coincide with the magnetic field concentrations across the whole field of view. This is best seen in the zoom into one particular bright point shown in Fig. 5.2e.

After the alignment, we reprojected the C III image on top of the AIA images in the same way as we did with $Ly\beta$ and HMI. We used this reprojected C III image only as guidance when selecting the bright points in the AIA images. As we illustrate in Fig. 5.2f with the 171 Å channel, we selected a box (light-blue rectangle) in the AIA image that nearly matches the pixels selected for the bright point analysis in C III (blue contour). We placed the same box in all other AIA channels, and calculated the average intensity within the box for each channel. These average intensity values we used in further analysis (Sect. 5.2.2). Varying the area of the bright point used for the analysis had no qualitative effect on our results (see Sect. 5.3.2).

5.2 DEM analysis of the bright points and the quiet Sun

We performed a DEM analysis to study the thermal properties of the bright points through the transition region (SPICE) and coronal temperatures (AIA). As we discuss below, we calculated the DEM separately for the SPICE and the AIA data, by using different techniques, developed by Young (2018) and Cheung et al. (2015), respectively. For the SPICE inversions and further calculations in this study, we use version 10.0 of the CHIANTI software and data package (Del Zanna et al. 2021; Dere et al. 1997).

We checked that these DEM inversion methods yield reasonable and expected results by computing the average quiet-Sun DEM, and comparing this to published values. To get the input intensities of the quiet Sun in different emission lines and channels, we spatially averaged the intensity over the whole SPICE and the corresponding AIA field of view. This quiet-Sun DEM was also used to provide context for the DEM of the bright points.

5.2.1 DEM with SPICE

We used the SPICE data to calculate the DEM in the temperature range between $\log T [\text{K}] = 4.6$ and 6.0 . One of the main assumptions when calculating the DEM is that the emission lines should form under optically thin conditions (Mariska 1992). The $\text{Ly}\beta$ line forms under more complex conditions, and does not fulfill the assumption of optically thin plasma, so we excluded this line. For each bright point, we used only the line intensities (as discussed in Sect. 5.1.3) of the remaining five emission lines from SPICE for the DEM analysis.

To calculate the DEM, we used an IDL-based software.⁴ From it, we employed the `ch_dem_linear_fit` routine, which assumes that the DEM is a piece-wise power law of the temperature. As discussed in Sect. 4.4, this choice is justified by the general appearance of the (differential) emission measure as a function of temperature in the quiet Sun (e.g., Raymond & Doyle 1981). In an iterative process, the routine finds the solution for the DEM that gives the closest match to the observed line intensities. For a more detailed explanation of the routine, see Young (2023). Examples of using piece-wise power-law DEM functions for the transition region were given by Young (2005, 2018) in relation to determining relative elemental abundances.

The DEM procedure takes line intensities and uncertainties as input. We estimated these uncertainties to be 20% of the total line intensity for each line. Because the spectra are averaged over the whole bright point, the photon noise and hence the error of the intensity integrated over the line profile should be significantly smaller (below 1%; see also appendix of Huang et al. (2023) for the measurement errors of SPICE). The systematic uncertainties are, however, expected to be larger and prevail in the total uncertainty of the line intensity. These include the uncertainties in the radiometric calibration, which we expect to be of the order of 15% (based on the estimate for SOHO/SUMER, whose observations were used as a reference for the radiometric calibration of SPICE; Wilhelm et al. 1997). Furthermore, there is contamination due to continuum radiation, in cases where wide spectral lines cover most of the available spectral pixels, and leave few measurement points in the continuum. This we estimated to be up to 15%. Finally, to cover different sources of uncertainties mentioned, we used this larger value of 20%.

With the lines that are available in our data set, we selected the temperature range of calculation from $\log T [\text{K}] = 4.6$ to 6.0 , covered by two

⁴Software available at https://github.com/pryoung/ch_dem.

power laws, matching at a minimum at $\log T [\text{K}] = 5.2$. For the initial values of the DEM in the three logarithmic temperature nodes $[4.6, 5.2, 6.0]$ we set $[1.0, 0.5, 1.0] \cdot 10^{22} \text{ cm}^{-5} \text{ K}^{-1}$. We performed the calculation for an isobaric atmosphere, by setting the pressure to a constant value through $n_e T = 10^{15} \text{ K cm}^{-3}$. In this way, we obtained the DEM distribution using the SPICE data, separately for each bright point and for the average quiet Sun.

5.2.2 DEM with AIA

We used the data from the EUV channels of AIA (listed in Table 5.1), excluding the 304 Å channel, to calculate the DEM in the temperature range between $\log T [\text{K}] = 5.9$ and 6.5. For this, we employed the IDL-based software developed by Cheung et al. (2015). By this, we first calculated the emission measure (EM) distribution over $\log T [\text{K}]$, from which we then calculated the DEM distribution.

To calculate the EM, we employed the `aia_sparse_em_solve` routine. This routine uses the observed intensities in the six EUV channels from AIA, together with the temperature response function of each channel, to solve for the EM distribution. The EM is represented in terms of a basis function and a set of coefficients that, when multiplied with the basis function, give the EM value in each temperature bin.

We supplied the routine with the average intensity value in each AIA channel (for one bright point or the average quiet Sun). We specified the temperature axis to span between $\log T [\text{K}] = 5.5$ and 6.5 with increments of 0.1. By using the keyword `bases_sigmas = [0, 0.125]`, we selected the basis functions used to represent the EM distribution over $\log T [\text{K}]$. In our case, for each temperature bin, the basis function was a combination of one Dirac Delta function and a truncated Gaussian of the width of 0.125 in $\log T [\text{K}]$.

The routine also requires an estimate for the intensity uncertainties, which are calculated by another routine, `aia_bp_estimate_error`. When calculating the uncertainties, we have taken into account the total number of pixels that were averaged for the intensity measurement (`n_sample` keyword). Since we averaged many pixels when calculating the input intensity, both during spatial and temporal averaging, this caused the calculated uncertainties to be almost negligible. These values were underestimated, however, because the systematic errors, e.g., due to uncertainties in the calibration, were not accounted for. Therefore, and in order to assure that the fitting routine will converge, we specified in `aia_sparse_em_solve` routine that the estimated uncertainties should be taken with a tolerance factor of 10 (`tolfac` keyword).

With the input AIA data and the parameters specified as above, we obtained the EM distribution. After that, we calculated the DEM distribution, by dividing the EM distribution with a factor of $T \cdot \ln 10 \cdot \Delta \log T$. Values of T and $\Delta \log T = 0.1$ correspond to the central value and the width of the temperature bin, respectively.

We tested how robust the resulting DEM is when varying the tolerance factor for the uncertainties. Using values between 1 and 50, we found that the resulting DEM varies significantly at temperatures below $\log T [\text{K}] \approx 5.9$. At higher temperatures, the results were consistent regardless of the tolerance factor. Based on this, we decided to consider the DEM calculated from the AIA data only at temperatures higher than $\log T [\text{K}] = 5.9$.

5.3 Results

Using the UV spectroscopic data from SPICE and the EUV images from AIA, we calculated the DEM of the average quiet Sun, and of the bright points we selected. The DEM inversions were performed separately for the transition region observations with SPICE, and for the coronal observations with AIA data. The input intensities for the bright points, necessary for the DEM inversions, were obtained as described in Sect. 5.1.3. The input intensities of the quiet Sun were obtained by spatially averaging the intensity over the whole SPICE raster map and the corresponding AIA field of view, in respective emission lines and channels. The details of the DEM inversions are described in Sect. 5.2. Finally, with the HMI magnetograms we followed the evolution of the surface magnetic fields underlying the bright points.

5.3.1 Quiet Sun DEM with SPICE and AIA

We calculated the DEM of the quiet Sun for the full field of view of SPICE, using both the SPICE and the AIA data (Sect. 5.2). We show the resulting DEM in Fig. 5.3. There, the two power laws show the result based on the SPICE data. This reflects the well-studied variation of the DEM as a function of temperature. Qualitatively and quantitatively, this is similar to previous quiet-Sun studies (e.g., Parenti & Vial 2007, their Fig. 2).

To double-check the piece-wise power-law DEM inversion, we calculated EM loci for the emission lines covered by SPICE. Essentially, EM locus is the total line intensity divided by the line contribution function. We calculated the appropriate contribution function for each transition, under the assumption of an isobaric atmosphere, by using the `ch_lookup_gofnt` routine available in CHIANTI software and data package (version 10.0; Del

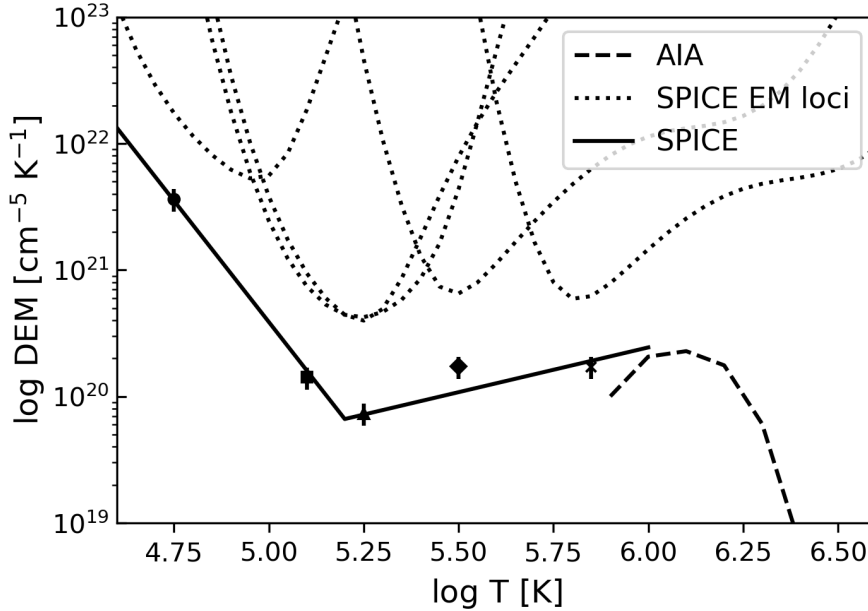


Figure 5.3: Differential emission measure of the average quiet Sun. The input intensity of the quiet Sun is spatially averaged over the whole SPICE (and the corresponding AIA) field of view. The solid line depicts the DEM profile derived from the SPICE data. Each emission line (see Table 5.1) is represented with a diamond at its effective line formation temperature, as derived with the DEM procedure. The offset of each diamond to the DEM curve indicates the ratio of the observed line intensity to the one derived from the DEM. The bars represent the errors of the observed line intensities. The dotted lines display the emission measure loci for the SPICE emission lines. The dashed line depicts the DEM profile as determined using the AIA data. See Sect. 5.3.1.

Zanna et al. 2021; Dere et al. 1997). The EM loci are shown as dotted curves in Fig. 5.3. For a single spectral line, the EM locus curve shows, at each temperature, the amount of plasma needed to emit the observed line intensity, should all the available plasma be at only that one temperature. For that reason, the lower envelope of the EM loci curves represents an upper boundary of the true emission measure, and the variation of this envelope should follow a trend similar to the DEM curve. This is what we see in our quiet Sun data in Fig. 5.3. Hence, we conclude that the DEM inversion based on the SPICE data is reliable.

The output DEM from the AIA data, shown with a dashed curve in Fig. 5.3, peaks at a temperature near 1 MK. Toward higher temperatures, the AIA DEM drops significantly. This trend reflects that, on average, there is little plasma hotter than 2–3 MK in the quiet corona, which is consistent with earlier studies (e.g., Morgan & Taroyan 2017). The cutoff of the AIA DEM be-

low 1 MK is due to the AIA filter responses not constraining well the plasma emission at lower temperatures (see Sect. 5.2.2). There, the SPICE measurements provide a better coverage. Essentially, the AIA quiet-Sun DEM level just below 1 MK transitions nicely into the level determined by SPICE observations. This smooth connection between the two temperature domains is reassuring.

Overall, by combining the data from SPICE and AIA, we were able to calculate the DEM of the quiet Sun between $\log T [\text{K}] = 4.6$ and 6.5. Our result in Fig. 5.3 is in qualitative and quantitative agreement with many earlier studies, such as Raymond and Doyle (1981) and Parenti and Vial (2007). This gives us a good foundation to study the DEM of other features, namely the bright points.

5.3.2 Properties of the bright points

We analyzed 14 bright points, that range in size between about 6 Mm and 10 Mm, based on the C III image. This size is within the expected range for coronal bright points (Madjarska 2019). Our data provided a broad thermal coverage of these features, as we illustrate in Fig. 5.4. There we show the bright point 01 in all the different spectral ranges and emission lines available in our data. In the following, we summarize the main morphological, thermal and magnetic properties of the features we analyzed.

Bright points in the coronal images

The majority of the analyzed bright points, represented by short loops, are persistent in the coronal images for several hours. To illustrate this, we supplement a movie to Fig. 5.1. These loops are clearly visible in the average images from AIA we made for the three example bright points 01, 02, and 03 (see AIA panels in Figs. 5.4, 5.6, and 5.7), which are among the brightest in our sample. The longest loops we identified are about 12 Mm (e.g., bright point 01). The smallest ones are down to 2–4 Mm (e.g., bright point 03).

A few of the bright points, however, remain mostly quiet during the time series we studied, with faint EUV emission in the coronal images, (e.g., bright points 06, 09, and 11). They stand out more prominently above the background only during short periods of time, when they exhibit bursts of EUV intensity enhancements, that last between roughly 5 and 20 minutes. Some of these bursts were caught by the SPICE slit, and correspond to the bright points we selected in the C III raster image, while overall they are not prominent in the coronal emission.

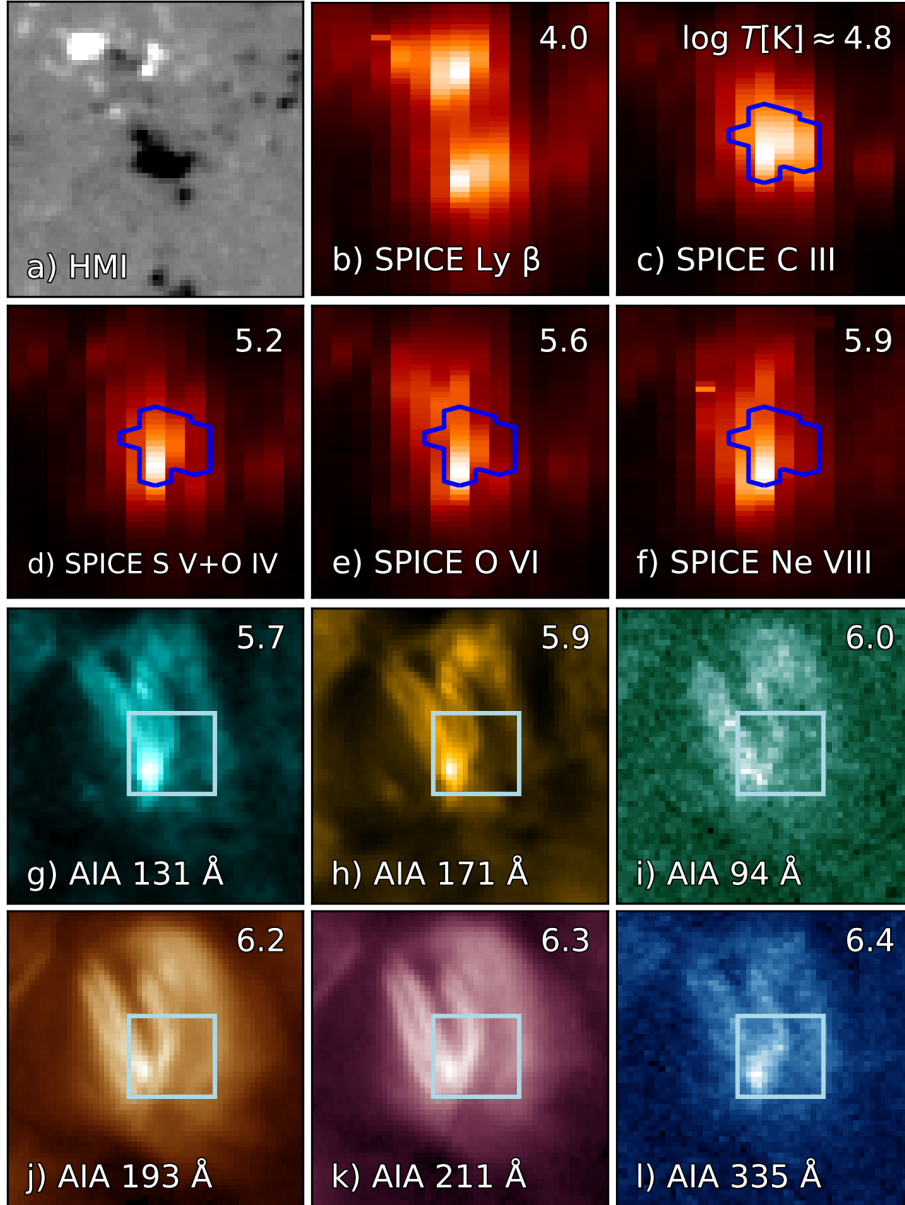


Figure 5.4: Overview of the bright point 01 observations. We show spectral and imaging diagnostics, along with the surface magnetic fields, for bright point 01, as labeled in each panel. Both the SPICE and the SDO data are shown in their original view plane and plate scale, and images are scaled linearly between minimum and maximum values. The SPICE panels have a size of about 24×24 Mm. In the top right of each panel, we indicate the temperature (in $\log T$ [K]) of the plasma for which the emission line or channel has the highest sensitivity (Table 5.1). The SDO data are averaged over about 5 minutes, during which time the SPICE slit crossed the bright point. The dark blue contours and the light-blue boxes highlight the pixels selected for the analysis of the bright point, as discussed in Sect. 5.1.3.

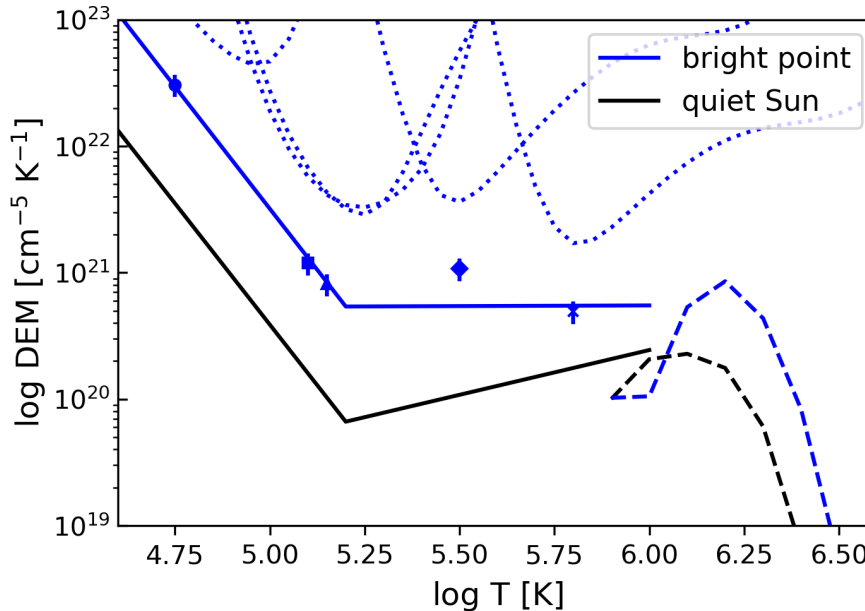


Figure 5.5: Differential emission measure of the bright point 01 compared to the quiet Sun. The quiet-Sun DEM is computed for spatially averaged intensity over the whole SPICE (and the corresponding AIA) field of view. The choice of the different line styles is the same as in Fig. 5.3. The results are represented with blue lines for the bright point, and black lines for the quiet Sun. See Sect. 5.3.2.

The nature of the SPICE data, in the form of a large raster, prevents us from checking if these features show similar transient behavior also at transition region temperatures. Some insight into this could be gained from the AIA 304 Å channel, which at moments shows loop-like features, but generally has a more patchy appearance and evolves more rapidly than the coronal channels. The formation of the He II line that dominates the 304 Å band is, however, more complicated than the optically thin transition region lines predominantly excited by electron collisions. Therefore, any quantitative conclusion about the variability of the transition region plasma based on the 304 Å channel is difficult (e.g., Andretta & Jones 1997). In particular, we cannot use the 304 Å channel for the following DEM analysis using AIA data.

DEM of the bright points

We calculated the DEM of the bright points, as discussed in Sect. 5.2. As above, we show the same three example bright points 01, 02, and 03. The DEM of the bright point 01 is enhanced at all observed temperatures, when compared to the quiet Sun (Fig. 5.5). Furthermore, the peak of the DEM at the high-temperature end (covered by AIA) shifts to higher temperatures

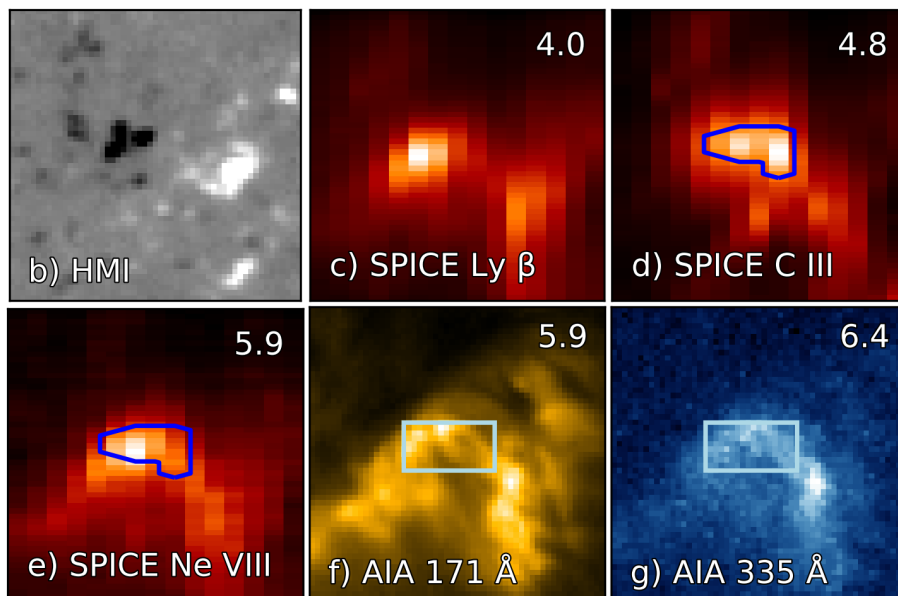
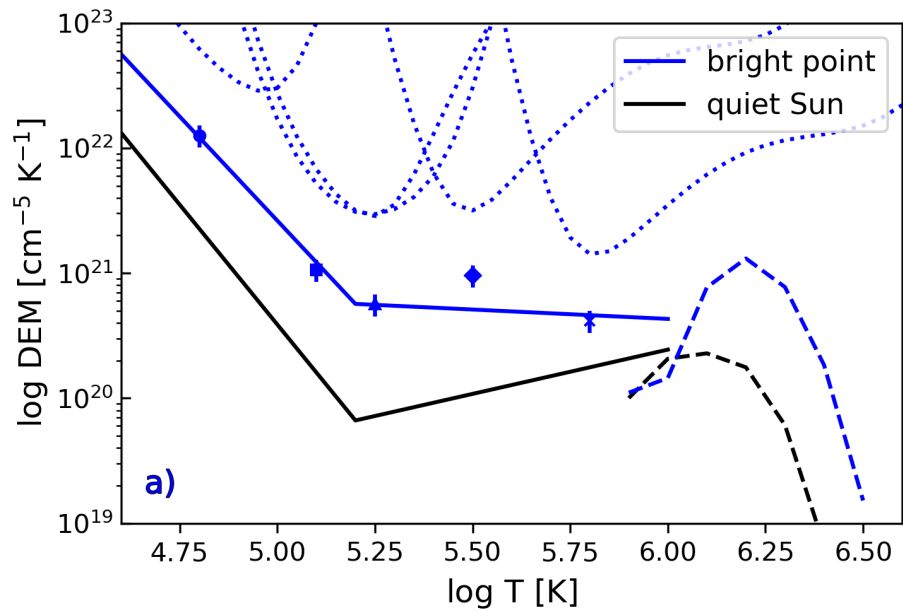


Figure 5.6: Overview of the results for the bright point 02. In panel a we show the DEM of the bright point compared to the quiet Sun (similar to Fig. 5.5; see Sect. 5.3.2). In panels b–g we show the bright point observations from different instruments and spectral ranges (similar to Fig. 5.4; see Sect. 5.1.3).

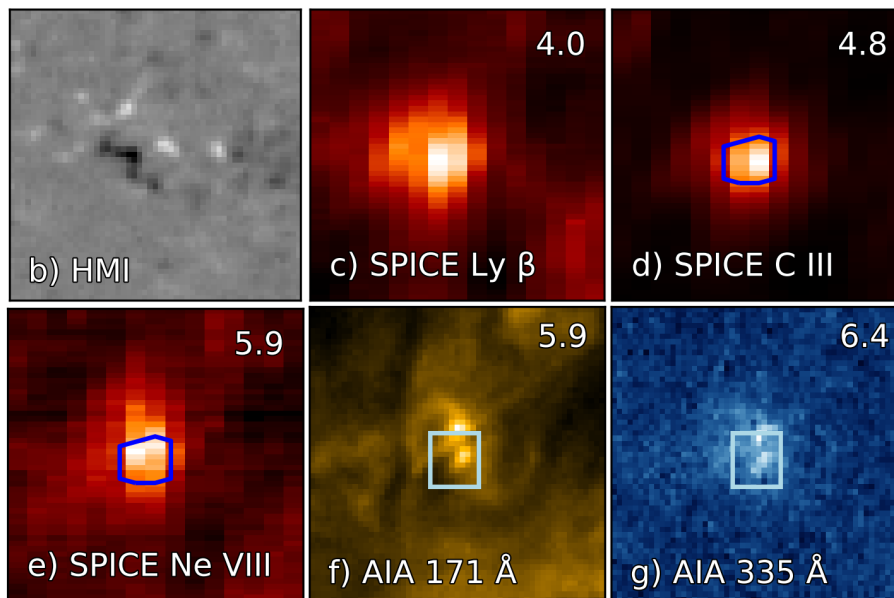
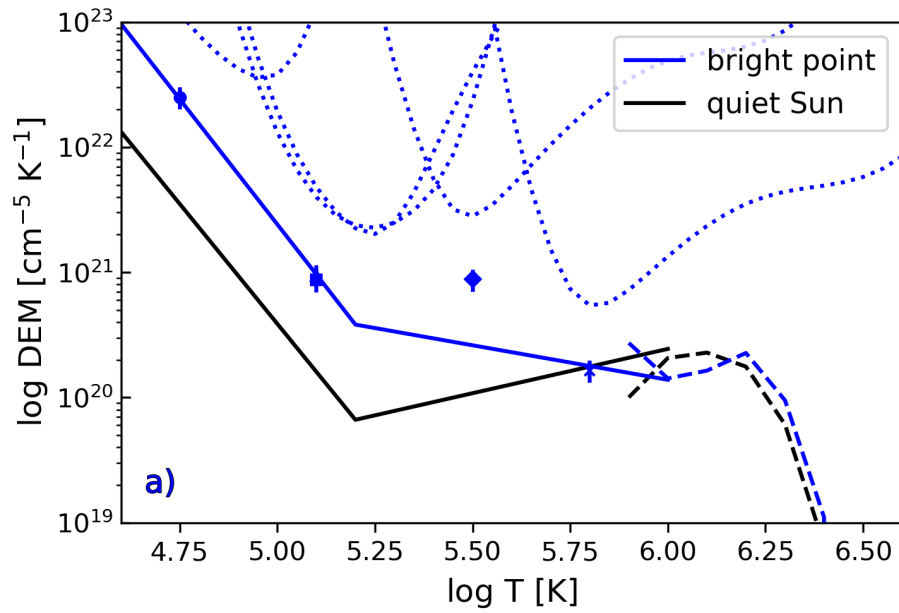


Figure 5.7: Overview of the results for the bright point 03. The layout of the panels is like in Fig. 5.6. See Sect. 5.3.2.

from $\log T \text{ [K]} \approx 6.1$ in the quiet Sun, to 6.2 in the bright point.

The factor by which the DEM is increased in the bright point (in comparison to the quiet Sun), however, is not the same at all temperatures. At the low-temperature end, in the lower transition region below $\log T \text{ [K]} \approx 5.2$, the bright point and the quiet Sun have a similar, negative slope of the DEM (of about -4). In the upper transition region, above temperatures of $\log T \text{ [K]} \approx 5.2$ and up to $\log T \text{ [K]} \approx 6.0$, the slopes of the two are quite different. Here, the quiet-Sun DEM has a clear positive slope (of about 0.7), while the bright point DEM shows only little change (slope close to 0). Certainly, in the bright point, the increase of the DEM towards the corona (if present at all) is significantly less steep than in the quiet Sun.

Other bright points in our sample share the above characteristics with the example 01. The slope and the values of the DEM in the lower transition region, in particular, are quite similar for all the bright points (see Table 5.2). Furthermore, they all show a flat or even a negative trend of the DEM in the upper transition region. This is evident when comparing bright point 01 with cases 02 and 03, which are shown in Fig. 5.6a and Fig. 5.7a.

At and above $\log T \text{ [K]} \approx 6.0$, often the peak of the DEM is shifted to higher temperatures, and the peak value is higher than for the quiet Sun (as for BPs 01 and 02). Still, even if the bright point DEM is at a higher level at $\log T \text{ [K]} \approx 6.0$ than in the quiet Sun, the gradient of the DEM in the upper transition region is more shallow in the bright points. About half of the cases do not show an enhanced DEM at $\log T \text{ [K]} \approx 6.0$ at all, and hence often show even a negative slope, i.e., a drop, of the DEM in the upper transition region towards higher temperatures. This is illustrated by the example of bright point 03 in Fig. 5.7a. This bright point, although very prominent in the transition-region emission (Fig. 5.1c), does not stand out in coronal emission, when compared to the background quiet Sun in the large field of view shown in Fig. 5.1d. Hence, the DEM of this bright point around 1 MK is comparable to the average quiet Sun as seen in Fig. 5.7a. Still, in the local surroundings of the bright point, where the coronal quiet-Sun emission is particularly low, the coronal loops in the bright point can be identified clearly (Fig. 5.7f).

There are limitations to our results of the DEM. To select the bright points in the SPICE image, we needed to set intensity thresholds (Sect. 5.1.3), which might have affected our results. We tested different thresholds for the bright point 01, which resulted in selecting a smaller or larger area of the bright point for the analysis, in SPICE, and consequently in AIA data. While this caused the overall DEM curve to shift up or down (due to the increased or decreased average intensity), it did not affect the general trends we dis-

cussed above. Furthermore, our results are limited by the available diagnostics, in particular the five emission lines from SPICE we used to study the DEM in the transition region. Differences in the DEM between the bright points might not have been fully revealed with the data we have. This can be improved by selecting emission lines that more finely and evenly sample the studied range of temperatures in new studies of SPICE. We do not expect major changes of the results, however, because our result for the quiet-Sun DEM is in good agreement with earlier studies.

In summary, we find that all bright points show an increase of the DEM in the lower transition region ($\log T [\text{K}] < 5.2$), and keep the same slope of the power law when compared to the average quiet Sun. In contrast, in the upper transition region ($5.2 < \log T [\text{K}] < 6.0$) the gradient of the DEM is much more shallow in the bright point, with a DEM sometimes even decreasing toward higher temperatures. In only about half of the bright points the DEM in the coronal part ($\log T [\text{K}] > 6.0$) is increasing, and peaking at higher temperatures as compared to the quiet Sun. In the other half of the cases, the coronal part of the bright point DEM is very similar to the quiet-Sun one, i.e. the bright point is less prominent in the coronal than in the transition-region data.

Relation of bright points to the photospheric magnetic field

To study the magnetic driving of the bright points in relation to their thermal properties, we followed the evolution of their magnetic flux content, particularly prior to the observation with SPICE. We did this by using the aforementioned time series of the SDO data, which starts four hours before the SPICE raster, and runs for 8 hours in total. By (initially) visually inspecting the photospheric magnetograms, we recognized different processes in the magnetic footpoints of the analyzed bright points, namely magnetic flux emergence, flux cancellation and random motion of the footpoints. For the example bright points 01, 02, and 03, we show three snapshots of their magnetograms in the top panels of Fig. 5.8.

In the time leading up to the SPICE observations, bright point 01 shows very prominent flux emergence. In fact, the beginning of its emergence is captured in the SDO time series we analyzed. Its unsigned magnetic flux (black curve in Fig. 5.8a) increases between hours 2 and 6, with a rate of about $0.15 \cdot 10^{20} \text{ Mx h}^{-1}$, after which it saturates to a value of about $1.3\text{--}1.4 \cdot 10^{20} \text{ Mx}$. At the time when the SPICE slit crossed over the bright point (vertical red line), the flux emergence was still ongoing. This bright point contains the highest amount of magnetic flux within our sample, with its value being at the higher end of what is considered a coronal bright point, nearing to

Table 5.2: Summary of the bright point properties

Bright point	DEM slope lower TR ^a	DEM slope upper TR ^b	Coronal log T [K] ^c	Magnetic signature ^d
01	-3.9	+0.0	6.22	E
02	-3.3	-0.2	6.23	E
03	-4.0	-0.6	6.14	C
04	-3.3	+0.1	6.17	E
05	-3.5	+0.1	6.12	R
06	-3.7	-0.3	6.13	C
07	-3.2	-0.4	6.15	E
08	-3.6	-0.4	6.19	E
09	-3.4	-0.4	6.15	R
10	-3.1	-1.8	6.14	R
11	-3.2	-0.9	6.12	R
12	-3.6	-0.6	6.16	E
13	-3.3	-0.9	6.14	C
14	-3.5	-0.5	6.12	R
QS ^e	-3.8	+0.7	6.14	

Notes.

^a Slope of log DEM with log T [K] in the lower transition region ($4.6 < \log T$ [K] < 5.2), based on SPICE data.

^b Same in the upper transition region ($5.2 < \log T$ [K] < 6.0).

^c EM-weighted temperature in the range of $5.9 < \log T$ [K] < 6.5 , based on AIA data.

^d Magnetic process exhibited by the footpoints prior to the SPICE observation (E – emergence, C – cancellation, R – random motions; Sect. 5.3.2).

^e Quiet-Sun measurement for comparison.

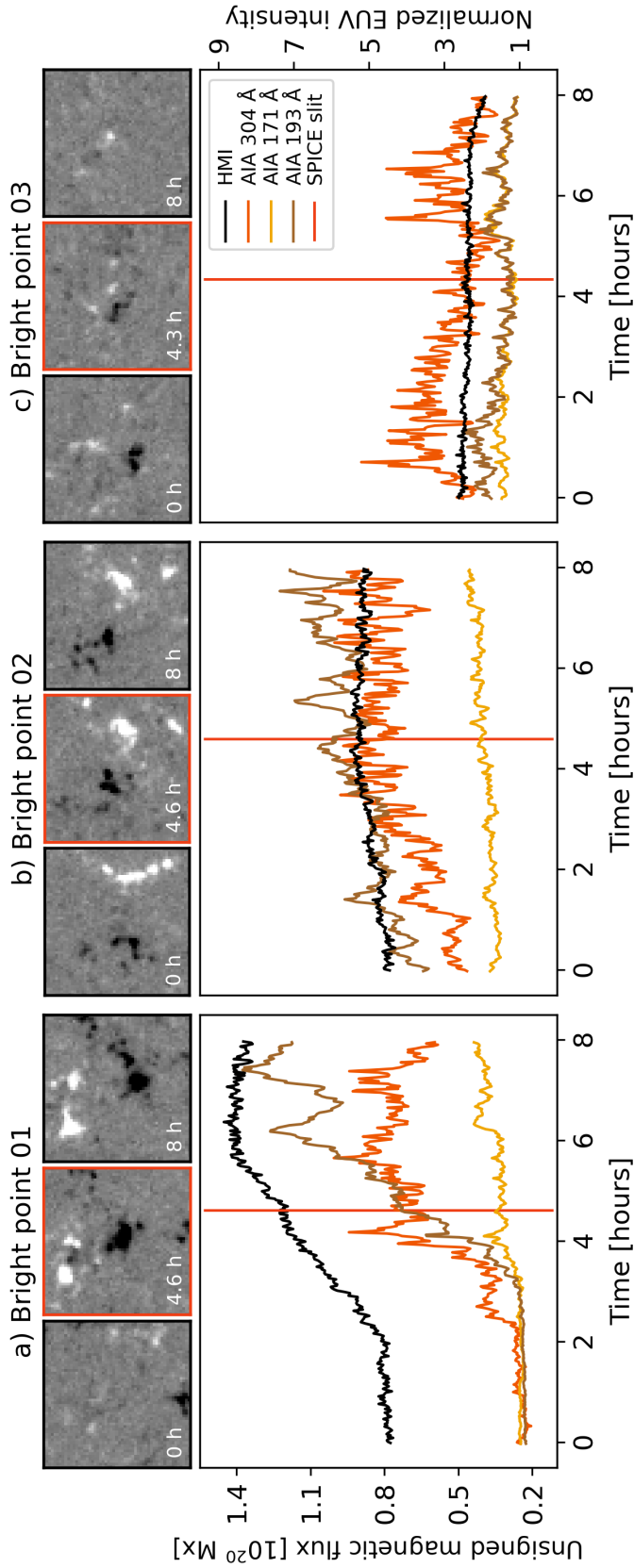


Figure 5.8: Evolution of bright points 01, 02 and 03 over the course of 8 hours. In the bottom panels, the orange, yellow, and brown curves depict the variation of the EUV intensity in a specific AIA channel, spatially averaged within the box used to calculate the DEM (cf. light-blue boxes in Fig. 5.4g–l), and normalized to the average quiet-Sun value in the total field of view. The SPICE raster takes place between hours 4 and 4.75, and the vertical red line indicates the time when the SPICE slit crossed over a specific bright point. The black curve depicts the variation of the total unsigned magnetic flux, integrated in the field of view shown in top panels, including only pixels with signal above the noise level of 10 G. The top panels show snapshots of the line-of-sight magnetogram from HMI, saturated at ± 100 G. The snapshots correspond to the beginning, mid-time and the end of the 8-hour time series (Sect. 5.1), and cover a field of view of about 24×24 Mm (like in Fig. 5.4a). The evolution of these magnetograms is also available as an online movie at: <https://owncloud.gwdg.de/index.php/s/Bn6he2QRhY3eIEb>

the flux range of small active regions (see e.g., Mou et al. 2016, their Fig.2). Its rate of growth of the magnetic flux is also 2–3 times larger than in a typical coronal bright point ($1.5 \cdot 10^{15} \text{ Mx s}^{-1} \approx 0.05 \cdot 10^{20} \text{ Mx h}^{-1}$; Golub et al. 1977; Madjarska 2019), making this case exceptional in that sense.

Several other bright points also show flux emergence prior to the SPICE observation (blue boxes in Fig. 5.1b–d), including bright point 02. Its magnetic flux grows until some 4.5 hours, with a rate of about $0.03 \cdot 10^{20} \text{ Mx h}^{-1}$ (Fig. 5.8b), which is somewhat lower than the typical value for coronal bright points. This feature was, however, already present at the beginning of the SDO time series. A more dynamic emergence phase happened ≈ 9 hours before that, after which the magnetic footpoints exhibited mostly random motions.

Some bright points from our sample show flux cancellation before the SPICE raster (violet boxes in Fig. 5.1b–d). As an example of these, we show bright point 03 in Fig. 5.8c. Its magnetic flux gradually decreases over time (by about $0.01 \cdot 10^{20} \text{ Mx h}^{-1}$), which could be related to the flux cancellation. The absolute value of this rate of change is significantly smaller than for the other two examples we show. The flux is still consistently diminishing over the course of our observation, as is also evident from the snapshots of magnetograms (top panels of Fig. 5.8c). We note here that the ongoing magnetic processes are often, except in very prominent cases like bright point 01, better visible from the evolution of magnetograms than from the magnetic flux curves. It is, therefore, difficult to objectively grasp the magnetic evolution of bright points, and to identify the most relevant processes.

Other bright points in our sample (green boxes in Fig. 5.1b–d) show predominantly random motion of the magnetic field concentrations. We do not find systematic change of the magnetic flux in these cases, and any processes other than shuffling of the magnetic elements are hard to recognize in the magnetograms. These may still be present at smaller scales, below the resolution power and sensitivity of HMI, similarly as opposite (parasitic) polarities can be found at the footpoints of coronal loops when observing at very high resolution (Chitta et al. 2017).

In all bottom panels in Fig. 5.8 we overplot the curves of the average EUV intensity in different AIA channels on top of the unsigned magnetic flux. The magnetic flux growth in bright point 01 is clearly followed by the general increase of the coronal emission. In case of bright point 02, which is already emerged at the beginning of the time series, the EUV emission fluctuates well-above the average quiet Sun, with a noticeable positive trend, maybe related to the flux emergence. The coronal emission in bright point 03, with the least magnetic flux of the three examples, fluctuates at a lower

rate, with a subtle declining trend that could be related to the diminishing magnetic flux.

On top of the general trends, there are smaller variations of the magnetic flux and the EUV intensity, between which it is harder to find a direct causation. We note here that the expected measurement error for the EUV intensity shown in Fig. 5.8 is at most 2–3 counts per pixel in each channel. We estimated this value by using the routines available in the `aiapy` Python package, equivalent to the `aia_bp_estimate_error` routine from SolarSoft. It corresponds to ~ 0.01 in the normalized intensity scaling we use in the figure, which is significantly smaller than the short-term variability seen in the EUV curves. Hence, the short-term EUV variability in Fig. 5.8 should be of solar origin.

In conclusion, the 14 bright points we identified show different magnetic processes at their base. Roughly two thirds show either flux emergence or flux cancellation prior to the SPICE observation, while the rest show only reshuffling of the magnetic elements at their footpoints, without major signatures of either flux emergence or cancellation. While there are limitations present both in the computed DEM and in the accurate identification of the relevant magnetic processes, all analyzed bright points show very similar enhancement and trend of the DEM in the lower and the upper transition region (Sect. 5.3.2), regardless of the ongoing magnetic processes, or the amount of magnetic flux available to the bright point prior to the DEM evaluation.

5.4 Discussion

We find that all bright points show a similar increase of the DEM at all temperatures from below 0.1 MK up to about 1 MK as compared to the quiet Sun. An increase of the DEM in a given temperature bin generally implies higher plasma density at the respective temperature. This is expected for bright points, as they stand out above the background emission in different transition region and coronal images (e.g., Fig. 5.4). When present, the shift of the coronal DEM peak toward higher temperatures above 1 MK indicates an increase of the coronal temperature in these features. In the following, we will discuss implications of our results for the heating processes acting in the bright points.

5.4.1 Bright points DEM in the lower transition region

In the lower transition region (below $\log T \text{ [K]} \approx 5.2$), the DEM of the bright points is increased when compared to the quiet Sun. The increase is such that the DEM maintains a (negative) slope similar to that found in the quiet Sun. This implies that the plasma at a given temperature has a density in the bright point that is higher than in the quiet Sun. The increased density implied by the DEM could have various sources.

One possible source is heating acting at higher, coronal temperatures, with the transition region being maintained via thermal conduction of energy deposited in the corona. This will shift the transition region downwards towards higher densities (e.g., Hansteen & Leer 1995). However, in a 1D model the energy balance will generally not lead to the observed slope of the DEM in the lower transition region, i.e. the steep increase of the DEM towards the chromosphere (e.g., Athay 1982).

Alternatively, plasma can be supplied to the lower transition region by the heating events initiated at still lower temperatures. There, various types of jet-like features, which are commonly associated with the chromospheric network, should have an impact. In particular, (type II) spicules (Bose et al. 2023; Pereira et al. 2014) and network jets (Gorman et al. 2022) are expected to contribute to the upper atmosphere, although their share remains an open question (Klimchuk 2012). Additionally, Judge et al. (1997) considered upward-propagating acoustic shock waves, and concluded that these do not contribute significantly to the heating of the lower transition region.

Finally, the excess emission in the lower transition region could be, at least partially, explained by short, cool (nested) loops. Loops at lower temperatures up to $\sim 10^5$ K, thermally isolated from the hotter coronal plasma, were suggested to be an additional source of transition-region emission near the footpoints of long, hot loops (Antiochos & Noci 1986; Dowdy et al. 1986; Feldman 1983). The contribution of short loops might be significant in the quiet-Sun network (Judge & Centeno 2008; Wiegmann & Solanki 2004). They are expected and have been found to evolve rapidly, because of the efficient radiative cooling (Hansteen et al. 2014). In coronal bright points, however, any present cool loops should be of similar length as the hot loops (like in the model by Nóbrega-Siverio & Moreno-Insertis 2022). While hot loop-like features were observed many times in coronal data, in the transition region, because of the lack of instrumentation to resolve them, similar observations are rare (e.g., Kayshap & Dwivedi 2017; Madjarska et al. 2021; Teriaca et al. 2004). Clear loops are not resolvable in the SPICE data we used. Instead, in Fig. 5.9 we show loop-like features in bright point 01 in different AIA channels, that seem to co-exist at po-

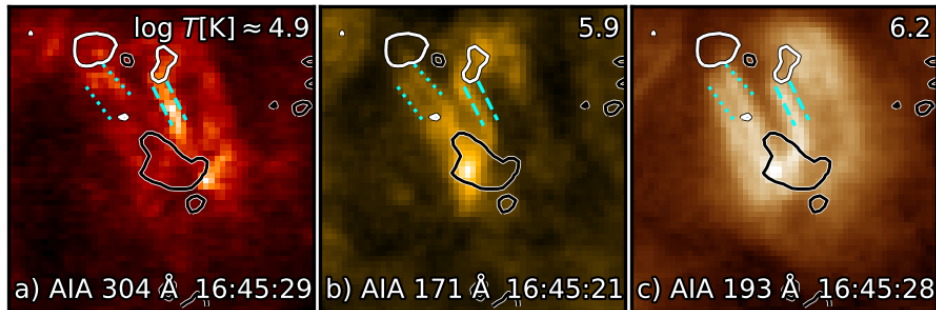


Figure 5.9: Loops in bright point 01. We show single snapshots of bright point 01 in different AIA channels, as labeled in each panel. We indicate in the top right the temperature of plasma (in $\log T$ [K]), for which the channel has the highest sensitivity (Table 5.1). The field of view is like in Fig. 5.4, and the images are scaled linearly between minimum and maximum values. The black and white contours in all panels outline the magnetic field from HMI at values of -50 G and $+50$ G, respectively. The dashed and dotted blue lines highlight loop-like features from 304 Å and 171 Å channels, respectively, as discussed in Sect. 5.4.1.

tentially different temperatures, and not to overlap entirely. These short loops, although probably thermally isolated from one another, should still be related through motions and interactions of their footpoints. While it is reasonable to assume that spicules, jets, and cool loops are all contributing to the emission in compact, network features, such as coronal bright points, disentangling the impact of each component remains a challenging task.

5.4.2 Bright points DEM in the upper transition region

Also in the upper transition region ($5.2 < \log T$ [K] < 6.0), bright points show a higher DEM compared to the average quiet Sun. Unlike in the lower transition region (Sect. 5.3.2), in this temperature range the slope of the DEM is shallower in the bright points. This finding suggests that there is a depletion of the DEM in bright points at coronal temperatures, in comparison to the lower temperatures.

This could be a selection effect, because we selected the bright points based on the increased emission in the transition region (but not in the corona). It is therefore an interesting question whether this trend of the DEM is only a transient phase, especially since we do not have access to temporal evolution of the transition region emission. We find this unlikely, as the flat DEM in the upper transition region is a common property of all the cases we analyzed, which most likely will be in different phases of their evolution. This is further supported by the fact that the features are

well-scattered across the field of view that covers several supergranular cells, which makes it unlikely that they are all correlated and in a common or similar phase of evolution.

In our study, the bright points correspond to the brightest locations in the magnetic network lanes, and the average quiet-Sun emission includes both the network lanes and the cell interiors. The trend of the DEM in the upper transition region we found is consistent with an earlier study by Raymond and Doyle (1981), who analyzed the DEM of the bright magnetic network lanes, and of the darker cell interiors in the quiet Sun. These authors showed that, when compared to the cell interiors, the network lanes have higher DEM at all temperatures, and a flatter trend in the upper transition region (cf. Fig. 4.3). Similar DEM trends in network lanes and cell interiors were also reported in studies by Griffiths et al. (1999) and O’Shea et al. (2000).

Many studies measured the slope of the EM in active-region loops. There, the EM distribution follows a power law $EM(T) \propto T^\alpha$ from $\log T [\text{K}] = 6.0$ up to the coronal peak at $\log T [\text{K}] \approx 6.5$. Values of α found in different active regions span a broad range between roughly 2 and 5 (e.g., Warren et al. 2012). The power-law $EM(T) \propto T^\alpha$ could be considered equivalent to $DEM(T) \propto T^{\alpha-1}$. Based on this simple conversion, the slopes we found for the bright points roughly span the range of $0 < \alpha < 1$. Hence, the slopes in the bright points are significantly flatter than in the active regions, as observed in earlier studies (e.g., Griffiths et al. 2000).

5.4.3 Implications on the frequency of heating

The slope of the EM is often used as a proxy to investigate properties of heating mechanisms acting in active region coronal loops. The power law $EM(T) \propto T^\alpha$ in the upper transition region, with $\alpha > 0$, arises naturally in models where plasma is heated to coronal temperatures of more than 1 MK, with plasma at lower temperatures being supplied during the subsequent cooling phase. There, the positive slope of the EM generally reflects the shape of the radiative losses function, as pointed out in the analytical study of nanoflare heating by Cargill (1994). Compared to the scenario we discussed in Sect. 4.4, this is a time-dependent model with intermittent heating. Since the radiative losses increase toward lower temperatures (due to the increased density in the atmosphere), this results in plasma cooling quicker through the lower temperatures and spending little time in a cooler state.

The amount of time the plasma is found at certain temperatures, and

hence the shape of the EM, also depends on how often the plasma is heated (Sect. 3.4.2). If the heating is episodic (low frequency of variable heating), the waiting time between two heating events is longer than the typical cooling timescales in the corona (a few tens of minutes for plasma at ca. 1 MK). This allows the hot plasma to cool and hence increase the density at lower temperatures. In case of steady (or high frequency) heating, it is the opposite, so that the plasma is maintained at higher temperatures without the chance to cool between two heating pulses.

Consequently, the frequency of the heating will affect the steepness of the EM in the upper transition region. The connection between the slope of the EM and the heating frequency was studied, for example, in the scope of the nanoflare heating models. It was demonstrated that trains of low-frequency nanoflares correspond to slopes of $\alpha \sim 2$, while the high-frequency ones can account for larger slopes, which are also seen in observations (e.g., Warren et al. 2011). Nevertheless, introducing trains of non-equally spaced (and non-equally energetic) nanoflares can also reproduce a broad range of slopes (Cargill 2014). This is still an area of active research (Del Zanna & Mason 2018).

The slopes we found for the bright points roughly span the range of $0 < \alpha < 1$, while the average quiet Sun shows a slope of $\alpha \approx 1.7$. Following the assumption that lower values of the slope correspond to lower frequency of heating, we speculate that the heating in the bright points is of lower frequency than in the quiet Sun. In other words, while on average the quiet solar corona is heated steadily, the bright points undergo episodic and more energetic heating events. However, the models mentioned above, on which our conclusion is based, to our knowledge never produced slopes in range $0 < \alpha < 1$. Furthermore, the quiet-Sun network we observed might require input parameters for the models that are quite different from the ones appropriate for the active regions. Apart from the obviously different loop lengths and their (presumably) different cross-sectional widths, we suppose that also the average coronal energy losses, and the energy of the individual nanoflares, might be different in case of the quiet-Sun loops. Chitta et al. (2013) and Mondal et al. (2023) modeled loops in coronal bright points using zero-dimensional hydrodynamic simulations, but none of these studies covered fully the transition region emission. Clearly, more work is needed to interpret the slopes we observe in terms of the heating frequency.

Finally, the nanoflare heating models (implicitly) assume that the amount of plasma existing at coronal temperatures (over 1 MK) and in the upper transition region is a consequence of the same heating events (nanoflares) in the corona, and is in that way related to each other. However, in contrast

to the nanoflare heating models, we can also imagine that the plasma in the two temperature domains (around $\log T [\text{K}] \approx 5.0$ and at $\log T [\text{K}] \approx 6.0$) evolves separately. Then the slopes that we observe in the DEM cannot be explained through varying frequency of the heating events. This dichotomy was already recognized in the observations of coronal bright points, for example in the studies by Tian et al. (2008) and Doschek et al. (2010). There could be loops at different temperatures, that are thermally independent (in some respects similar to early suggestion by Dowdy et al. 1986, whereas the loops in bright points are all of similar length). Observations that cover the evolution of a bright point over a few hours, both in the transition region and in the corona, would certainly provide more information to address this problem.

5.5 From bright points to diffuse coronal features

In this chapter, we studied the bright points – small loops in the magnetic network of the quiet Sun, related to compact magnetic bipoles. We examined the thermal properties of bright points by using observations that cover a broad range of plasma temperatures. We found systematic behavior of the DEM in all the studied bright points, regardless of their magnetic flux content, phase of evolution, or the exact magnetic processes exhibited by their footpoints. Our results can provide insights into the nature of plasma heating in the bright points, and suggest that the bright points undergo stronger, less frequent heating episodes than the quiet Sun on average. Instead, the shape of the DEM we found in the bright points might imply that the transition region and the coronal plasma are rather heated independently.

Apart from the compact bipoles with mixed polarities, where magnetic loops are to be expected, the magnetic network can also comprise fields that are more unipolar. Such extended, unipolar areas host spicular emission in the chromosphere and transition region, with bushels of elongated structures that seemingly trace the magnetic field. The question of how the corona above such a magnetic foundation compares to the loops in bright points, and how it relates to the structures at lower temperatures, leads us to our next study (Ch. 6) about the diffuse coronal features in the quiet Sun.

6 Diffuse solar coronal features and their spicular footpoints*

Besides clear loop-like structures, there is also a component of the solar coronal emission that appears to be rather diffuse and featureless. This diffuse component, which often constitutes a majority of the coronal plasma, stands in contrast to the underlying, highly-structured chromosphere and transition region. The connection of the diffuse emission to the magnetic footpoints in the lower atmosphere is not well understood.

In this chapter, we study diffuse corona above the quiet Sun network. We combine spectral data from IRIS with cotemporal AIA and HMI observations, which allows us to connect the atmosphere – from the photosphere through the transition region into the corona. Our observations suggest that the diffuse emission forms at the base of a long-ranging magnetic loop. There are indications of spicular or other type of small-scale activity at the footpoints, which might be responsible for sustaining the diffuse emission for several hours.

6.1 Observations and data processing

6.1.1 Observational data

To span the solar atmosphere, we used observations from three instruments. We covered the photosphere with the magnetograms, the chromosphere and the transition region with the spectroscopic data in the UV domain, and the corona with the images in the EUV.

For a view of the transition region, we used observations acquired on 21 July 2014 (11:50 – 15:21 UT) with the IRIS spectrograph.¹ These data are in the form of a very large, dense raster, and the field of view is located near the disk center, in a quiet-Sun region (Fig. 6.1). The raster spans about 106'' in the east-west direction, with 400 steps (slit positions), each 0.35'' wide. The slit is about 171'' long, with the plate scale along the slit being

*This chapter is based on an article published in the journal *Astronomy & Astrophysics*, and all figures in this chapter are adopted from the paper:
N. Milanović, L. P. Chitta and H. Peter, *A&A* 673, A81, 2023.
DOI: 10.1051/0004-6361/202245544.

¹The IRIS data can be downloaded from <https://iris.lmsal.com/>.

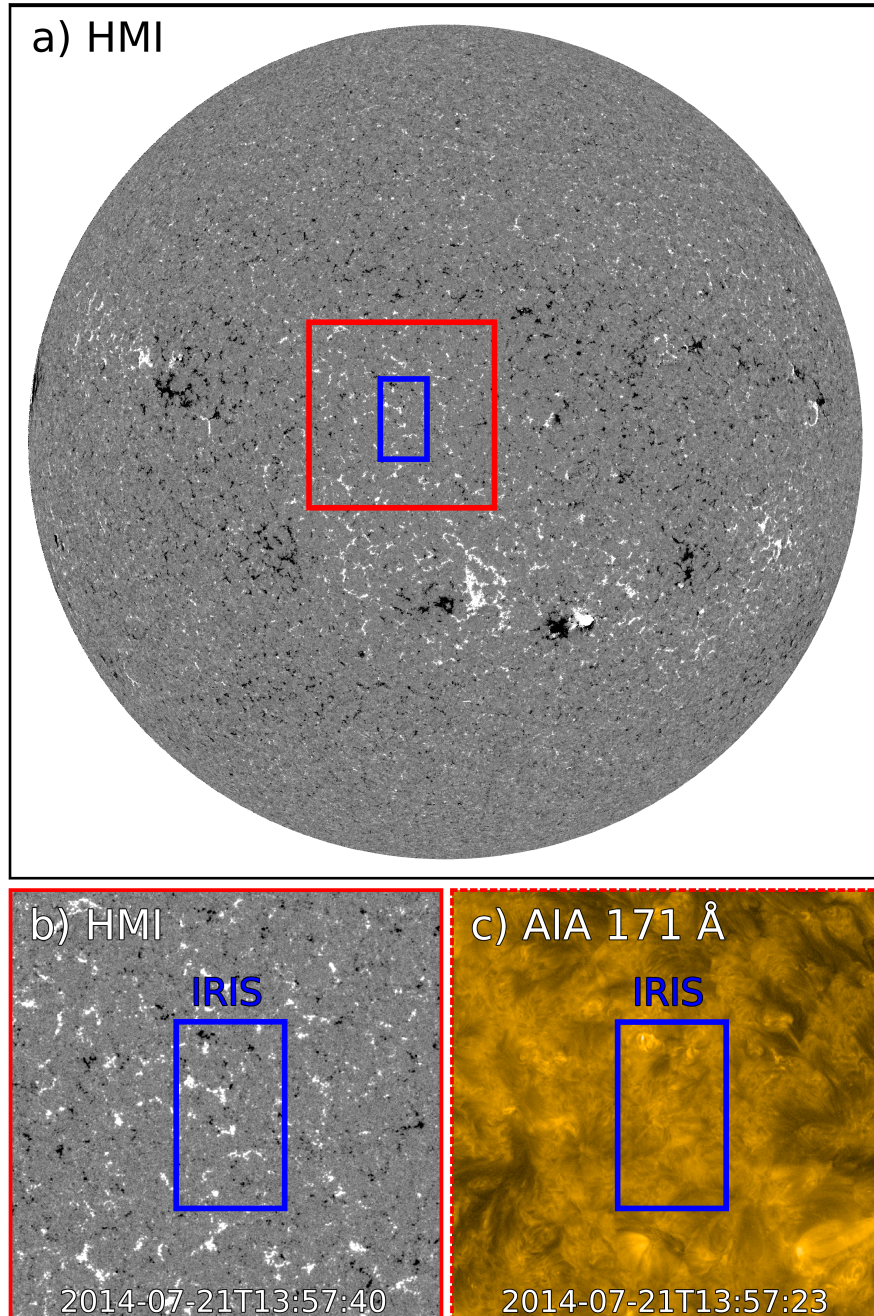


Figure 6.1: Observational context. In panel a we show a full-disk magnetogram acquired with HMI, at a time that corresponds to the midpoint of the IRIS raster. The field of view of IRIS is marked with the blue box, and a larger, surrounding area is marked with the red box. In panel b we show the contents of the red box as observed with HMI, and in (c) with the 171 Å channel of AIA, with the corresponding time stamps. The AIA image is plotted in logarithmic scaling. See Sect. 6.1.1 (Milanović et al. 2023).

Table 6.1: Lines and EUV bands

	Line / band ^a	$\log T$ [K] ^c	T [MK] ^c
	Si I continuum (low chromosphere)		
IRIS	Si IV 1393.76 Å	4.90	0.08
	O IV 1401.163 Å	5.18	0.15
	304 Å (He II)	4.92	0.08
	131 Å (Fe VIII) ^b	5.76	0.58
AIA	171 Å (Fe IX)	5.93	0.85
	193 Å (Fe XII)	6.18	1.5
	211 Å (Fe XIV)	6.27	1.9

Notes.

^a For the IRIS emission lines we list rest wavelengths from Sandlin et al. (1986), and for the AIA bands the dominant contributing ions from Lemen et al. (2012).

^b For the quiet-Sun observations, like in this study, the contribution from Fe XXI at around 10 MK in the 131 Å channel is not relevant.

^c For the IRIS spectral lines, we list the line formation temperature based on the MHD model by Peter et al. (2006), their Table 1. For the AIA channels, we list the peak temperature of the contribution function based on Peter et al. (2022), their Fig. 9.

0.17''/pixel. This observation contains several emission lines, with a good signal-to-noise ratio due to the exposure time of 30 s per slit position. The spectral scale of 25.6 m/pixel corresponds to about 5.5 km s⁻¹. In our work, we used emission lines of Si IV (1394 Å) and O IV (1401 Å), which form in the transition region, and the nearby Si I Lyman continuum at about 1395 Å (see Table 6.1; Sect. 4.1).

For the coronal emission, we used full-disk images in the 171 Å channel from AIA on board the SDO. These data are a time series spanning from one hour before to one hour after the IRIS raster. The images are taken with the temporal cadence of 12 s, and the plate scale is about 0.6''/pixel. To complement the images at 171 Å with observations that cover a wider range of temperatures, we used similar full-disk images in the 131 Å, 193 Å, 211 Å, and 304 Å channel (see Table 6.1). These images were acquired on the same day at about 13:57 UT, which corresponds to the time when the IRIS slit scanned over the region of interest of our study.

To follow the magnetic field in the photosphere, we used the full-disk

line-of-sight magnetograms from HMI on board the SDO.² The time series of the HMI data spans the same duration as the AIA 171 Å observations we used. These data have a temporal cadence of 45 s, and a plate scale of about 0.5"/pixel. We complemented these data with a daily updated synchronic frame from HMI for 21 July 2014, to learn about the configuration of the magnetic field on larger scales. A full description of the synchronic data, which provides the magnetic field over the whole solar surface, is available in Sun (2018).

6.1.2 Data processing

We analyzed the line profile of Si iv (1394 Å) and the properties of the nearby Si I Lyman continuum. We fit the measured Si iv line profile with a single Gaussian, by employing the Python package SciPy (Virtanen et al. 2020) and the `curve_fit` function. In Fig. 6.2a we show the total line intensity based on the fit parameters. Because IRIS did not follow solar rotation during the observation, the features on the Sun appear stretched along the direction of rastering. Since the observation was performed close to the disk center, the solar rotation is mostly along the east-west direction, which is the horizontal direction in the images. We therefore corrected for the effect of the rotation in all images that show the IRIS raster data, by simply adjusting the aspect ratio of the plot.

From the IRIS spectra around 1395 Å we obtained a map of the Si I Lyman continuum shown in Fig. 6.2d. This continuum intensity originates from the low chromosphere above the temperature minimum (e.g., Vernazza et al. 1981). We produced the image in Fig. 6.2d by summing the spectrum on the red side of the Si iv line, in the range between 150 km s^{-1} and 420 km s^{-1} that covers 49 spectral pixels. With the continuum intensity being rather faint, this approach of summation instead of a Gaussian fitting helped to reduce the noise. We further processed the image in order to detect small brightenings in the Si I continuum, which are related to the magnetic network. This processing included flattening of the visible global trends, and correcting for an odd-even pixel pattern in the rastering direction, which are prominent when working with low count rates in the continuum. The network brightenings, outlined with red contours in Fig. 6.2, should correspond to the chromospheric footpoints of the hotter transition-region and coronal structures. For that reason, the brightenings should show a very good correlation with the enhanced magnetic field concentrations in the network.

²The AIA and HMI data can be downloaded from <http://jsoc.stanford.edu/>.

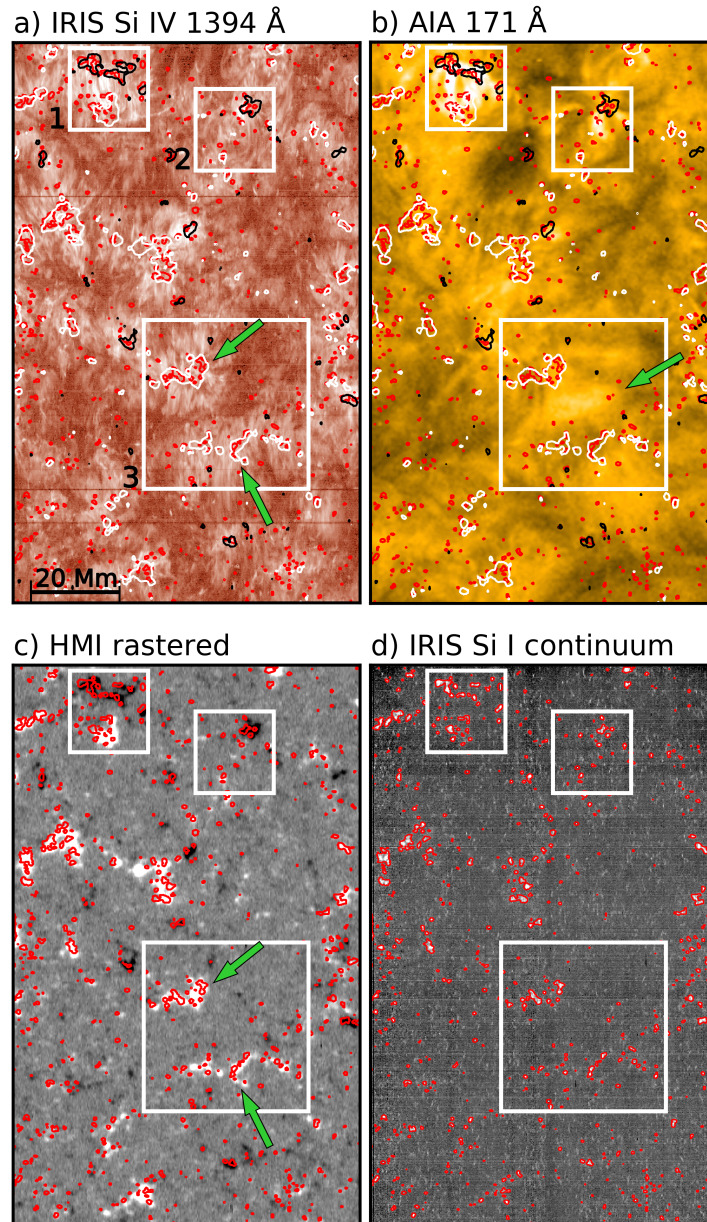


Figure 6.2: Overview of the used data. The four images show data matching the IRIS filed of view (blue box in Fig. 6.1a). These are (a) the total Si iv 1394 Å emission line intensity from the IRIS raster, (b) a snapshot from the 171 Å channel of AIA near the raster midpoint, (c) a pseudo-raster constructed with the line-of-sight magnetograms from HMI (Sect. 6.1.2), and (d) the Si I continuum around 1395 Å obtained from the IRIS raster. Panels a and b are shown in logarithmic scaling, and the overlaid black and white contours correspond to the magnetic field (panel c) of -30 G and $+30$ G, respectively. The red contours overlaid in all images mark the continuum brightenings (panel d). Different features, which are discussed in Sects. 6.1.2 and 6.2.1, are highlighted with the white squares and the green arrows (Milanović et al. 2023).

The preparation of the coronal images from AIA consisted of updating the instrument pointing information, rescaling the image plate scale to exactly $0.6''/\text{pixel}$, removing the instrument roll angle, and correcting the measured intensity for the degradation of the instrument. We performed these corrections by employing the routines available in the Python package `aiapy` (Barnes et al. 2020), which are based on the SolarSoft `aia_prep` procedure. To compare the AIA images with the IRIS spectra, we used the information about the field of view given in the data headers, and coaligned the AIA time series with the IRIS raster. This we did by using the routines from the Python package `reproject` (part of The Astropy Project; Astropy Collaboration et al. 2018; Astropy Collaboration et al. 2013). After we projected the AIA images onto the IRIS field of view, in order to track the evolution of the region of interest, we corrected the AIA images for solar rotation. This correction was performed separately for each AIA snapshot. As before, because of the proximity to the disk center, we assumed the rotation has an effect only along the east-west direction. We corrected for it by shifting the image along the horizontal axis for an integer number of IRIS pixels. In Fig. 6.2b we show one AIA snapshot in 171 \AA channel after it has been projected onto the IRIS field of view and corrected for the rotation.

As with the AIA data, we projected the HMI line-of-sight magnetograms and corrected for solar rotation. We used the resulting time series of magnetograms to construct a pseudo-raster, which we show in Fig. 6.2c. To do so, for each IRIS slit position, we cut a vertical stripe from a magnetogram which is the closest in time to that raster step. The resulting pseudo-raster magnetogram is nearly cotemporal with the IRIS raster. Since the underlying magnetic field changes during the roughly 3.5 hours of the IRIS raster, the pseudo-raster magnetogram is helpful in verifying the alignment between IRIS, HMI, and AIA. Good alignment between different data sets is evident in Fig. 6.2c, where the red contours, which correspond to the brightenings in the low chromosphere (IRIS), match the concentrations of the magnetic field in the photosphere (HMI).

6.1.3 Magnetic field extrapolation

We extrapolated the magnetic field using a potential field source surface (PFSS) model, where the magnetic field is calculated in spherical coordinates, under the assumption of no currents present in the volume. In this model, the field becomes radial at a certain height (radius) above the solar surface, and this height defines the so-called source surface. This extrapolation provided context for the large-scale structure of the field, and its

relation to our region of interest. We calculated the PFSS model using the Python package `pfsspy` (Stansby et al. 2020), where we specified boundary conditions for the magnetic field. For boundary conditions, we used a synchronic map of the photospheric magnetic field, which is a data product provided by HMI (`hmi.mrdailysynframe_polfil_720s`; Sect. 6.1.1).

The synchronic map contains values of the photospheric line-of-sight magnetic field, with spatial pixels equally spaced in longitude and sine of latitude. These data were remapped to a grid with pixel size of 0.5° at the solar equator (about 6 Mm), which is sufficient for our purpose. To set the grid in the radial direction, we used 100 points equally spaced in logarithmic scale between the photosphere and the source surface. The source surface, where the magnetic field becomes radial, was set to be at a radius of $2.5 R_\odot$. This resulted in the radial grid spacing near the solar surface of about 6.4 Mm, matching the horizontal spacing near the equator.

By using routines available in the `pfsspy` package, we traced magnetic field lines based on the PFSS model. We placed the starting points for the line-tracing ('seeds') near and within the IRIS field of view, at a height of $0.015 R_\odot$ (about 10 Mm) above the photosphere. We discuss the results of the extrapolation in Sect. 6.2.5.

6.2 Results

The target of our study is an unusual diffuse feature in the coronal emission, which we identified by combining the coronal images with the transition region spectra and the underlying magnetograms. To characterize this feature, we used temporal evolution of the coronal images, different wavelength bands in the corona and spectral lines in the transition region.

6.2.1 Unusual diffuse coronal emission pattern

As we discussed for the quiet Sun in Sect. 3.3, the emission from the transition-region Si iv ion (0.1 MK) predominantly originates from the bright lanes of the magnetic network. The emission is concentrated in the bushel-like patterns, where elongated features, possibly related to spicules (Sect. 3.3.1; e.g., Samanta et al. 2019), emerge and point outward from the magnetic field patches. Our data from IRIS also show this well-known property (Fig. 6.2a).

Short and cool loop-like features, that have often been observed to cross the network lanes (Sect. 3.3.2) are also visible in the Si iv image in Fig. 6.2a. These are particularly prominent at locations with stronger concentrations of the magnetic field, like in the two regions we highlighted with squares

1 and 2 at the top of the field of view. The transition region loops are intermixed with the coronal loops seen in 171 Å channel of AIA. These short loops span between bipolar magnetic footpoints, as it is expected in the coronal bright points (Sect. 3.3.3; e.g., Madjarska 2019).

As opposed to the short loops, in the square 3 in Fig. 6.2 we highlighted a region with quite a different emission pattern. This region shows two positive magnetic concentrations, marked with the green arrows in Fig. 6.2c. The emission in Si iv above the two positive polarities is reminiscent of the regions with spicular activity (green arrows in Fig. 6.2a; e.g., Samanta et al. 2019). At the coronal temperatures in the 171 Å images, there is a comparably bright diffuse-looking feature, located in between the two spicular regions in Si iv (green arrow in Fig. 6.2b). This unusual feature is the main target of our study (Milanović et al. 2023).

At first sight, the diffuse region, which extends over some 15×20 Mm, could originate at the apex of a closed magnetic connection. The closed connection would span between the two spicular footpoints, and the diffuse coronal emission would appear between the footpoints when observed from the top, due to the projection effects. On the other hand, the spicular footpoints originate from the magnetic patches of the same (positive) polarity. This makes the scenario of closed magnetic connection (a magnetic loop) unrealistic.

6.2.2 Temporal evolution of the diffuse region

The way in which the diffuse region evolves with time is also unusual. The region is visible in the images for at least five hours, and its evolution is unlike that of the common magnetically closed (coronal) loops. The brightness of the diffuse region evolves gradually, becoming either brighter or dimmer, but with no obvious presence of (spatial) substructure (Milanović et al. 2023).

To study the evolution, we investigated a time series of AIA 171 Å channel images (Fig. 6.3). In the time series, the diffuse region continuously appears smooth, which is the best visible in the movie of Fig. 6.3, but can also be seen from the different snapshots we show in Fig. 6.3b. The variability of the average intensity of the diffuse feature, shown in Fig. 6.3c, is generally not greater than 10% over a period of some five hours. These only gradual changes are emphasized with the space-time plot of an artificial slit we placed across the diffuse region (Fig. 6.3d). The slit position is marked with letters A and B in Fig. 6.3b. The space-time plot shows no ridges, or other signs of dynamic evolution.

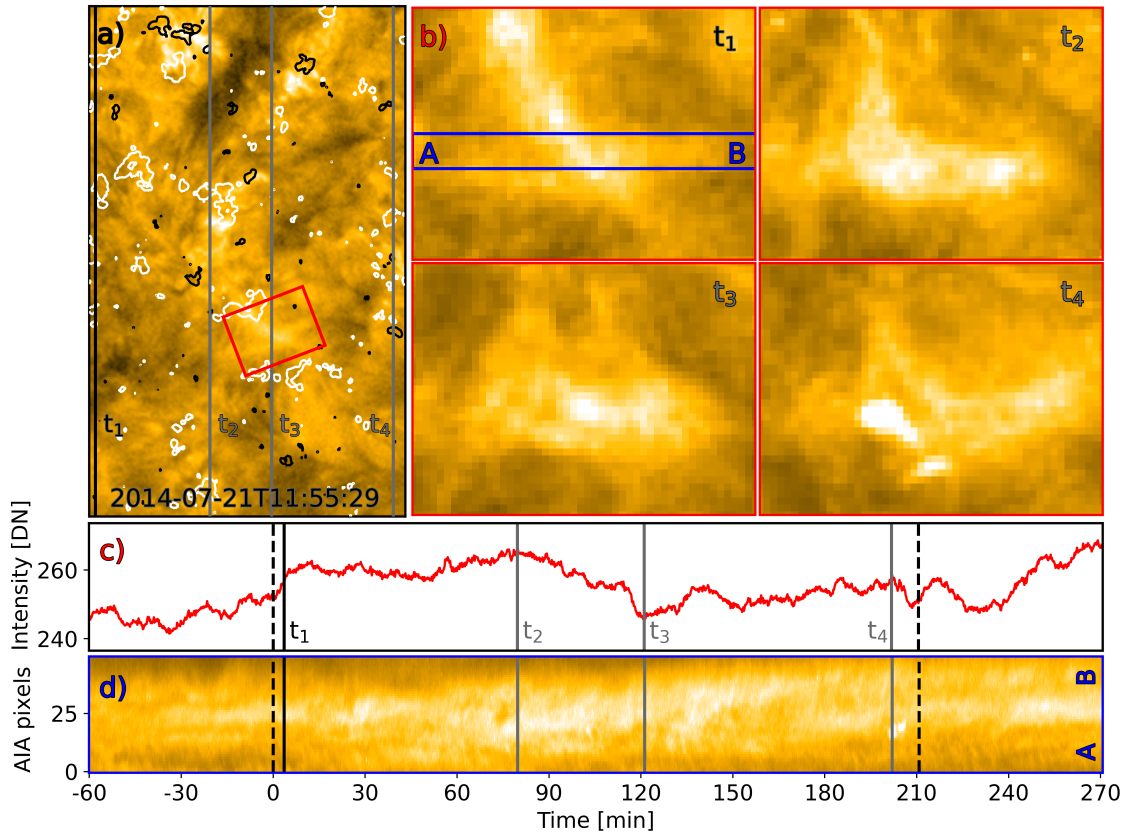


Figure 6.3: Temporal evolution of the diffuse region. In panel a we show an AIA 171 Å image at time t_1 , similar to Fig. 6.2b, with the overlaid black and white contours that mark the opposite magnetic polarities in the photosphere. We highlight the diffuse coronal region with the red rectangle. In panel b we display the contents of this rectangle, plotted in linear scaling, at times t_1 to t_4 . In panel c we show the light curve of the average emission in the red rectangle, where the variability over some five hours does not exceed about 10%. In panel d we display a space-time diagram of the emission averaged within an artificial slit, where the slit position is marked in panel b with letters A and B. The intensity is averaged across the slit, in the vertical direction between the two blue lines. The zero time on the axis in panels c and d corresponds to the beginning of the IRIS raster, which ends at 210 min. A movie of this figure is available with the online version of the paper by Milanović et al. (2023). See Sect. 6.2.2.

There are, however, a few exceptions, where the otherwise diffuse region at certain times shows bright, localized emission. For example, in the snapshot shown in Fig. 6.3b, which corresponds to time t_1 , there is a bright feature toward the top left corner. This feature appears to be related to the concentration of positive magnetic field right below (see the white contours in panel a). Similarly, there is a compact, bright feature in Fig. 6.3b at the time t_4 , located below the middle of the panel. This brightening is also prominent in the 304 Å channel of AIA. Because this channel images plasma at about 0.1 MK, this is an indication that the brightening originates from cooler, transition-region temperatures. The cooler brightening then appears in the 171 Å image, because this channel samples not only plasma at about 1 MK (Fe ix emission), but also at around 0.3 MK (O v emission; see Sect. 6.2.3). Although there are exceptions like these, over the observed five hours the diffuse region remains mainly diffuse (Fig. 6.3).

Finally, there is another diffuse-looking feature in the IRIS field of view, located below the square 1 in Fig. 6.2b. This feature also appears to have spicular bushels at the footpoints, which are of the same polarity (see Fig. 6.2a,c), similar to the region we studied. This second feature is, however, less isolated and closer to the coronal bright point marked with the square 1. Therefore, we did not focus on it here.

6.2.3 Temperature of diffuse region

To better estimate if the diffuse emission in the AIA 171 Å channel originates from coronal, or the transition-region plasma, we combined different channels of AIA with the emission lines from IRIS. In particular, we used the O iv line at 1401 Å to determine whether the diffuse emission forms at temperatures around 1 MK, or below 0.3 MK.

The diffuse region is the best observed in the AIA 171 Å channel (Fig. 6.4d–h). In the 131 Å channel, which samples cooler plasma (see Table 6.1), the region is recognizable, but less prominent compared to the 171 Å images. Similar is observed for the 193 Å and 211 Å channels, which sample hotter plasma.³ The situation is different for the 304 Å channel, which is the coolest of the AIA EUV channels and samples the transition region emission around 0.1 MK. The bright features there (Fig. 6.4d) are predominantly related to the magnetic footpoints, and avoid the location of the diffuse region.

The AIA images show the diffuse region predominantly in channels with

³Another diffuse structure is visible in the 193 Å and 211 Å channels. This possibly hotter structure is marked with the blue arrow in Fig. 6.4g–h. Our focus, however, is on the diffuse region in 171 Å images.

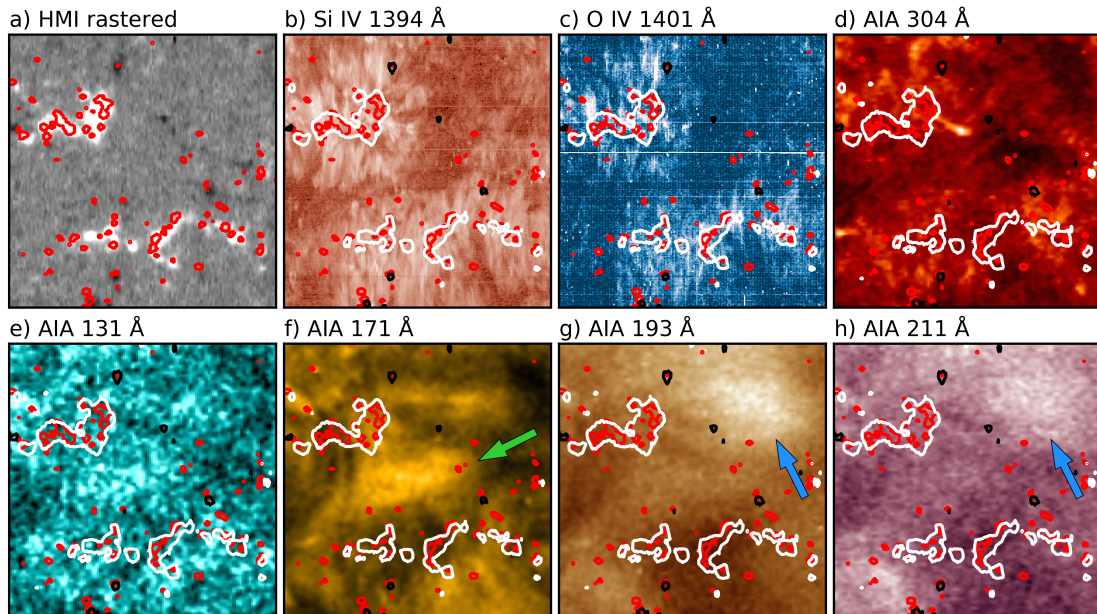


Figure 6.4: Diffuse region observed in various spectral bands. We show (a) the pseudo-raster of the line-of-sight magnetogram from HMI, as in Fig. 6.2c, (b) the total intensity of the Si iv 1394 Å line from IRIS, as in Fig. 6.2a, (c) the summed intensity in the spectral window of O iv 1401 Å emission line from IRIS, and (d)–(h) the images from different AIA channels, as indicated. Images in (b) and (c) are plotted in logarithmic scaling. The black and white contours outline the magnetic field of -30 G and $+30$ G, respectively, and the red contours mark the Si i continuum brightenings, as in Fig. 6.2. We highlighted the diffuse region we studied with the green arrow in panel f, and the neighboring region with hotter plasma with the blue arrows in panels g and h. See Sect. 6.2.3 (Milanović et al. 2023).

plasma above 0.8 MK, and not at 0.1 MK. This alone, however, is not sufficient to determine if the plasma in the diffuse region is of the coronal or the transition-region origin. The reason for this is the temperature response function of the 171 Å channel, where the diffuse region is the most prominent. The peak of the response function is at around 0.85 MK (see Table 6.1), due to the Fe ix emission lines. There is, however, a significant contribution from the transition region plasma at about 0.26 MK (e.g., Fig. 9 of Peter et al. 2022), which makes the temperature of the diffuse region more uncertain. This cooler contribution is mostly due to O v emission, which forms at about 0.27 MK (based on the magnetohydrodynamic model of Peter et al. 2006, see their Table 1).

To check whether it is likely that the diffuse emission is due to the contribution of O v, we used the O iv (1401 Å) emission line from IRIS, which forms at about 0.15 MK (see Table 6.1). In Fig. 6.4c we show the summed in-

tensity of 20 pixels in the spectral window of O IV, in a range between ± 55 km s⁻¹ around the rest line center. Both this image of O IV, and the Si IV image appear dark at the location of the diffuse region (Fig. 6.4b,c). Since there is no prominent O IV emission, we considered it more likely for the diffuse emission to originate from about 1 MK hot plasma, than from O V in the transition region (Milanović et al. 2023). This agrees with Martínez-Sykora et al. (2011), who concluded that the 171 Å channel predominantly shows emission at close to 1 MK.

6.2.4 Si IV line profiles at the spicular footpoints of the diffuse region

To investigate if the two neighboring spicular regions are related to the diffuse coronal emission, we analyzed the Si IV 1394 Å line profiles. We analyzed the line profile fits, and their asymmetries in particular, to see the presence of any up- and downflows in and out of the diffuse region.

We summarized the parameters of the Gaussian line fits for Si IV (1394 Å) in Fig. 6.5. In panels a–c we show the total line intensity, Doppler shift of the line center, and the nonthermal line width. In the field of view shown, the line profiles are predominantly redshifted (Fig. 6.5b), with the average value of the Doppler shift of 8.1 km s⁻¹ (Fig. 6.5e). This agrees with the earlier measurements for the quiet-Sun transition region (Peter & Judge 1999). Although most line profiles are single Gaussians, many pixels deviate from this, and show excursions in the red or in the blue line wing. We show examples of individual pixels with and without wing excursions in Fig. 6.5f–h.

We used the red-blue asymmetry (RBA) to study the spatial distribution of the excursions in the line wings. To do this, we first linearly interpolated the Si IV spectrum to a grid spacing of about 0.9 km s⁻¹, which roughly matches the error in the line shift from the Gaussian fit. We then calculated the RBA of the line at each spatial pixel, by integrating the spectrum in the red and in the blue wing, and then taking the difference of the two (similar to McIntosh & De Pontieu 2009). We set the range of the integration to $[+30, +50]$ km s⁻¹ in the red wing and $[-50, -30]$ km s⁻¹ in the blue wing, with respect to the line center from the Gaussian fit. These spectral ranges, which are marked for the sample spectra in Fig. 6.5f–h, cover the line profile between about one and two times the line width away from center. The selected ranges do not critically affect the resulting RBA map (Fig. 6.5d), but they show the line asymmetry most clearly.

The features in the RBA map are similar to those in the intensity map (cf. Fig. 6.5a,d). The blue excursions are predominantly seen in the magnetic

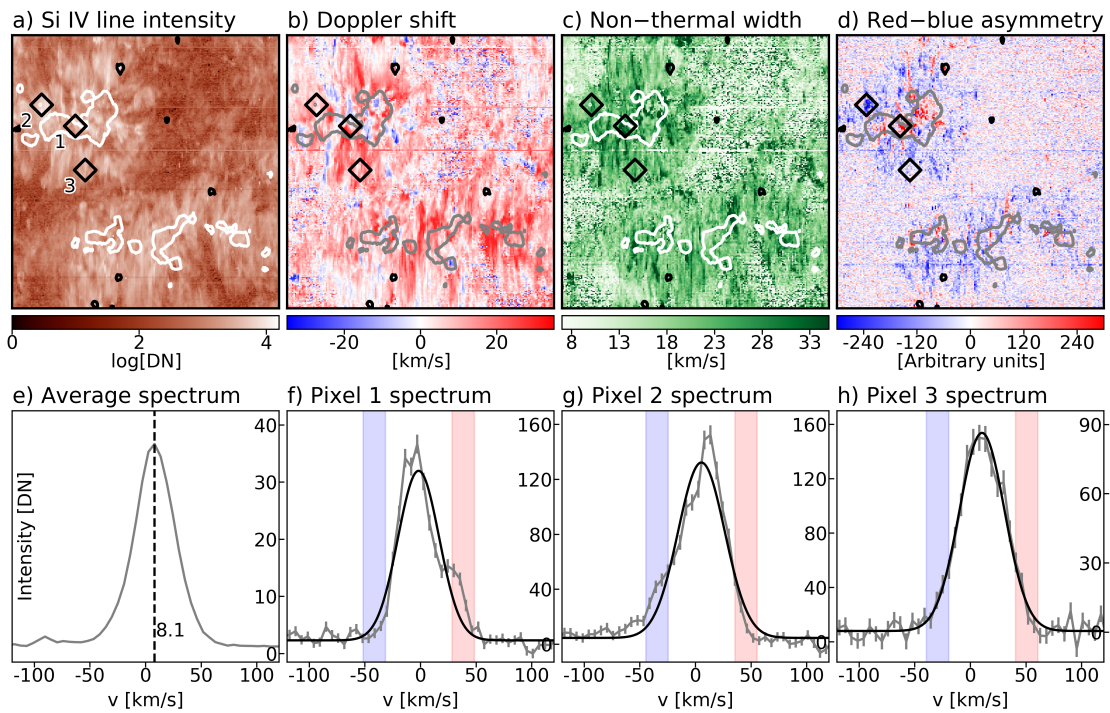


Figure 6.5: Summarized properties of Si iv (1394 \AA) profiles around the diffuse region. In the top panels we display (a) the total line intensity, (b) the Doppler shift of the line center, (c) the nonthermal line width, and (d) the red-blue asymmetry. The meaning of the contours is the same as in Fig. 6.2. In panel e we display the average line profile in the area shown in (a), with marked average Doppler shift of 8.1 km s^{-1} . In panels f–h we display line profiles of three individual spatial pixels which are marked with diamonds in the top images. Single Gaussian fits are shown in black, and measured spectra with errors in gray. Positive Doppler shift is toward red. The shaded areas in panels f–h mark the integration ranges we used for the red-blue asymmetry calculation. See Sect. 6.2.4 (Milanović et al. 2023).

network, and particularly at the transition between the network and the internetwork (Milanović et al. 2023). This is in agreement with the concept from De Pontieu et al. (2009), where spicular bushels, that might feed material into the corona, are expected to show emission in the blue wing. The red-wing excursions, which are mostly concentrated within the network elements, may indicate fast downflows of the cooling coronal material. The stronger RBA also appears to be correlated with the larger values of the non-thermal line width. This is reasonable, since the wing excursions can be interpreted as the presence of separate components in the line profile additional to the main one. At those locations, the single Gaussian fits applied to a multicomponent line result in the fitted profile typically wider than the individual components.

6.2.5 Magnetic connectivity of the diffuse region

Our study focuses on an area in the quiet Sun. The magnetic surroundings of the diffuse region, however, are more reminiscent of that of a coronal hole. In Fig. 6.1a, we show the distribution of the magnetic field at the surface. There, a larger area that surrounds our field of view, marked with the red box, hosts predominantly positive magnetic polarity.

Such extended, unipolar areas are common at the base of coronal holes, and result in an open field configuration on large scales. Based on the AIA EUV images, however, our field of view is not a part of a coronal hole. We therefore expect that the diffuse region is a part of a closed magnetic configuration, so that the field lines that originate there connect back to the surface. The prevailing positive flux in the area originated from the decay of active regions which were present there over multiple solar rotations. Because of this remnant magnetic flux from the decayed active regions, and the flux imbalance, we expect this area to be engaged in closed, but long-range magnetic connections.

To test for the presence of the long-range connections, we performed a PFSS magnetic field extrapolation (see Sect. 6.1.3). The magnetic field lines we traced from the extrapolation are shown in Fig. 6.6. There are closed field lines that originate from within the red box, with their footpoints about 400" (300 Mm) apart. These confirm that there are long-range connections between the diffuse coronal region and locations about 300 Mm away (Milanović et al. 2023).

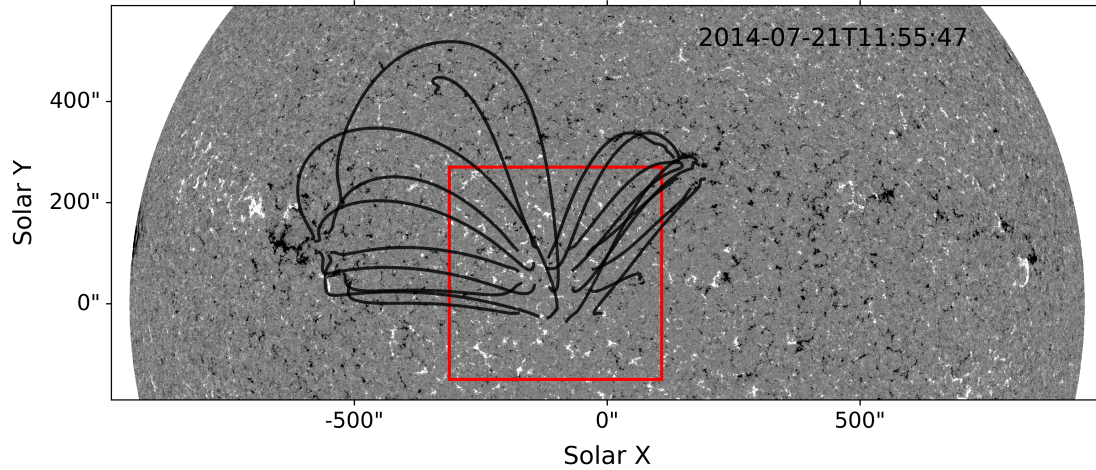


Figure 6.6: Large-scale magnetic configuration in the vicinity of the diffuse region. We show a line-of-sight magnetogram from HMI, where the surroundings of the diffuse region are denoted with the red box, same as in Fig. 6.1a. The magnetic field lines, traced from a PFSS extrapolation, show long-range connections starting from the location of the diffuse region (close to the center of the red box). See Sect. 6.2.5 (Milanović et al. 2023).

6.3 Discussion

6.3.1 Magnetic structure of diffuse coronal emission

An intriguing property of the observed diffuse coronal emission is its positioning between two patches of the positive magnetic field, which both host spicular bushels in the transition region. Based on these observations, we discuss how the diffuse region can fit into the surrounding magnetic configuration.

The footpoints of the diffuse region are likely to be located in the two underlying spicular bushels, that stem out of the positive magnetic patches (Fig. 6.4a). We illustrate the local magnetic configuration related to the diffuse region in the cartoon picture in Fig. 6.7. The magnetic field lines in the illustration originate from the two field concentrations of the same polarity, which are marked with N. The field lines form a canopy above and between the spicular bushels (orange). The apparently diffuse coronal emission comes from the plasma located within this canopy (yellow), which extends farther into the corona. The inspiration for this picture came from De Pontieu et al. (2009), and their scenario of spicules that feed mass into the coronal loops. While the magnetic configuration of the diffuse region might well be as in Fig. 6.7, the relation of spicules to the diffuse emission,

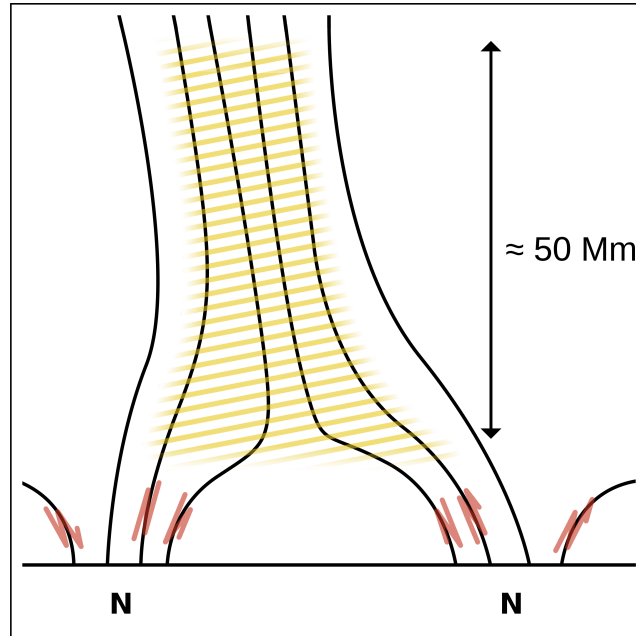


Figure 6.7: Magnetic field configuration within the diffuse region. With this illustration, we depict the vertical cross-section of the diffuse region, along the direction between the two positive magnetic footpoints (Fig. 6.4a) marked with N. The spicular emission at the footpoints is shown in orange, and the diffuse coronal emission in yellow. The magnetic field lines that originate from the footpoints form a canopy below the diffuse region. See Sect. 6.3.1 (Milanović et al. 2023).

and their role in loading hot mass into the corona, is still unclear (Milanović et al. 2023).

The diffuse region is present in the observations for many hours. Since this is much longer than the typical plasma cooling time in the corona (order of tens of minutes for 1 MK plasma; e.g., Aschwanden 2005), we expect the diffuse region to be in a near-equilibrium state and follow a barometric stratification. The plasma contained there, illustrated with yellow in Fig. 6.7, should then extend upward to at least one pressure scale height (about 50 Mm for 1 MK plasma). On the other hand, the observed diffuse region is a compact structure of a supergranular scale, near the disk center. This could be due to a projection effect, if the diffuse region is embedded in a magnetic field structure that is nearly vertical up to about 50 Mm, but observed from above (from the top in Fig. 6.7).

We reported in Sect. 6.2.5 about the possible long-ranging magnetic connection in the vicinity of the diffuse region. The region could then be located at the base of one of these long connections (loops). If for simplicity

we assume that this loop is semicircular and has footpoints about 300 Mm apart, the 50 Mm tall structure of the diffuse region at one of the footpoints would be nearly vertical. Observed from above, a 50 Mm long section of this loop would have a horizontal extent of only about 8.5 Mm, which is similar to the observed extent of the diffuse region (see Fig. 6.2b and the scale in panel a).

The above discussion suggests that the source of the diffuse emission is the plasma in the stem of a long-ranging loop (Milanović et al. 2023). If this is the case, the diffuse appearance might (at least partly) be a consequence of the averaging along the line of sight. This could be further investigated in future studies, by using observations of similarly diffuse emission from two vantage points close to quadrature, which can be arranged with AIA and EUVI on board Solar Orbiter.

6.3.2 Supply of hot gas to the diffuse corona above the quiet Sun

After we discussed its temperature and magnetic configuration, the remaining question is what processes play a role in the formation of the diffuse region. In this regard, our study is limited to speculations that need to be evaluated in the future, due to the limitations in the available data.

It is reasonable to assume that the footpoints hold information about the physical processes relevant for the diffuse region. At the footpoints, we found excess emission in the blue wing of the Si IV line from IRIS (see Figs. 6.4f and 6.5d). These blue excursions suggest presence of upflows, which might contribute hot plasma to the diffuse region. The upflows could be powered in the energetic events in the lower layers of the atmosphere, like in the type II spicules (Sect. 3.3.1), if they were really heated to coronal temperatures (De Pontieu et al. 2017a). They could also be powered by the heating events in the corona, where heat conduction from the corona downward causes chromospheric evaporation of plasma at the footpoints (Patsourakos & Klimchuk 2006).

On the other hand, the upflows we found at the footpoints need not really be related to the diffuse region. Their apparent relation in the images could simply be by chance. However, there are other examples of the activity at the footpoints sustaining the coronal phenomena for several hours. Here, we can make an analogy with the coronal holes. Although our diffuse region is located in the quiet Sun, it shows some similarities with the coronal holes, due to its predominantly unipolar magnetic environment. Coronal holes host hazy-looking features called plumes, which show very dynamical activ-

ity at their footpoints (e.g., Raouafi & Stenborg 2014). There, the cancellation of the minority polarity with the dominant flux is believed to drive different small-scale features, like jetlets and plume transient bright points (PTBPs). Similarly to plumes with their jetlets and PTBPs, our diffuse region might be supported for several hours by the upflows from the footpoints.

Finally, there is a possibility of plasma being supplied to the diffuse region from its other footpoint – the farther side of the long-ranging magnetic connection. This plasma would come in the form of downflows, which would need to be driven from the farther footpoint, possibly via a siphon flow. There have been many observations of the transition-region downflows above sunspots, where the footpoints of long coronal loops are located (Chen et al. 2022; Chitta et al. 2016). These downflows show in the transition region emission lines as redshifted components, often with shift indicating supersonic speeds. In our case, we investigated the average profiles of Si IV (1394 Å) and O IV (1401 Å), and could not identify any significant redshifts at the location of the diffuse region, at least not at these transition-region temperatures.

In this chapter, we studied diffuse coronal emission above the magnetic network in the quiet Sun. Our results suggest that the observed diffuse emission originated from the base of a long-ranging loop. Its featureless appearance is likely due to the averaging along the line of sight. The long-ranging loop stems out of a predominantly unipolar network in the quiet Sun. While these unipolar footpoints show signatures of spicular activity, the role of this activity in the formation of the diffuse emission remain unclear with the observations available in our study.

7 Conclusions

In this thesis, we discussed the upper atmosphere of the quiet Sun, with its footpoints in the supergranular magnetic network in the photosphere. Although it consists of magnetic features less prominent than those found in active regions, the quiet Sun makes a significant contribution to the solar magnetism, due to its ubiquity and fast replenishment. Continuous disturbance of the flux concentrations in the network provides magnetic heating, which energizes and sustains various dynamic features of the upper atmosphere, like spicules, network jets, or short loops. In the two studies that this thesis comprises, we aimed to understand how this structured and dynamic foundation related to the supergranular network gives rise to equally dynamic, small coronal loops in some places, but gradually-evolving, featureless coronal emission in others. We used data from different mission, including SDO, IRIS and Solar Orbiter, to probe the quiet atmosphere from its photospheric magnetic footpoints to the corona. Because different parts of the solar atmosphere are connected by the magnetic field, such data that cover different atmospheric layers are highly valuable when studying the origin of energy transport and heating in the upper atmosphere.

First we focused on the coronal bright points, which have been studied since the earliest X-ray and EUV images of the solar corona. While they were not spatially resolved in early observations, hence the name, we now know that they consist of a range of compact coronal loops (~ 20 Mm). With new instruments, like spectrograph SPICE on Solar Orbiter, which can simultaneously cover plasma from the low transition region to the corona, new light can be shed on the thermal properties of short loops in the bright points. We used SPICE data to analyze bright points in the quiet Sun, and identified 14 bright points in the transition-region network. All these features correspond to short loops in the coronal images from AIA on SDO, and have underlying bipolar fields at their footpoints in the photospheric magnetograms from HMI. Combining SPICE data with the coronal images from AIA allowed us to cover the bright points over a broad range of temperatures, and reconstruct their DEM.

All the bright points we analyzed show consistent trends of the DEM, when compared to the average quiet Sun. Namely, the slope of the DEM in the lower transition region ($\log T [\text{K}] < 5.2$) is negative and similar to the quiet Sun. In the upper transition region ($5.2 < \log T [\text{K}] < 6.0$), where the quiet-Sun DEM has a positive slope, the bright point DEM is flat or

shows a negative trend with temperature. Different features that we analyzed show clearly distinct magnetic evolution during a few hours prior to the DEM analysis. The similarities we found in their DEM might then imply that different magnetic processes, acting at the footpoints of these loops, result in similar properties of the heated plasma. More details about the heating mechanisms in the bright points can be inferred from the shape of the DEM. One approach we discussed is to interpret the slope of the DEM in the upper transition region in the context of nanoflare heating models and the frequency of the heating events. In this regard, our results imply that the bright points undergo larger, less frequent heating episodes compared to the average quiet Sun. Another possibility would be that, unlike in the nanoflare models, the heating mechanisms responsible for producing plasma in the transition region and in the corona are acting independently.

With the small magnetic flux concentrations that build the supergranular network, and form closed magnetic connections in the quiet Sun, one would expect that bright emission in the quiet corona typically resembles elongated, loop-like features. Interestingly, this is not always the case. While loops like those in coronal bright points are common, so are the comparably bright, but hazy regions with no clear substructure, that sometimes cover large areas the size of a supergranule. Such a diffuse-looking emission above the quiet-Sun network was the topic of our second study. We observed a diffuse region close to the disk center in the AIA images of about 1 MK plasma. The diffuse region was located above the internetwork, between two positive magnetic patches, making its magnetic connectivity puzzling. Unlike the dynamic loops in coronal bright points, the diffuse region evolved gradually over several hours, although the underlying transition region emission showed an abundance of small features, reminiscent of spicules.

The predominantly unipolar (positive) magnetic surroundings of the observed diffuse emission, together with the magnetic field extrapolations we performed, are both indicative of long-ranging magnetic connections starting from the vicinity of the diffuse region. Based on these findings, we suggest that the diffuse emission originated from a base of a long loop (~ 300 Mm) with highly-structured, spicular footpoints. If this is indeed the case, the compact appearance of the diffuse region near the disk center could be a consequence of a projection effect, when observing a nearly-vertical stem of the long loop from above. The inevitable line-of-sight integration over one pressure scale height would then contribute to the featureless appearance of the observed emission. Small-scale features at the footpoints of the diffuse emission, in the form of excursions in the blue wing of the transition-region Si IV line, suggest the presence of spicules or

other type of upflows. More extensive data, and particularly spectra that cover evolution of both transition-region and coronal plasma, are necessary to establish how this activity at the footpoints relates to the formation of the diffuse emission in the corona.

The studies we showed can be extended and deepened in several directions. While our one case-study of diffuse corona emission showed potential importance of long-ranging magnetic connections for the appearance of the quiet corona, future work should investigate how prevalent these long loops are in the diffuse corona. Another important question is where exactly the footpoints of the diffuse corona are located. More detailed magnetic field extrapolations can help investigate the importance of the rapidly-evolving internetwork flux for the formation of the featureless corona. There is also the question of thermal composition, where the diffuse corona can be compared to small loops and evaluated in terms of the shape of the DEM and frequency of heating events.

Dynamic structures in the quiet corona, like the small loops in coronal bright points, may live for several hours, and show variability at timescales down to minutes. In our study of coronal bright points, the AIA images showed highly dynamic features, both in coronal (e.g., at 171 Å), and in transition region emission (304 Å). With SPICE, however, we were not able to cover the evolution of the bright points. We had access to only one image of the transition region emission lines, acquired as a large raster map that takes about 45 minutes. In future work, we will focus on better capturing the evolution and dynamics of coronal bright points. Rasters that cover a smaller area on the Sun, but are successively repeated, are more appropriate for studying the evolution of small features, where the size of the field of view can be traded for the increased temporal cadence. Suitable data for this, for example, can be acquired with the instruments on board the Solar Orbiter.

An example of such a data set is shown in Fig. 7.1. These data were acquired on 12 October 2022, when Solar Orbiter was at a distance of about 0.29 astronomical units from the Sun. The EUV High Resolution Imager (EUI/HRI) covered an area in the quiet Sun at the disk center for more than two hours. This time series consists of images in 174 Å channel (Fe x emission at about 1 MK), taken with 10 s cadence in the first and the last 40 minutes, and with 3 s cadence for 45 minutes in between. During this period, the SPICE spectrograph made consecutive rasters with 6 steps, covering a narrow field of view of only about 5 Mm across, with a cadence of 72 s. A part of the EUI/HRI field of view was also covered with the High Resolution Telescope of the Polarimetric and Helioseismic Imager on the

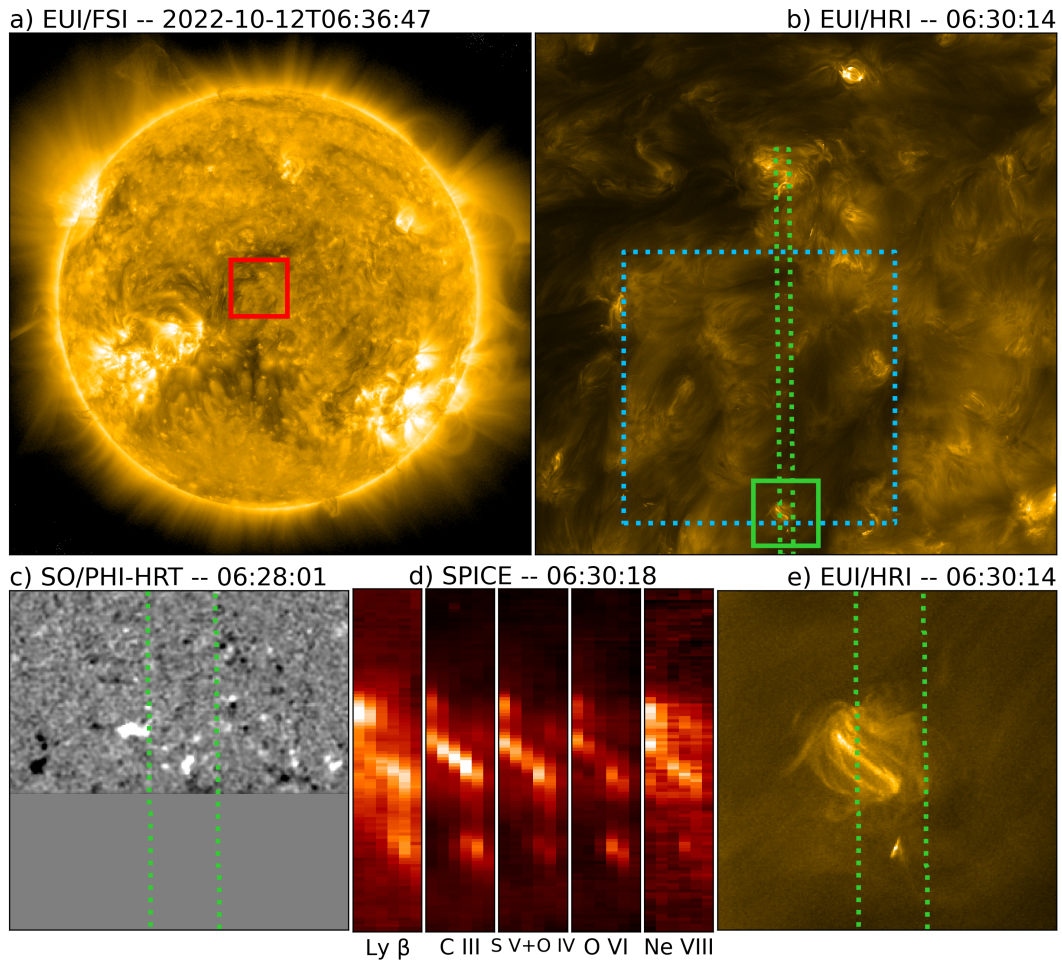


Figure 7.1: Coronal bright point study with Solar Orbiter. The image in the top left panel is acquired with the EUI Full Sun Imager (EUI/FSI), and the red box at the disk center marks the location of the EUI/HRI field of view. One snapshot from EUI/HRI is displayed in the top right panel, where the dotted green and blue boxes mark the location of the SPICE and SO/PHI-HRT field of view, respectively. The solid green box outlines a coronal bright point, which is enlarged in the bottom right panel. Nearly cotemporal snapshots from SO/PHI-HRT and SPICE at the location of the bright point are shown in the bottom left and middle panels, respectively.

Solar Orbiter mission (SO/PHI-HRT; Solanki et al. 2020), with a 5 minutes cadence.

In the bottom middle of the EUI/HRI field of view, there is a coronal bright point (solid green box in Fig. 7.1b), which due to the solar rotation gradually enters the SPICE field of view in the second half of the time series. In this unique observation, loops in the bright point are sampled with the spectrograph slit for about 45 minutes, covering simultaneously plasma from well below 0.1 MK into the corona at 1 MK. The EUI/HRI images show coronal loops that evolve on a timescale of minutes, at a great detail (Fig. 7.1e), with spatial resolution of about 200 km. The transition region emission seen with SPICE evolves equally fast, and the more modest spatial resolution of SPICE of about 1 Mm shows elongated features that resemble the ones seen with EUI/HRI (Fig. 7.1d). The loop footpoints (Fig. 7.1c), which are partially covered with the SO/PHI-HRT magnetogram (at a resolution of about 200 km, similar to EUI/HRI), show emergence of new magnetic flux and interactions of opposite polarities.

This rich data set allows for studying how thermal properties of small loops evolve with time, which was not possible in our previous study. With the detailed images from EUI/HRI, different parts of the loops can be targeted and compared, like the footpoints and the apex. The thermal response of plasma in the transition region and corona can be related to the evolution of the magnetic footpoints, observed in the similarly detailed magnetograms from SO/PHI-HRT. Furthermore, the SPICE slit also crosses an area of diffuse emission toward the top of the SO/PHI-HRT field of view. This might allow us to better characterize thermal properties of diffuse emission and its magnetic footpoints, and have a more direct comparison between the structured corona in loops and the seemingly-unstructured corona in the diffuse areas.

We used recent observations to study the quiet solar corona, that can exhibit both bright, distinct loops, and comparably bright, but diffuse emission. These two strikingly different components ultimately need to be reconciled, to answer how the quiet corona is heated. We made first steps in this regard, by looking at the thermal properties of the quiet corona, the activity at its magnetic footpoints, and the magnetic configuration on small and large scales. Future observations, with an emphasis on multi-instrument approach that spans the solar atmosphere from the surface to the corona, will advance our understanding of structuring and heating of the quiet solar corona.

Bibliography

- Alfvén, H. (1941). On the solar corona. *Arkiv for Matematik, Astronomi och Fysik*, 27A, 1–23.
- Andretta, V., & Jones, H. P. (1997). On the Role of the Solar Corona and Transition Region in the Excitation of the Spectrum of Neutral Helium. *Astrophys. J.*, 489(1), 375–394. <https://doi.org/10.1086/304760>
- Antiochos, S. K., & Noci, G. (1986). The Structure of the Static Corona and Transition Region. *Astrophys. J.*, 301, 440. <https://doi.org/10.1086/163912>
- Aschwanden, M. J. (2005). *Physics of the Solar Corona. An Introduction with Problems and Solutions (2nd edition)*.
- Aschwanden, M. J., & Nightingale, R. W. (2005). Elementary Loop Structures in the Solar Corona Analyzed from TRACE Triple-Filter Images. *Astrophys. J.*, 633(1), 499–517. <https://doi.org/10.1086/452630>
- Astropy Collaboration, Price-Whelan, A. M., Sipőcz, B. M., Günther, H. M., Lim, P. L., Crawford, S. M., Conseil, S., Shupe, D. L., Craig, M. W., Dencheva, N., Ginsburg, A., VanderPlas, J. T., Bradley, L. D., Pérez-Suárez, D., de Val-Borro, M., Aldcroft, T. L., Cruz, K. L., Robitaille, T. P., Tollerud, E. J., ... Astropy Contributors. (2018). The Astropy Project: Building an Open-science Project and Status of the v2.0 Core Package. *Astron. J.*, 156(3), Article 123, 123. <https://doi.org/10.3847/1538-3881/aabc4f>
- Astropy Collaboration, Robitaille, T. P., Tollerud, E. J., Greenfield, P., Droettboom, M., Bray, E., Aldcroft, T., Davis, M., Ginsburg, A., Price-Whelan, A. M., Kerzendorf, W. E., Conley, A., Crighton, N., Barbary, K., Muna, D., Ferguson, H., Grollier, F., Parikh, M. M., Nair, P. H., ... Streicher, O. (2013). Astropy: A community Python package for astronomy. *Astron. Astrophys.*, 558, Article A33, A33. <https://doi.org/10.1051/0004-6361/201322068>
- Athay, R. G. (1982). Responses of transition region models to magnetic field geometry and downflow velocities. *Astrophys. J.*, 263, 982–986. <https://doi.org/10.1086/160565>
- Barnes, W. T., Cheung, M. C. M., Bobra, M. G., Boerner, P. F., Chintzoglou, G., Leonard, D., Mumford, S. J., Padmanabhan, N., Shih, A. Y., Shirman, N., Stansby, D., & Wright, P. J. (2020). Aiapy: A python package for analyzing solar euv image data from aia. *Journal of Open Source Software*, 5(55), 2801. <https://doi.org/10.21105/joss.02801>

- Beckers, J. M. (1968). Solar Spicules (Invited Review Paper). *Solar Phys.*, 3(3), 367–433. <https://doi.org/10.1007/BF00171614>
- Bose, S., Nóbrega-Siverio, D., De Pontieu, B., & Rouppe van der Voort, L. (2023). The Chromosphere Underneath a Coronal Bright Point. *Astrophys. J.*, 944(2), Article 171, 171. <https://doi.org/10.3847/1538-4357/acb544>
- Bray, R. J., Cram, L. E., Durrant, C., & Loughhead, R. E. (1991). *Plasma loops in the solar corona*. Cambridge University Press. <https://doi.org/10.1017/CBO9780511600111>
- Breu, C., Peter, H., Cameron, R., Solanki, S. K., Przybylski, D., Rempel, M., & Chitta, L. P. (2022). A solar coronal loop in a box: Energy generation and heating. *Astron. Astrophys.*, 658, Article A45, A45. <https://doi.org/10.1051/0004-6361/202141451>
- Brooks, D. H., Warren, H. P., & Ugarte-Urra, I. (2012). Solar Coronal Loops Resolved by Hinode and the Solar Dynamics Observatory. *Astrophys. J. Lett.*, 755(2), Article L33, L33. <https://doi.org/10.1088/2041-8205/755/2/L33>
- Cargill, P. J. (2014). Active region emission measure distributions and implications for nanoflare heating. *The Astrophysical Journal*, 784(1), 49. <https://doi.org/10.1088/0004-637X/784/1/49>
- Cargill, P. J. (1994). Some Implications of the Nanoflare Concept. *Astrophys. J.*, 422, 381. <https://doi.org/10.1086/173733>
- Carlsson, M., De Pontieu, B., & Hansteen, V. H. (2019). New View of the Solar Chromosphere. *Ann. Rev. Astron. Astrophys.*, 57, 189–226. <https://doi.org/10.1146/annurev-astro-081817-052044>
- Chen, H., Tian, H., Li, L., Peter, H., Chitta, L. P., & Hou, Z. (2022). Coronal condensation as the source of transition-region supersonic downflows above a sunspot. *Astron. Astrophys.*, 659, Article A107, A107. <https://doi.org/10.1051/0004-6361/202142093>
- Chen, Y., Tian, H., Huang, Z., Peter, H., & Samanta, T. (2019). Investigating the Transition Region Explosive Events and Their Relationship to Network Jets. *Astrophys. J.*, 873(1), Article 79, 79. <https://doi.org/10.3847/1538-4357/ab0417>
- Cheung, M. C. M., Boerner, P., Schrijver, C. J., Testa, P., Chen, F., Peter, H., & Malanushenko, A. (2015). Thermal Diagnostics with the Atmospheric Imaging Assembly on board the Solar Dynamics Observatory: A Validated Method for Differential Emission Measure Inversions. *Astrophys. J.*, 807(2), Article 143, 143. <https://doi.org/10.1088/0004-637X/807/2/143>

- Chitta, L. P., Kariyappa, R., van Ballegooijen, A. A., DeLuca, E. E., Hasan, S. S., & Hanslmeier, A. (2013). Observations and Modeling of the Emerging Extreme-ultraviolet Loops in the Quiet Sun as Seen with the Solar Dynamics Observatory. *Astrophys. J.*, *768*(1), Article 32, 32. <https://doi.org/10.1088/0004-637X/768/1/32>
- Chitta, L. P., Peter, H., Solanki, S. K., Barthol, P., Gandorfer, A., Gizon, L., Hirzberger, J., Riethmüller, T. L., van Noort, M., Blanco Rodríguez, J., Del Toro Iniesta, J. C., Orozco Suárez, D., Schmidt, W., Martínez Pillet, V., & Knölker, M. (2017). Solar Coronal Loops Associated with Small-scale Mixed Polarity Surface Magnetic Fields. *Astrophys. J. Suppl.*, *229*(1), Article 4, 4. <https://doi.org/10.3847/1538-4365/229/1/4>
- Chitta, L. P., Peter, H., & Young, P. R. (2016). A closer look at a coronal loop rooted in a sunspot umbra. *Astron. Astrophys.*, *587*, Article A20, A20. <https://doi.org/10.1051/0004-6361/201527340>
- Cranmer, S. R., & van Ballegooijen, A. A. (2005). On the Generation, Propagation, and Reflection of Alfvén Waves from the Solar Photosphere to the Distant Heliosphere. *Astrophys. J. Suppl.*, *156*(2), 265–293. <https://doi.org/10.1086/426507>
- Cranmer, S. R., & Winebarger, A. R. (2019). The Properties of the Solar Corona and Its Connection to the Solar Wind. *Ann. Rev. Astron. Astrophys.*, *57*, 157–187. <https://doi.org/10.1146/annurev-astro-091918-104416>
- Dammasch, I. E., Curdt, W., Dwivedi, B. N., & Parenti, S. (2008). The redshifted footpoints of coronal loops. *Annales Geophysicae*, *26*(10), 2955–2959. <https://doi.org/10.5194/angeo-26-2955-2008>
- De Pontieu, B., De Moortel, I., Martínez-Sykora, J., & McIntosh, S. W. (2017a). Observations and Numerical Models of Solar Coronal Heating Associated with Spicules. *Astrophys. J. Lett.*, *845*(2), Article L18, L18. <https://doi.org/10.3847/2041-8213/aa7fb4>
- De Pontieu, B., McIntosh, S., Hansteen, V. H., Carlsson, M., Schrijver, C. J., Tarbell, T. D., Title, A. M., Shine, R. A., Suematsu, Y., Tsuneta, S., Katsukawa, Y., Ichimoto, K., Shimizu, T., & Nagata, S. (2007a). A Tale of Two Spicules: The Impact of Spicules on the Magnetic Chromosphere. *Pub. Astron. Soc. Japan*, *59*, S655. <https://doi.org/10.1093/pasj/59.sp3.S655>
- De Pontieu, B., Martínez-Sykora, J., & Chintzoglou, G. (2017b). What Causes the High Apparent Speeds in Chromospheric and Transition Region Spicules on the Sun? *Astrophys. J. Lett.*, *849*(1), Article L7, L7. <https://doi.org/10.3847/2041-8213/aa9272>
- De Pontieu, B., McIntosh, S. W., Carlsson, M., Hansteen, V. H., Tarbell, T. D., Schrijver, C. J., Title, A. M., Shine, R. A., Tsuneta, S., Katsukawa, Y.,

- Ichimoto, K., Suematsu, Y., Shimizu, T., & Nagata, S. (2007b). Chromospheric Alfvénic Waves Strong Enough to Power the Solar Wind. *Science*, 318(5856), 1574. <https://doi.org/10.1126/science.1151747>
- De Pontieu, B., Title, A. M., Lemen, J. R., Kushner, G. D., Akin, D. J., Allard, B., Berger, T., Boerner, P., Cheung, M., Chou, C., Drake, J. F., Duncan, D. W., Freeland, S., Heyman, G. F., Hoffman, C., Hurlburt, N. E., Lindgren, R. W., Mathur, D., Rehse, R., ... Waltham, N. (2014). The Interface Region Imaging Spectrograph (IRIS). *Solar Phys.*, 289(7), 2733–2779. <https://doi.org/10.1007/s11207-014-0485-y>
- De Pontieu, B., Erdélyi, R., & James, S. P. (2004). Solar chromospheric spicules from the leakage of photospheric oscillations and flows. *Nature*, 430(6999), 536–539. <https://doi.org/10.1038/nature02749>
- De Pontieu, B., McIntosh, S. W., Hansteen, V. H., & Schrijver, C. J. (2009). Observing the Roots of Solar Coronal Heating—in the Chromosphere. *Astrophys. J. Lett.*, 701(1), L1–L6. <https://doi.org/10.1088/0004-637X/701/1/L1>
- Del Zanna, G., Dere, K. P., Young, P. R., & Landi, E. (2021). CHIANTI—An Atomic Database for Emission Lines. XVI. Version 10, Further Extensions. *Astrophys. J.*, 909(1), Article 38, 38. <https://doi.org/10.3847/1538-4357/abd8ce>
- Del Zanna, G., & Mason, H. E. (2003). Solar active regions: SOHO/CDS and TRACE observations of quiescent coronal loops. *Astron. Astrophys.*, 406, 1089–1103. <https://doi.org/10.1051/0004-6361:20030791>
- Del Zanna, G., & Mason, H. E. (2018). Solar UV and X-ray spectral diagnostics. *Living Reviews in Solar Physics*, 15(1), Article 5, 5. <https://doi.org/10.1007/s41116-018-0015-3>
- Dere, K. P. (1994). Explosive events, magnetic reconnection, and coronal heating. *Advances in Space Research*, 14(4), 13–22. [https://doi.org/10.1016/0273-1177\(94\)90154-6](https://doi.org/10.1016/0273-1177(94)90154-6)
- Dere, K. P., Landi, E., Mason, H. E., Monsignori Fossi, B. C., & Young, P. R. (1997). CHIANTI - an atomic database for emission lines. *Astron. Astrophys. Suppl.*, 125, 149–173. <https://doi.org/10.1051/aas:1997368>
- Doschek, G. A., Landi, E., Warren, H. P., & Harra, L. K. (2010). Bright Points and Jets in Polar Coronal Holes Observed by the Extreme-Ultraviolet Imaging Spectrometer on Hinode. *Astrophys. J.*, 710(2), 1806–1824. <https://doi.org/10.1088/0004-637X/710/2/1806>
- Dowdy, J., J. F., Rabin, D., & Moore, R. L. (1986). On the Magnetic Structure of the Quiet Transition Region. *Solar Phys.*, 105(1), 35–45. <https://doi.org/10.1007/BF00156374>

- Edlén, B. (1943). Die Deutung der Emissionslinien im Spektrum der Sonnenkorona. Mit 6 Abbildungen. *Z. Astrophys.*, 22, 30.
- Feldman, U. (1983). On the unresolved fine structures of the solar atmosphere in the 30,000-200,000 K temperature region. *Astrophys. J.*, 275, 367–373. <https://doi.org/10.1086/161539>
- Feldman, U., Widing, K. G., & Warren, H. P. (1999). Morphology of the Quiet Solar Upper Atmosphere in the $4 \times 10^4 < T_e < 1.4 \times 10^6$ K Temperature Regime. *Astrophys. J.*, 522(2), 1133–1147. <https://doi.org/10.1086/307682>
- Fludra, A., Caldwell, M., Giunta, A., Grundy, T., Guest, S., Leeks, S., Sidher, S., Auchère, F., Carlsson, M., Hassler, D., Peter, H., Aznar Cuadrado, R., Buchlin, É., Caminade, S., DeForest, C., Fredvik, T., Haberreiter, M., Harra, L., Janvier, M., ... Chitta, L. P. (2021). First observations from the spice euv spectrometer on solar orbiter. *A&A*, 656, A38. <https://doi.org/10.1051/0004-6361/202141221>
- Gabriel, A. H. (1976). A Magnetic Model of the Solar Transition Region. *Philos. Trans. Royal Soc. A*, 281(1304), 339–352. <https://doi.org/10.1098/rsta.1976.0031>
- Golub, L., DeLuca, E., Austin, G., Bookbinder, J., Caldwell, D., Cheimets, P., Cirtain, J., Cosmo, M., Reid, P., Sette, A., Weber, M., Sakao, T., Kano, R., Shibasaki, K., Hara, H., Tsuneta, S., Kumagai, K., Tamura, T., Shimojo, M., ... Varisco, S. (2007). The X-Ray Telescope (XRT) for the Hinode Mission. *Solar Phys.*, 243(1), 63–86. <https://doi.org/10.1007/s11207-007-0182-1>
- Golub, L., Krieger, A. S., Harvey, J. W., & Vaiana, G. S. (1977). Magnetic properties of X-ray bright points. *Solar Phys.*, 53(1), 111–121. <https://doi.org/10.1007/BF02260212>
- Golub, L., Krieger, A. S., Silk, J. K., Timothy, A. F., & Vaiana, G. S. (1974). Solar X-Ray Bright Points. *Astrophys. J. Lett.*, 189, L93. <https://doi.org/10.1086/181472>
- Gorman, J., Chitta, L. P., & Peter, H. (2022). Spectroscopic observation of a transition region network jet. *Astron. Astrophys.*, 660, Article A116, A116. <https://doi.org/10.1051/0004-6361/202142995>
- Gorman, J., Chitta, L. P., Peter, H., Berghmans, D., Auchère, F., Aznar Cuadrado, R., Teriaca, L., Solanki, S. K., Verbeeck, C., Kraaikamp, E., Stegen, K., & Gissot, S. (2023). Beyond small-scale transients: A closer look at the diffuse quiet solar corona. *Astron. Astrophys.*, 678, Article A188, A188. <https://doi.org/10.1051/0004-6361/202345892>
- Griffiths, N. W., Fisher, G. H., Woods, D. T., Acton, L. W., & Siegmund, O. H. W. (2000). Simultaneous SOHO and Yohkoh Observations of a Small So-

- lar Active Region. *Astrophys. J.*, 537(1), 481–494. <https://doi.org/10.1086/309005>
- Griffiths, N. W., Fisher, G. H., Woods, D. T., & Siegmund, O. H. W. (1999). SUMER Observations of the Quiet-Sun Transition Region. *Astrophys. J.*, 512(2), 992–1005. <https://doi.org/10.1086/306794>
- Grotian, W. (1939). Zur Frage der Deutung der Linien im Spektrum der Sonnenkorona. *Naturwissenschaften*, 27(13), 214–214. <https://doi.org/10.1007/BF01488890>
- Habbal, S. R., & Withbroe, G. L. (1981). Spatial and Temporal Variations of EUV Coronal Bright Points. *Solar Phys.*, 69(1), 77–97. <https://doi.org/10.1007/BF00151257>
- Habbal, S. R., Dowdy, J., James F., & Withbroe, G. L. (1990). A Comparison between Bright Points in a Coronal Hole and a Quiet-Sun Region. *Astrophys. J.*, 352, 333. <https://doi.org/10.1086/168540>
- Hackenberg, P., Marsch, E., & Mann, G. (2000). On the origin of the fast solar wind in polar coronal funnels. *Astron. Astrophys.*, 360, 1139–1147.
- Hansteen, V., De Pontieu, B., Carlsson, M., Lemen, J., Title, A., Boerner, P., Hurlburt, N., Tarbell, T. D., Wuelsel, J. P., Pereira, T. M. D., De Luca, E. E., Golub, L., McKillop, S., Reeves, K., Saar, S., Testa, P., Tian, H., Kankelborg, C., Jaeggli, S., ... Martí-Nez-Sykora, J. (2014). The unresolved fine structure resolved: IRIS observations of the solar transition region. *Science*, 346(6207), Article 1255757, 1255757. <https://doi.org/10.1126/science.1255757>
- Hansteen, V. H., De Pontieu, B., Rouppe van der Voort, L., van Noort, M., & Carlsson, M. (2006). Dynamic Fibrils Are Driven by Magnetoacoustic Shocks. *Astrophys. J. Lett.*, 647(1), L73–L76. <https://doi.org/10.1086/507452>
- Hansteen, V. H., & Leer, E. (1995). Coronal heating, densities, and temperatures and solar wind acceleration. *J. Geophys. Res.*, 100(A11), 21577–21594. <https://doi.org/10.1029/95JA02300>
- Huang, Z., Teriaca, L., Aznar Cuadrado, R., Chitta, L. P., Mandal, S., Peter, H., Schühle, U., Solanki, S. K., Auchère, F., Berghmans, D., Buchlin, É., Carlsson, M., Fludra, A., Fredvik, T., Giunta, A., Grundy, T., Hassler, D., Parenti, S., & Plaschke, F. (2023). Imaging and spectroscopic observations of extreme-ultraviolet brightenings using EUI and SPICE on board Solar Orbiter. *Astron. Astrophys.*, 673, Article A82, A82. <https://doi.org/10.1051/0004-6361/202345988>
- Innes, D. E., Inhester, B., Axford, W. I., & Wilhelm, K. (1997). Bi-directional plasma jets produced by magnetic reconnection on the Sun. *Nature*, 386(6627), 811–813. <https://doi.org/10.1038/386811a0>

- Judge, P., Carlsson, M., & Wilhelm, K. (1997). SUMER Observations of the Quiet Solar Atmosphere: The Network Chromosphere and Lower Transition Region. *Astrophys. J. Lett.*, 490(2), L195–L198. <https://doi.org/10.1086/311037>
- Judge, P., & Centeno, R. (2008). On the Magnetic Structure of the Solar Transition Region. *Astrophys. J.*, 687(2), 1388–1397. <https://doi.org/10.1086/590104>
- Kayshap, P., & Dwivedi, B. N. (2017). Diagnostics of Coronal Bright Points using IRIS, AIA, and HMI Observations. *Solar Phys.*, 292(8), Article 108, 108. <https://doi.org/10.1007/s11207-017-1132-1>
- Klimchuk, J. A. (2012). The role of type II spicules in the upper solar atmosphere. *Journal of Geophysical Research (Space Physics)*, 117(A12), Article A12102, A12102. <https://doi.org/10.1029/2012JA018170>
- Klimchuk, J. A. (2006). On Solving the Coronal Heating Problem. *Solar Phys.*, 234(1), 41–77. <https://doi.org/10.1007/s11207-006-0055-z>
- Klimchuk, J. A. (2015). Key aspects of coronal heating. *Philosophical Transactions of the Royal Society of London Series A*, 373(2042), 20140256–20140256. <https://doi.org/10.1098/rsta.2014.0256>
- Klimchuk, J. A., Lemen, J. R., Feldman, U., Tsuneta, S., & Uchida, Y. (1992). Thickness Variations along Coronal Loops Observed by the Soft X-Ray Telescope on YOHKOH. *Pub. Astron. Soc. Japan*, 44, L181–L185.
- Lagg, A., Solanki, S. K., Riethmüller, T. L., Martínez Pillet, V., Schüssler, M., Hirzberger, J., Feller, A., Borrero, J. M., Schmidt, W., del Toro Iniesta, J. C., Bonet, J. A., Barthol, P., Berkefeld, T., Domingo, V., Gandorfer, A., Knölker, M., & Title, A. M. (2010). Fully Resolved Quiet-Sun Magnetic flux Tube Observed with the SUNRISE/IMAX Instrument. *Astrophys. J. Lett.*, 723(2), L164–L168. <https://doi.org/10.1088/2041-8205/723/2/L164>
- Landi, E., Mason, H. E., Lemaire, P., & Landini, M. (2000). SUMER observations of transition region fine structures. *Astron. Astrophys.*, 357, 743–756.
- Lemen, J. R., Title, A. M., Akin, D. J., Boerner, P. F., Chou, C., Drake, J. F., Duncan, D. W., Edwards, C. G., Friedlaender, F. M., Heyman, G. F., Hurlburt, N. E., Katz, N. L., Kushner, G. D., Levay, M., Lindgren, R. W., Mathur, D. P., McFeaters, E. L., Mitchell, S., Rehse, R. A., ... Waltham, N. (2012). The Atmospheric Imaging Assembly (AIA) on the Solar Dynamics Observatory (SDO). *Solar Phys.*, 275(1-2), 17–40. <https://doi.org/10.1007/s11207-011-9776-8>
- Madjarska, M. S. (2019). Coronal bright points. *Living Reviews in Solar Physics*, 16(1), Article 2, 2. <https://doi.org/10.1007/s41116-019-0018-8>

- Madjarska, M. S., Chae, J., Moreno-Insertis, F., Hou, Z., Nóbrega-Siverio, D., Kwak, H., Galsgaard, K., & Cho, K. (2021). The chromospheric component of coronal bright points. Coronal and chromospheric responses to magnetic-flux emergence. *Astron. Astrophys.*, *646*, Article A107, A107. <https://doi.org/10.1051/0004-6361/202039329>
- Malanushenko, A., & Schrijver, C. J. (2013). On the Anisotropy in Expansion of Magnetic Flux Tubes in the Solar Corona. *Astrophys. J.*, *775*(2), Article 120, 120. <https://doi.org/10.1088/0004-637X/775/2/120>
- Mandal, S., Peter, H., Chitta, L. P., Cuadrado, R. A., Schühle, U., Teriaca, L., Solanki, S. K., Harra, L., Berghmans, D., Auchère, F., Parenti, S., Zhukov, A. N., Buchlin, É., Verbeeck, C., Kraaikamp, E., Rodriguez, L., Long, D. M., Schwanitz, C., Barczynski, K., ... Cheung, M. C. (2023). Signatures of dynamic fibrils at the coronal base: Observations from Solar Orbiter/EUI. *Astron. Astrophys.*, *670*, Article L3, L3. <https://doi.org/10.1051/0004-6361/202245431>
- Mariska, J. T., Feldman, U., & Doschek, G. A. (1978). Measurements of extreme-ultraviolet emission-line profiles near the solar limb. *Astrophys. J.*, *226*, 698–705. <https://doi.org/10.1086/156652>
- Mariska, J. (1992). *The solar transition region*. Cambridge University Press. <https://books.google.de/books?id=Iu8XoEtXrykC>
- Martínez-Sykora, J., De Pontieu, B., Hansteen, V. H., Rouppe van der Voort, L., Carlsson, M., & Pereira, T. M. D. (2017). On the generation of solar spicules and Alfvénic waves. *Science*, *356*(6344), 1269–1272. <https://doi.org/10.1126/science.aah5412>
- Martínez-Sykora, J., De Pontieu, B., Testa, P., & Hansteen, V. (2011). Forward Modeling of Emission in Solar Dynamics Observatory/Atmospheric Imaging Assembly Passbands from Dynamic Three-dimensional Simulations. *Astrophys. J.*, *743*(1), Article 23, 23. <https://doi.org/10.1088/0004-637X/743/1/23>
- Mason, H. E., Landi, E., Pike, C. D., & Young, P. R. (1999). Electron density and temperature structure of two limb active regions observed by SOHO-CDS. *Solar Phys.*, *189*(1), 129–146. <https://doi.org/10.1023/A:1005246220208>
- McIntosh, S. W. (2007). On the Mass and Energy Loading of Extreme-UV Bright Points. *Astrophys. J.*, *670*(2), 1401–1413. <https://doi.org/10.1086/521948>
- McIntosh, S. W., & De Pontieu, B. (2009). High-Speed Transition Region and Coronal Upflows in the Quiet Sun. *Astrophys. J.*, *707*(1), 524–538. <https://doi.org/10.1088/0004-637X/707/1/524>

- Milanović, N., Chitta, L. P., & Peter, H. (2023). Diffuse solar coronal features and their spicular footpoints. *Astron. Astrophys.*, 673, Article A81, A81. <https://doi.org/10.1051/0004-6361/202245544>
- Mondal, B., Klimchuk, J. A., Vadawale, S. V., Sarkar, A., Del Zanna, G., Athiray, P. S., Mithun, N. P. S., Mason, H. E., & Bhardwaj, A. (2023). Role of Small-scale Impulsive Events in Heating the X-Ray Bright Points of the Quiet Sun. *Astrophys. J.*, 945(1), Article 37, 37. <https://doi.org/10.3847/1538-4357/acb8bb>
- Morgan, H., & Taroyan, Y. (2017). Global conditions in the solar corona from 2010 to 2017. *Science Advances*, 3(7), e1602056. <https://doi.org/10.1126/sciadv.1602056>
- Mou, C., Huang, Z., Xia, L., Madjarska, M. S., Li, B., Fu, H., Jiao, F., & Hou, Z. (2016). Magnetic Flux Supplement to Coronal Bright Points. *Astrophys. J.*, 818(1), Article 9, 9. <https://doi.org/10.3847/0004-637X/818/1/9>
- Müller, D., Nicula, B., Felix, S., Verstringe, F., Bourgoignie, B., Csillaghy, A., Berghmans, D., Jiggins, P., García-Ortiz, J. P., Ireland, J., Zahniy, S., & Fleck, B. (2017). JHelioviewer. Time-dependent 3D visualisation of solar and heliospheric data. *Astron. Astrophys.*, 606, Article A10, A10. <https://doi.org/10.1051/0004-6361/201730893>
- Müller, D., St. Cyr, O. C., Zouganelis, I., Gilbert, H. R., Marsden, R., Nieves-Chinchilla, T., Antonucci, E., Auchère, F., Berghmans, D., Horbury, T. S., Howard, R. A., Krucker, S., Maksimovic, M., Owen, C. J., Rochus, P., Rodriguez-Pacheco, J., Romoli, M., Solanki, S. K., Bruno, R., ... Williams, D. (2020). The Solar Orbiter mission. Science overview. *Astron. Astrophys.*, 642, Article A1, A1. <https://doi.org/10.1051/0004-6361/202038467>
- Nóbrega-Siverio, D., & Moreno-Insertis, F. (2022). A 2D Model for Coronal Bright Points: Association with Spicules, UV Bursts, Surges, and EUV Coronal Jets. *Astrophys. J. Lett.*, 935(2), Article L21, L21. <https://doi.org/10.3847/2041-8213/ac85b6>
- O'Shea, E., Gallagher, P. T., Mathioudakis, M., Phillips, K. J. H., Keenan, F. P., & Katsiyannis, A. C. (2000). Transition region and coronal structuring. *Astron. Astrophys.*, 358, 741–748.
- Parenti, S., & Vial, J. -. (2007). Prominence and quiet-Sun plasma parameters derived from FUV spectral emission. *Astron. Astrophys.*, 469(3), 1109–1115. <https://doi.org/10.1051/0004-6361:20077196>
- Parker, E. N. (1983). Magnetic neutral sheets in evolving fields. I - General theory. *Astrophys. J.*, 264, 635–647. <https://doi.org/10.1086/160636>
- Parker, E. N. (1988). Nanoflares and the Solar X-Ray Corona. *Astrophys. J.*, 330, 474. <https://doi.org/10.1086/166485>

- Patsourakos, S., & Klimchuk, J. A. (2006). Nonthermal Spectral Line Broadening and the Nanoflare Model. *Astrophys. J.*, *647*(2), 1452–1465. <https://doi.org/10.1086/505517>
- Patsourakos, S., Vial, J. .-, Gabriel, A. H., & Bellamine, N. (1999). Transition-Region Network Boundaries in the Quiet Sun: Width Variation with Temperature as Observed with CDS on SOHO. *Astrophys. J.*, *522*(1), 540–546. <https://doi.org/10.1086/307609>
- Pauluhn, A., Solanki, S. K., Rüedi, I., Landi, E., & Schühle, U. (2000). Statistics of quiet Sun extreme ultraviolet intensities. *Astron. Astrophys.*, *362*, 737–745.
- Pereira, T. M. D., De Pontieu, B., Carlsson, M., Hansteen, V., Tarbell, T. D., Lemen, J., Title, A., Boerner, P., Hurlburt, N., Wülser, J. P., Martínez-Sykora, J., Kleint, L., Golub, L., McKillop, S., Reeves, K. K., Saar, S., Testa, P., Tian, H., Jaeggli, S., & Kankelborg, C. (2014). An Interface Region Imaging Spectrograph First View on Solar Spicules. *Astrophys. J. Lett.*, *792*(1), Article L15, L15. <https://doi.org/10.1088/2041-8205/792/1/L15>
- Pesnell, W. D., Thompson, B. J., & Chamberlin, P. C. (2012). The Solar Dynamics Observatory (SDO). *Solar Phys.*, *275*(1-2), 3–15. <https://doi.org/10.1007/s11207-011-9841-3>
- Peter, H. (2001). On the nature of the transition region from the chromosphere to the corona of the Sun. *Astron. Astrophys.*, *374*, 1108–1120. <https://doi.org/10.1051/0004-6361:20010697>
- Peter, H., & Bingert, S. (2012). Constant cross section of loops in the solar corona. *Astron. Astrophys.*, *548*, Article A1, A1. <https://doi.org/10.1051/0004-6361/201219473>
- Peter, H., Bingert, S., & Kamio, S. (2012). Catastrophic cooling and cessation of heating in the solar corona. *Astron. Astrophys.*, *537*, Article A152, A152. <https://doi.org/10.1051/0004-6361/201117889>
- Peter, H., Bingert, S., Klimchuk, J. A., de Forest, C., Cirtain, J. W., Golub, L., Winebarger, A. R., Kobayashi, K., & Korreck, K. E. (2013). Structure of solar coronal loops: from miniature to large-scale. *Astron. Astrophys.*, *556*, Article A104, A104. <https://doi.org/10.1051/0004-6361/201321826>
- Peter, H., & Judge, P. G. (1999). On the Doppler Shifts of Solar Ultraviolet Emission Lines. *Astrophys. J.*, *522*(2), 1148–1166. <https://doi.org/10.1086/307672>
- Peter, H., Chitta, L. P., Chen, F., Pontin, D. I., Winebarger, A. R., Golub, L., Savage, S. L., Rachmeler, L. A., Kobayashi, K., Brooks, D. H., Cirtain, J. W., De Pontieu, B., McKenzie, D. E., Morton, R. J., Testa, P., Tiwari, S. K., Walsh, R. W., & Warren, H. P. (2022). Parallel Plasma Loops and

- the Energization of the Solar Corona. *Astrophys. J.*, 933(2), Article 153, 153. <https://doi.org/10.3847/1538-4357/ac7219>
- Peter, H., & Dwivedi, B. N. (2014). Discovery of the Sun's million-degree hot corona. *Frontiers in Astronomy and Space Sciences*, 1, Article 2, 2. <https://doi.org/10.3389/fspas.2014.00002>
- Peter, H., Gudiksen, B. V., & Nordlund, Å. (2006). Forward Modeling of the Corona of the Sun and Solar-like Stars: From a Three-dimensional Magnetohydrodynamic Model to Synthetic Extreme-Ultraviolet Spectra. *Astrophys. J.*, 638(2), 1086–1100. <https://doi.org/10.1086/499117>
- Priest, E. R., Foley, C. R., Heyvaerts, J., Arber, T. D., Culhane, J. L., & Acton, L. W. (1998). Nature of the heating mechanism for the diffuse solar corona. *Nature*, 393(6685), 545–547. <https://doi.org/10.1038/31166>
- Raouafi, N. .-, & Stenborg, G. (2014). Role of Transients in the Sustainability of Solar Coronal Plumes. *Astrophys. J.*, 787(2), Article 118, 118. <https://doi.org/10.1088/0004-637X/787/2/118>
- Raymond, J. C., & Doyle, J. G. (1981). The energy balance in coronal holes and average quiet-sun regions. *Astrophys. J.*, 247, 686–691. <https://doi.org/10.1086/159080>
- Reale, F. (2014). Coronal Loops: Observations and Modeling of Confined Plasma. *Living Reviews in Solar Physics*, 11(1), Article 4, 4. <https://doi.org/10.12942/lrsp-2014-4>
- Reeves, E. M. (1976). The EUV chromospheric network in the quiet sun. *Solar Phys.*, 46(1), 53–72. <https://doi.org/10.1007/BF00157554>
- Rochus, P., Auchère, F., Berghmans, D., Harra, L., Schmutz, W., Schühle, U., Addison, P., Appourchaux, T., Aznar Cuadrado, R., Baker, D., Barbay, J., Bates, D., BenMoussa, A., Bergmann, M., Beurthe, C., Borgo, B., Bonte, K., Bouzit, M., Bradley, L., ... Zhukov, A. N. (2020). The Solar Orbiter EUI instrument: The Extreme Ultraviolet Imager. *Astron. Astrophys.*, 642, Article A8, A8. <https://doi.org/10.1051/0004-6361/201936663>
- Roupe van der Voort, L., De Pontieu, B., Hansteen, V. H., Carlsson, M., & van Noort, M. (2007). Magnetoacoustic Shocks as a Driver of Quiet-Sun Mottles. *Astrophys. J. Lett.*, 660(2), L169–L172. <https://doi.org/10.1086/518246>
- Roupe van der Voort, L., Leenaarts, J., de Pontieu, B., Carlsson, M., & Visser, G. (2009). On-disk Counterparts of Type II Spicules in the Ca II 854.2 nm and H α Lines. *Astrophys. J.*, 705(1), 272–284. <https://doi.org/10.1088/0004-637X/705/1/272>
- Samanta, T., Tian, H., Yurchyshyn, V., Peter, H., Cao, W., Sterling, A., Erdélyi, R., Ahn, K., Feng, S., Utz, D., Banerjee, D., & Chen, Y. (2019). Gener-

- ation of solar spicules and subsequent atmospheric heating. *Science*, 366(6467), 890–894. <https://doi.org/10.1126/science.aaw2796>
- Sandlin, G. D., Bartoe, J. .-. F., Brueckner, G. E., Tousey, R., & Vanhoosier, M. E. (1986). The High-Resolution Solar Spectrum, 1175–1710 Angstrom. *Astrophys. J. Suppl.*, 61, 801. <https://doi.org/10.1086/191131>
- Scherrer, P. H., Schou, J., Bush, R. I., Kosovichev, A. G., Bogart, R. S., Hoeksema, J. T., Liu, Y., Duvall, T. L., Zhao, J., Title, A. M., Schrijver, C. J., Tarbell, T. D., & Tomczyk, S. (2012). The Helioseismic and Magnetic Imager (HMI) Investigation for the Solar Dynamics Observatory (SDO). *Solar Phys.*, 275(1-2), 207–227. <https://doi.org/10.1007/s11207-011-9834-2>
- Schou, J., Scherrer, P. H., Bush, R. I., Wachter, R., Couvidat, S., Rabello-Soares, M. C., Bogart, R. S., Hoeksema, J. T., Liu, Y., Duvall, T. L., Akin, D. J., Allard, B. A., Miles, J. W., Rairden, R., Shine, R. A., Tarbell, T. D., Title, A. M., Wolfson, C. J., Elmore, D. F., ... Tomczyk, S. (2012). Design and Ground Calibration of the Helioseismic and Magnetic Imager (HMI) Instrument on the Solar Dynamics Observatory (SDO). *Solar Phys.*, 275(1-2), 229–259. <https://doi.org/10.1007/s11207-011-9842-2>
- Schrijver, C. J. (2007). Braiding-induced Interchange Reconnection of the Magnetic Field and the Width of Solar Coronal Loops. *Astrophys. J. Lett.*, 662(2), L119–L122. <https://doi.org/10.1086/519455>
- Schrijver, C. J., & Title, A. M. (2003). The Magnetic Connection between the Solar Photosphere and the Corona. *Astrophys. J. Lett.*, 597(2), L165–L168. <https://doi.org/10.1086/379870>
- Solanki, S. K., del Toro Iniesta, J. C., Woch, J., Gandorfer, A., Hirzberger, J., Alvarez-Herrero, A., Appourchaux, T., Martínez Pillet, V., Pérez-Grande, I., Sanchis Kilders, E., Schmidt, W., Gómez Cama, J. M., Michalik, H., Deutsch, W., Fernandez-Rico, G., Grauf, B., Gizon, L., Heerlein, K., Kolléck, M., ... Zouganelis, I. (2020). The Polarimetric and Helioseismic Imager on Solar Orbiter. *Astron. Astrophys.*, 642, Article A11, A11. <https://doi.org/10.1051/0004-6361/201935325>
- Solanki, S. K., & Steiner, O. (1990). How magnetic is the solar chromosphere? *Astron. Astrophys.*, 234(1-2), 519–529.
- Solanki, S. K. (2003). Sunspots: An overview. *Astron. Astrophys. Rev.*, 11(2-3), 153–286. <https://doi.org/10.1007/s00159-003-0018-4>
- Solanki, S. K., Inhester, B., & Schüssler, M. (2006). The solar magnetic field. *Reports on Progress in Physics*, 69(3), 563–668. <https://doi.org/10.1088/0034-4885/69/3/R02>
- SPICE Consortium, Anderson, M., Appourchaux, T., Auchère, F., Aznar Cuadrado, R., Barbay, J., Baudin, F., Beardsley, S., Bocchialini, K., Borgo, B., Bruzzi,

- D., Buchlin, E., Burton, G., Büchel, V., Caldwell, M., Caminade, S., Carlsson, M., Curdt, W., Davenne, J., ... Müller, D. (2020). The Solar Orbiter SPICE instrument. An extreme UV imaging spectrometer. *Astron. Astrophys.*, 642, Article A14, A14. <https://doi.org/10.1051/0004-6361/201935574>
- Stansby, D., Yeates, A., & Badman, S. T. (2020). Pfsspy: A python package for potential field source surface modelling. *Journal of Open Source Software*, 5(54), 2732. <https://doi.org/10.21105/joss.02732>
- Stein, R. F. (2012). Solar Surface Magneto-Convection. *Living Reviews in Solar Physics*, 9(1), Article 4, 4. <https://doi.org/10.12942/lrsp-2012-4>
- Stenflo, J. O. (1973). Magnetic-Field Structure of the Photospheric Network. *Solar Phys.*, 32(1), 41–63. <https://doi.org/10.1007/BF00152728>
- Stix, M. (2002). *The Sun* (I. Appenzeller, G. Börner, A. Burkert, M. A. Dopita, T. Encrenaz, M. Harwit, R. Kippenhahn, J. Lequeux, A. Maeder, & V. Trimble, Eds.). Springer Berlin Heidelberg. <https://doi.org/10.1007/978-3-642-56042-2>
- Sturrock, P. A., Wheatland, M. S., & Acton, L. W. (1996). Yokhoh Soft X-Ray Telescope Images of the Diffuse Solar Corona. *Astrophys. J. Lett.*, 461, L115. <https://doi.org/10.1086/310010>
- Sun, X. (2018). Polar Field Correction for HMI Line-of-Sight Synoptic Data. *arXiv e-prints*, Article arXiv:1801.04265, arXiv:1801.04265. <https://doi.org/10.48550/ARXIV.1801.04265>
- Teriaca, L., Banerjee, D., Falchi, A., Doyle, J. G., & Madjarska, M. S. (2004). Transition region small-scale dynamics as seen by SUMER on SOHO. *Astron. Astrophys.*, 427, 1065–1074. <https://doi.org/10.1051/0004-6361:20040503>
- The SunPy Community, Barnes, W. T., Bobra, M. G., Christe, S. D., Freij, N., Hayes, L. A., Ireland, J., Mumford, S., Perez-Suarez, D., Ryan, D. F., Shih, A. Y., Chanda, P., Glogowski, K., Hewett, R., Hughitt, V. K., Hill, A., Hiware, K., Inglis, A., Kirk, M. S. F., ... Dang, T. K. (2020). The sunpy project: Open source development and status of the version 1.0 core package. *The Astrophysical Journal*, 890, 68–. <https://doi.org/10.3847/1538-4357/ab4f7a>
- Thompson, W. T. (2006). Coordinate systems for solar image data. *Astron. Astrophys.*, 449(2), 791–803. <https://doi.org/10.1051/0004-6361:20054262>
- Tian, H., DeLuca, E. E., Cranmer, S. R., De Pontieu, B., Peter, H., Martínez-Sykora, J., Golub, L., McKillop, S., Reeves, K. K., Miralles, M. P., McCauley, P., Saar, S., Testa, P., Weber, M., Murphy, N., Lemen, J., Title, A., Boerner, P., Hurlburt, N., ... McIntosh, S. W. (2014). Prevalence of small-scale jets from the networks of the solar transition region and

- chromosphere. *Science*, 346(6207), Article 1255711, 1255711. <https://doi.org/10.1126/science.1255711>
- Tian, H., Curdt, W., Marsch, E., & He, J. (2008). Cool and Hot Components of a Coronal Bright Point. *Astrophys. J. Lett.*, 681(2), L121. <https://doi.org/10.1086/590410>
- Vaiana, G. S., Krieger, A. S., & Timothy, A. F. (1973). Identification and Analysis of Structures in the Corona from X-Ray Photography. *Solar Phys.*, 32(1), 81–116. <https://doi.org/10.1007/BF00152731>
- Van Doorselaere, T., Srivastava, A. K., Antolin, P., Magyar, N., Vasheghani Farahani, S., Tian, H., Kolotkov, D., Ofman, L., Guo, M., Arregui, I., De Moortel, I., & Pascoe, D. (2020). Coronal Heating by MHD Waves. *Space Sci. Rev.*, 216(8), Article 140, 140. <https://doi.org/10.1007/s11214-020-00770-y>
- van Noort, M., Lagg, A., Tiwari, S. K., & Solanki, S. K. (2013). Peripheral downflows in sunspot penumbrae. *Astron. Astrophys.*, 557, Article A24, A24. <https://doi.org/10.1051/0004-6361/201321073>
- Vernazza, J. E., Avrett, E. H., & Loeser, R. (1981). Structure of the solar chromosphere. III. Models of the EUV brightness components of the quiet sun. *Astrophys. J. Suppl.*, 45, 635–725. <https://doi.org/10.1086/190731>
- Viall, N. M., & Klimchuk, J. A. (2011). Patterns of Nanoflare Storm Heating Exhibited by an Active Region Observed with Solar Dynamics Observatory/Atmospheric Imaging Assembly. *Astrophys. J.*, 738(1), Article 24, 24. <https://doi.org/10.1088/0004-637X/738/1/24>
- Viall, N. M., & Klimchuk, J. A. (2012). Evidence for Widespread Cooling in an Active Region Observed with the SDO Atmospheric Imaging Assembly. *Astrophys. J.*, 753(1), Article 35, 35. <https://doi.org/10.1088/0004-637X/753/1/35>
- Virtanen, P., Gommers, R., Oliphant, T. E., Haberland, M., Reddy, T., Cournapeau, D., Burovski, E., Peterson, P., Weckesser, W., Bright, J., van der Walt, S. J., Brett, M., Wilson, J., Millman, K. J., Mayorov, N., Nelson, A. R. J., Jones, E., Kern, R., Larson, E., ... SciPy 1.0 Contributors. (2020). SciPy 1.0: Fundamental Algorithms for Scientific Computing in Python. *Nature Methods*, 17, 261–272. <https://doi.org/10.1038/s41592-019-0686-2>
- Warren, H. P., Brooks, D. H., & Winebarger, A. R. (2011). Constraints on the heating of high-temperature active region loops: Observations from hinode and the solar dynamics observatory. *The Astrophysical Journal*, 734(2), 90. <https://doi.org/10.1088/0004-637X/734/2/90>

- Warren, H. P., Winebarger, A. R., & Brooks, D. H. (2012). A Systematic Survey of High-temperature Emission in Solar Active Regions. *Astrophys. J.*, 759(2), Article 141, 141. <https://doi.org/10.1088/0004-637X/759/2/141>
- Webb, D. F., Martin, S. F., Moses, D., & Harvey, J. W. (1993). The Correspondence Between X-Ray Bright Points and Evolving Magnetic Features in the Quiet Sun. *Solar Phys.*, 144(1), 15–35. <https://doi.org/10.1007/BF00667979>
- Wiegelmann, T., & Solanki, S. K. (2004). Similarities and Differences between Coronal Holes and the Quiet Sun: Are Loop Statistics the Key? *Solar Phys.*, 225(2), 227–247. <https://doi.org/10.1007/s11207-004-3747-2>
- Wiegelmann, T., Solanki, S. K., Borrero, J. M., Martínez Pillet, V., del Toro Iniesta, J. C., Domingo, V., Bonet, J. A., Barthol, P., Gandorfer, A., Knölker, M., Schmidt, W., & Title, A. M. (2010). Magnetic Loops in the Quiet Sun. *Astrophys. J. Lett.*, 723(2), L185–L189. <https://doi.org/10.1088/2041-8205/723/2/L185>
- Wiegelmann, T., Thalmann, J. K., & Solanki, S. K. (2014). The magnetic field in the solar atmosphere. *Astron. Astrophys. Rev.*, 22, Article 78, 78. <https://doi.org/10.1007/s00159-014-0078-7>
- Wilhelm, K., Lemaire, P., Feldman, U., Hollandt, J., Schühle, U., & Curdt, W. (1997). Radiometric calibration of sumer: Refinement of the laboratory results under operational conditions on soho. *Appl. Opt.*, 36(25), 6416–6422. <https://doi.org/10.1364/AO.36.006416>
- Williams, T., Walsh, R. W., Winebarger, A. R., Brooks, D. H., Cirtain, J. W., De Pontieu, B., Golub, L., Kobayashi, K., McKenzie, D. E., Morton, R. J., Peter, H., Rachmeler, L. A., Savage, S. L., Testa, P., Tiwari, S. K., Warren, H. P., & Watkinson, B. J. (2020). Is the High-Resolution Coronal Imager Resolving Coronal Strands? Results from AR 12712. *Astrophys. J.*, 892(2), Article 134, 134. <https://doi.org/10.3847/1538-4357/ab6dcf>
- Withbroe, G. L., & Noyes, R. W. (1977). Mass and energy flow in the solar chromosphere and corona. *Ann. Rev. Astron. Astrophys.*, 15, 363–387. <https://doi.org/10.1146/annurev.aa.15.090177.002051>
- Young, P. R. (2005). The element abundance FIP effect in the quiet Sun. *Astron. Astrophys.*, 439(1), 361–366. <https://doi.org/10.1051/0004-6361:20052963>
- Young, P. R. (2018). Element Abundance Ratios in the Quiet Sun Transition Region. *Astrophys. J.*, 855(1), Article 15, 15. <https://doi.org/10.3847/1538-4357/aaab48>
- Young, P. (2023). CHIANTI Technical Report No. 22: CHIANTI software for interfacing with emission measure codes. <https://doi.org/10.5281/zenodo.7504532>

- Zhang, J., Kundu, M. R., & White, S. M. (2001). Spatial Distribution and Temporal Evolution of Coronal Bright Points. *Solar Phys.*, 198(2), 347–365. <https://doi.org/10.1023/A:1005222616375>

Publications

Refereed publications

Milanović, N., Chitta, L. P., Peter, H., *Diffuse solar coronal features and their spicular footpoints*, 2023, *A&A*, 673, A81, DOI: 10.1051/0004-6361/202245544

Vučetić, M., **Milanović, N.**, Urošević, D., Raymond, J., Onić, D., Milošević, S., Petrov, N., *Proper Motion of Cygnus Loop Shock Filaments*, 2023, *SAJ*, 207, 9, DOI: 10.2298/SAJ2307009V

Conference presentations

- Thermal structuring and evolution of coronal bright points, *EclipseSA Meeting*, 04.2024, San Antonio, Texas, USA – Poster
- Thermal structuring and evolution of coronal bright points, *SOLARNET Conference*, 05.2023, Potsdam, Germany – Poster
- Thermal structuring and evolution of coronal bright points, *8th Solar Orbiter Workshop*, 09.2022, Belfast, UK – Poster
- Diffuse solar coronal features originating from highly structured spicular footpoints, *10th Coronal Loops Workshop*, 06.2022, Paris, France – Contributed talk
- Identifying the spicular footpoints of diffuse coronal emission in the transition region, *Hinode 14 / IRIS 11 Meeting*, 10.2021, Virtual Meeting – Contributed talk
- Thermal structure of coronal bright points at their base in the low transition region, *16th European Solar Physics Meeting*, 09.2021, Virtual Meeting – Postertalk

Acknowledgments

I am grateful for the opportunity to do a PhD as a part of the IMPRS at MPS. I enjoyed working in a diverse and international environment, where I had many chances to participate in scientific meetings and engage in inspiring discussions with colleagues. Over the last almost four years, my work was guided by the members of my Thesis Advisory Committee – Hardi, Sami, Karl-Heinz and Luca, whom I would like to thank here.

I would especially like to thank my daily supervisors Hardi and Pradeep, from whom I learned a lot, who always found time for me, and had no trouble discussing the same issues many times. Although work was not always easy, they approached any difficulties on the way with a very supportive and positive attitude, which I could look up to.

I also need to thank my parents, brother, and grandmothers, who were always there for me, and my husband Lazar, for his endless support during the tough last stages of my PhD. Hvala mojoj porodici na neizmernoj podršci tokom prethodne četiri godine, i uvek.

Finally, I would like to thank my friends from the IMPRS cohort, who brightened my days in Göttingen, and filled them with laughs, long coffee breaks, movie nights, board games, meaningless and meaningful conversations.

Curriculum Vitae

Personal data

Name: Nikolina Milanović
Date of birth: 05.10.1995
Place of birth: Pančevo, Serbia

Education

Since November 2020: PhD in Physics

International Max Planck Research School (IMPRS)
at the Max Planck Institute for Solar System Research, Göttingen, Germany
and Technische Universität Braunschweig, Braunschweig, Germany

Thesis title: Structuring of the quiet solar corona
Supervisors: Prof. Dr. Hardi Peter, Dr. Lakshmi Pradeep Chitta,
Prof. Dr. Sami Solanki, Prof. Dr. Karl-Heinz Glaßmeier, Dr. Luca Teriaca

October 2018 – September 2019: MSc in Astronomy

Department of Astronomy, Faculty of Mathematics,
University of Belgrade, Belgrade, Serbia

Thesis title: Shock speed in nonradiative and radiative filaments
in the supernova remnant Cygnus Loop
Supervisors: Dr. Milica Vučetić, Dr. Dušan Onić

October 2014 – July 2018: BSc in Astronomy

Department of Astronomy, Faculty of Mathematics,
University of Belgrade, Belgrade, Serbia



Nikolina Milanović: Structuring of the quiet solar corona

The heating of the solar corona, the tenuous outer atmosphere of the Sun, has remained one of the major open questions in solar physics for decades. How the coronal plasma, above the much cooler photosphere, reaches temperatures of millions of degrees is closely related to the magnetic field on the Sun. The corona is structured by the magnetic field, as is particularly evident in bright, arch-shaped coronal loops. In contrast to the clear loops, the corona also exhibits regions of diffuse emission, that show no obvious substructure. This poses the questions of what determines the amount of structure we can see in the corona, how the diffuse emission is connected to magnetic footpoints in the lower atmosphere, and how different the heating mechanisms in distinct loops and in the diffuse areas are. To shed light on these questions, we focus on observations of the quiet corona, whose magnetic footpoints lie in the supergranular magnetic network in the photosphere. We explore how this highly-structured magnetic foundation can support both structured small loops, and featureless diffuse emission.